UNIVERSITÀ DEGLI STUDI DI NAPOLI FEDERICO II

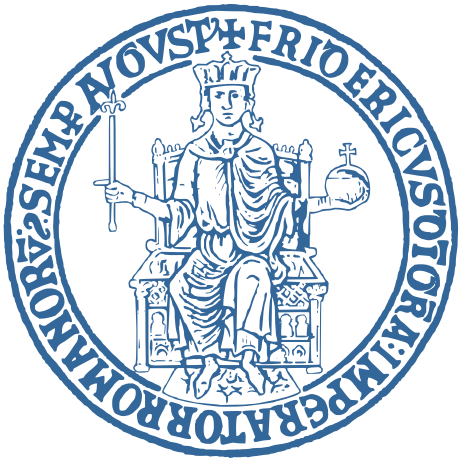

Dipartimento di Ingegneria Industriale

TESI

DOTTORATO DI RICERCA IN INGEGNERIA INDUSTRIALE

XXXV CICLO

Thermo-fluid dynamic properties of porous materials for energy conversion

Supervisore

Prof. Ing. Raffaele Dragonetti

Candidato

Elio Di Giulio

"L’uomo che ama camminare, camminerà più a lungo dell’uomo che ama la destinazione"

A Chiara

Acknowledgments

"L'uomo che ama camminare, camminerà più a lungo dell'uomo che ama la destinazione"

Sono profondamente convinto che questa frase racchiuda in sé l'essenza della ricerca. La continua voglia di conoscere, di capire e soprattutto di scoprire mi hanno permesso di trovare la mia dimensione in questo enorme mondo. Lo stesso mondo che a volte può risultare sconfortante, dispersivo e deludente se non lo si affronta con il supporto adeguato. L'enorme risorsa di energia che ho la fortuna di avere nella mia vita è la mia famiglia: Chiara, in grado di colorare il mio mondo che altrimenti sarebbe fatto di algoritmi, simulazioni e test in laboratorio e con la quale quotidianamente condividiamo le nostre vite, mia mamma Maria Grazia e mio padre Livio, che mi hanno spinto sempre a diventare ciò che vorrei essere nella vita, mio Fratello Luca, la mia famiglia allargata Rossella, Lorenzo, Livio e Maria Pia, ed un'altra famiglia che mi ha accolto come un figlio, Rosaria e Rino.E' innegabile che la mia passione per il mondo della ricerca, nel cercare giorno dopo giorno, nel mio infinitesimamente piccolo contributo, di spostare più in la quell'asticella della conoscenza, sia dovuta a Raffaele, che chiamo abitualmente *il prof* ma che probabilmente è riduttivo per la passione che quotidianamente trasmette in questo lavoro. Devo ringraziarlo per avermi guidato nel mio meraviglioso percorso di dottorato che mi ha portato fino a Parigi, da Camille Perrot dove ho potuto constatare che la scienza, quella vera, non parla italiano o francese, ma una sola lingua: quella della scoperta. Al termine del mio percorso di laurea magistrale non potevo avere idea di quale fosse il futuro che mi aspettava, probabilmente anche ora ma con una grande differenza: ad oggi so qual è il futuro che vorrei e come andare a prenderlo.

Elio

Abstract

Thermoacoustics combines thermodynamics, fluid dynamics and acoustics to describe the interaction that exists between heat and sound. Two types of devices can be realized which are based on the thermoacoustic conversion of energy: thermoacoustic *refrigerator* (or *heat pump*) that convert sound wave energy in refrigeration (or heating), thermoacoustic *engine* that convert heat in useful work. Nevertless, thermoacoustic technology could play a significant role in the development of renewable energies because of its advantages over conventional energetic technologies (environmentally friendly working fluid, low-grade energetic inputs can be used as driving sources, no moving part, low manufacturing and maintenance costs), actually there are still some challenges left that need to be resolved before thermoacoustic devices can be used competitively on a large scale. The core of thermoacoustic engines and heat pumps (or refrigerators), in which the energy conversion takes place, is represented by a particular porous material, named *stack* (or *regenerator*), suitably designed to allow the correct viscous and thermal interactions between the oscillating fluid and its solid surface in order to convert a mechanical energy (as a sound wave) into heat, and *vice versa*. To make these devices more efficient, it is crucial to understand the phenomena that occur in that porous core better and then identify the ideal geometry for each unique working condition. Therefore, the characterization of a porous material, used as *stack*, is made through the study of the thermo-fluid dynamic fields inside its solid skeleton fulfilled by a fluid. In particular, fluid mechanics balance equations for fluids need to be solved in the harmonic regime, because of the fluid moves under an oscillating flow (as sound wave is) stimulus. The goal of this thesis work is to expand the frontiers of knowledge in thermoacoustics by employing unconventional materials as *stacks*. Unconventional thermoacoustic *stacks*, such as Tetragonal Pin Array, Wire Mesh and 3D-Membrane Foams, have been investigated. New semi-phenomenological models, inspired by classically used models used to predict the sound absorption (or sound transmission loss) applications, are used to mathematically describe their behaviour. These predictive models of the viscous and thermal behaviours are based on their *micro-geometrical* features. Furthermore, the experimental validations of the predictive models have been carried out. Two new measuring approaches have been devised to address the shortcomings of the existing experimental methodologies, particularly in the low frequency range, for evaluating the dynamic behaviour of porous materials. Finally, an energetic criterion to select the core which maximize the heat-to-acoustic energy conversion has been presented.

Contents

List of Figures

List of Tables

Chapter 1

General introduction

Contents

1.1 Background and context

Research on sustainable technologies has received increasing attention in the past 20 years due to a rise in the energy consumption by human activities and a global focus on pollution and environmental challenges. Thermoacoustic technology can play a significant role in this context because of, the use of low-grade input energy (such as solar energy or industrial waste heat) as an energy source, the use of environmentally friendly working fluids (air, noble gas), and low realization and maintenance costs. Two types of devices can be realized which are based on the thermoacoustic conversion of energy: thermoacoustic *refrigerator* (or *heat pump*) that convert sound wave energy in refrigeration (or heating), thermoacoustic *engine* that convert heat in useful work. The literature shows that thermoacoustic technologies have been used in different applications such as electricity generation [1], domestic refrigeration [2], automotive industry [3], cryogenics [4], and thermal management of electronic devices [5]. Despite these advantages, thermoacoustic technology needs to be improved before it could represent a reasonable alternative solution to the present systems. The core of thermoacoustic engines and heat pumps (or refrigerators), in which the energy conversion takes place, is represented by a particular porous material [6], named *stack* (or *regenerator*). It is suitably designed to allow the correct viscous and thermal interactions between the oscillating fluid and its solid surface in order to convert a mechanical energy (as a sound wave) into heat, and *vice versa*. To make these devices more efficient, it is crucial to understand the phenomena that occur in that porous core better and then identify the ideal geometry for each unique working situation. Fig. 1.1 highlights the fields of science involved in thermoacoustics. Therefore, the analysis of the thermo-fluid dynamic fields within the solid skeleton filled by a fluid is carried out to characterize a porous material used as a *stack*. Because fluid moves in response to oscillating flow stimuli, like sound waves, fluid mechanics balancing equations for fluids must be specifically solved in the harmonic regime. Then, acoustic literature may be used to predict the viscous and thermal behaviours of the materials, using a semi-phenomenological model based on the materials' microstructure. Last but not the least, thermodynamics is fundamental to quantify the energy exchange and heat to mechanical power (and *vice versa*) conversion.

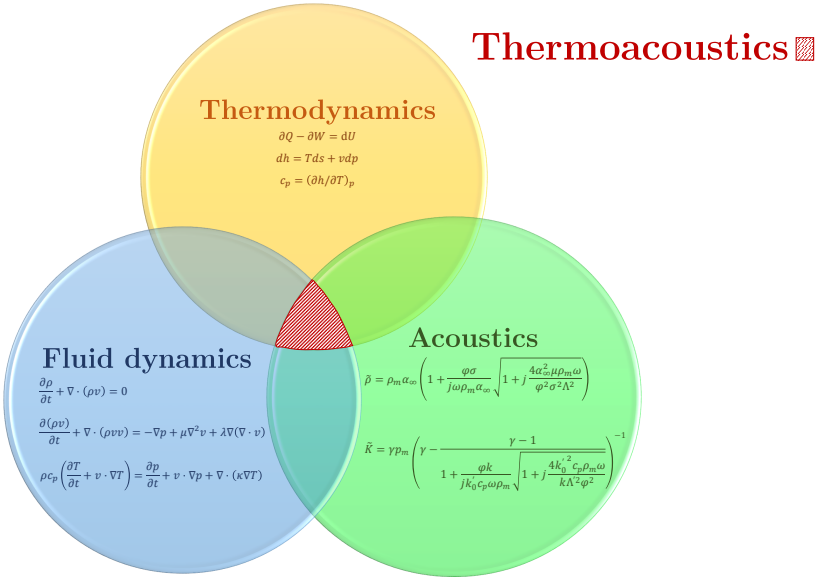

Figure 1.1: Illustration of the different fields of science involved in thermoacoustics.

1.2 Research objective and outline

In thermoacoustic literature, uniform cross sectional material are generally employed as *stack*. They are characterized by analytical formulations to describe their dynamic behaviour under oscillating flows. Nevertheless, their pore size is often too large to ensure very good heat contact between the gas and the solid material, which is fundamental for the thermoacoustic phenomena to rise up. Because of this constraint, materials with more complex geometry are mostly preferred. The goal of this thesis work is to expand the frontiers of knowledge in thermoacoustics by employing unconventional materials as *stacks*. Unconventional thermoacoustic *stacks*, such as Tetragonal Pin Array, Wire Mesh and 3D-Membrane Foams, have been investigated. New semi-phenomenological models, inspired by classically used models used to predict the sound absorption (or sound transmission loss) applications, are used to mathematically describe their behaviour. These predictive models of the viscous and thermal behaviours are based on their *micro-geometrical* features. Furthermore, the experimental validations of the predictive models have been carried out. Two new measuring approaches have been devised to address the shortcomings of the existing experimental methodologies, particularly in the low frequency range, for evaluating the dynamic behaviour of porous materials. Finally, an energetic criterion to select the core which maximize the heat-to-acoustic energy conversion has been presented. The outline of the thesis is presented in the following. In Sec. 2, physical and mathematical background is recalled starting from fluid mechanics equations to thermoacoustic theory, together with the description of the electroacoustic analogy. Acoustic semi-phenomenological models to predict the viscous and thermal behaviours of a rigid frame porous material and its micro geometrical (*transport*) parameters are presented in Sec. 3 .The numerical studies and the transport parameters models for three selected porous materials, such as Tetragonal Pin Array, Wire Mesh and 3D-Membrane Foams are reported in Sec. 4 , while Sec. 5 shows an overview of the existing measurement techniques for the dynamic behaviours of the porous media and two novel lumped element techniques. Thermoacoustic analyses are reported in Sec. 6 where the energetic theory is developed based on the microstructure features of the *stacks* and the thermoacoustic numerical scheme to solve acoustic and thermal field in such engine and heat pump is presented together with a performance comparison between the selected porous media. Finally, in Sec. 7 future developments and a few remarks conclude the work.

Chapter 2

Wave propagation in fluid-saturated porous medium

Contents

2.1 Introduction

The thesis aims to describe the energy conversions that occur inside porous materials as sound waves propagate through them. A porous medium, being a *heterogeneous* system made of a *solid matrix* with its void filled with fluids, can be treated as a continuum by properly accounting for the role of each phase in transport through this system of phases [7]. Therefore, to schematize the porous material as a single body with *homogeneous* behaviour it will be fundamental to correctly assess the viscous and thermal interaction between the fluid phase and the solid skeleton. In this chapter a brief presentation of the general equations of fluid mechanics is reported. Subsequently, the linearized version of Navier-Stoker equations will be presented in the frequency domain together with the scale separation approach for the viscous and thermal effects. Therefore, the analogy between the equations describing sound propagation inside a porous material and the electrical transmission line equations (*Telegrapher's equations*) will be highlighted. Finally, thermoacoustic mathematical background will be shown. In the last part, the classical assumptions of solid heat capacity being much higher than fluid heat capacity, that are regularly utilized in literature, will be removed in order to appropriately handle the thermal behavior of the solid skeleton.

2.2 General equations in fluid mechanics

Fluid mechanics concerns the study of the motion of fluids (liquid and gases) [8]. Since the phenomena considered in fluid dynamics are macroscopic, a fluid is regarded as a continuous medium. This means that even when a infinitely small elements of fluid volume is considered, it is large when compared with the distances between molecules. The complete mathematical description of the state of a moving fluid is given by the fields distribution of a momentum quantity such as the fluid velocity vector $\mathbf{v} = \mathbf{v}(x, y, z, t)$ and any two thermodynamic quantities of the fluid, for instance the pressure $p = p(x, y, z, t)$ and the density $\rho = \rho(x, y, z, t)$. All these quantities are, in general, functions of the spatial coordinates x, y, z and of the time t.

2.2.1 The equation of continuity

The equation of continuity expresses the conservation of matter. Let us consider a infinitesimal volume $\mathrm{d}V$ of space with a boundary surface $\mathrm{d}\Omega$. The mass of fluid in this volume is $\rho \mathrm{d}V$, while the mass of fluid flowing in unit time through an element $\mathrm{d}\Omega$ is $\rho \mathbf{v} \cdot \mathrm{d}\Omega$. Therefore, the general balance equation can be written as the sum of variation per unit time in the mass of fluid in the reference volume and the convective term flowing across the surface control of the volume. By using the differential formulation, it can be written as:

$$\frac{\partial \rho}{\partial t} + \nabla \cdot (\rho \mathbf{v}) = 0. \tag{2.1}$$

In the case of incompressible fluid ($\rho = cost$), Eq. (2.1) becomes $\nabla \cdot \mathbf{v} = 0$.

2.2.2 The equation of motion in a viscous fluid

To describe the motion of a real fluid, thermodynamic irreversibility effects due to internal friction (viscosity) must be considered. These contributes are reported in the *viscous stress tensor* σ' where its components can be written as

$$\sigma'_{ij} = \mu \left(\frac{\partial v_i}{\partial x_j} + \frac{\partial v_j}{\partial x_i} - \frac{2}{3} \delta_{ij} \frac{\partial v_i}{\partial x_i} \right) + \zeta \delta_{ij} \frac{\partial v_i}{\partial x_i} \tag{2.2}$$

where μ and ζ are respectively the dynamic and the bulk viscosity of the fluid. Therefore, the variation in time of the momentum in a volume of fluid $\mathrm{d}V$ is expressed, in vector form, as the sum of the surface and viscous forces:

$$\frac{\partial \rho \mathbf{v}}{\partial t} + \nabla \cdot (\rho \mathbf{v}\, \mathbf{v}) = -\nabla p + \mu \nabla^2 \mathbf{v} + \left(\zeta + \frac{1}{3}\mu\right) \nabla (\nabla \cdot \mathbf{v}) \,. \tag{2.3}$$

This equation is properly called the *Navier-Stokes equation*. It becomes simpler if the fluid may be regarded as incompressible, so the last term on the right of Eq. (2.3) is zero, and it can be written as follow

$$\frac{\partial \rho \mathbf{v}}{\partial t} + \nabla \cdot (\rho \mathbf{v}\, \mathbf{v}) = -\nabla p + \mu \nabla^2 \mathbf{v}. \tag{2.4}$$

2.2.3 The equation of heat transfer

In a viscous fluid the law of conservation of energy express the equality between the change per unit time in the total energy of the fluid in any volume and the total flux of energy through the surface bounding the control volume. One contribute is the energy transfer due to the *thermal conduction*, where the flux density is related to the variation of temperature through the fluid and its *thermal conductivity* κ as

$$\mathbf{q} = -\kappa \nabla T. \tag{2.5}$$

The other contribution to energy transfer is due to the processes of internal friction. This latter flux is giver by the vector $\mathbf{v} \cdot \boldsymbol{\sigma'}$ (by using the *Einstein tensor notation* it can be written as $v_i {\sigma'}_{ij}$). Accordingly, the general law of conservation of energy can be reported in terms of entropy s as follow

$$\rho T \left(\frac{\partial s}{\partial t} + \mathbf{v} \cdot \nabla s\right) = {\sigma'}_{ij} \frac{\partial v_i}{\partial x_j} + \nabla \cdot (\kappa \nabla T) \,. \tag{2.6}$$

By considering the thermodynamic relation $ds = c_p \frac{dT}{T} - \frac{dp}{\rho T}$, where c_p is the *specific heat at constant pressure*, Eq. (2.6) becomes

$$\rho c_p \left(\frac{\partial T}{\partial t} + \mathbf{v} \cdot \nabla T\right) = \frac{\partial p}{\partial t} + \mathbf{v} \cdot \nabla p + {\sigma'}_{ij} \frac{\partial v_i}{\partial x_j} + \nabla \cdot (\kappa \nabla T) \,. \tag{2.7}$$

In the extended form, the term ${\sigma'}_{ij} \frac{\partial v_i}{\partial x_j}$ is written as the sum of two quantities:

$$\frac{1}{2}\mu \left(\frac{\partial v_i}{\partial x_j} + \frac{\partial v_j}{\partial x_i} - \frac{2}{3}\delta_{ij} \frac{\partial v_i}{\partial x_i}\right)^2 + \zeta (\nabla \cdot \mathbf{v}) \,.$$

In the case of incompressible fluid, the latter term vanishes in the energy equation.

2.3 The linearized Navier-Stokes equations in frequency domain

An oscillating flow arises when a fluid, that is saturating the pore domain of a porous media with a rigid skeleton, responds to a wave stimulus. Therefore, the behaviour of the fluid is described by the coupled *linearized Navier-Stokes equations* in harmonic regime [9, 10]. Said f the frequency, $\omega = 2\pi f$ the angular frequency and $i = \sqrt{-1}$ the imaginary unit, in this treatment the *Rott's acoustic approximation* will be adopted with the following hypothesis [11]:

- Steady-state sinusoidal oscillations of the thermodynamic and kinematic variables such as pressure, temperature, density and velocity are considered and written in complex notation

sum of the mean values (subscripts m) and the first-order oscillating terms (subscripts 1; note also that a positive convention has been adopted $e^{i\omega t}$ and $\Re$ represents the real part of a complex number):

$$\rho(x,y,z,t) = \rho_m + \Re\left[\rho_1(x,y,z)e^{i\omega t}\right], \tag{2.8a}$$

$$T(x,y,z,t) = T_m + \Re\left[T_1(x,y,z)e^{i\omega t}\right], \tag{2.8b}$$

$$p(x,y,z,t) = p_m + \Re\left[p_1(x,y,z)e^{i\omega t}\right], \tag{2.8c}$$

$$\mathbf{v}(x,y,z,t) = \Re\left[\mathbf{v}_1(x,y,z)e^{i\omega t}\right]. \tag{2.8d}$$

- The time-dependent parts of all variables are small compared to the mean values. The products of small variables can often be neglected in comparison to the small variables themselves (*second order variables*).
- The mean pressure must be spatially uniform (independent of x, y and z) because any gradient in p_m, Eq. (2.8c), would cause an acceleration of gas. In addition, the mean velocity is assumed to be zero for the consideration above, see Eq. (2.8d).

With these approximations, simplified harmonic version of equations of fluid mechanics can be derived. Recalling that $\partial/\partial t$ is identical to $i\omega$ and neglecting the second-order terms, Eqs. (2.1), (2.3), and (2.7) over the fluid domain become

$$i\omega\rho_1 + \nabla\cdot(\rho_m\mathbf{v}) = 0, \tag{2.9}$$

$$i\omega\rho_m\mathbf{v}_1 = -\nabla p_1 + \mu\nabla^2\mathbf{v}_1, \tag{2.10}$$

$$i\omega\rho_m c_p T_1 = i\omega p_1 + \kappa\nabla^2 T_1. \tag{2.11}$$

Together with this set of five coupled equations, the description of the thermodynamic and kinematic fields in the fluid domain is completed by the equation of state:

$$\frac{p_1}{p_m} = \frac{\rho_1}{\rho_m} + \frac{T_1}{T_m}. \tag{2.12}$$

2.4 Homogenization of a rigid-frame porous media

From a theoretical point of view, the dynamic viscous and thermal behaviour of a generic porous material under the action of an oscillating flow can be derived by solving three linearized equations, Eqs. (2.9), (2.10), (2.11) coupled with the equation of state in the frequency domain, Eq. (2.12). In this treatment, the solid skeleton is assumed motionless because either the solid frame stiffness or its weight is significantly larger than that of the saturating fluid. The existence of a microscopic characteristic length l, determined by the size of local heterogeneities or the period size of the material, and a macroscopic characteristic length $L = \lambda/2\pi$, where $\lambda = c/f$ is the sound wavelength with c the speed of sound, and their highly distinct values, i.e. $l/L \ll 1$, permit defining a Representative Elementary Volume, see Fig. 2.1 [12]. Therefore, under scale separation between the wavelength and the characteristic size of the pore (as highlighted by Kirchhoff [13] for $r_w^{3/2} f < 10^6\ cm\ s^{-3/2}$, with r_w the pore size being greater than $10^{-3}\ cm$), momentum and

energy equations allow to describe the visco-inertial and heat diffusion effect separately, together with the hypotheses of rigid and isothermal walls of the material solid skeleton, Ω_{fs}:

$$\mathbf{v}_1 = 0 \quad \text{on} \quad \Omega_{fs}, \tag{2.13a}$$

$$T_1 = 0 \quad \text{on} \quad \Omega_{fs}. \tag{2.13b}$$

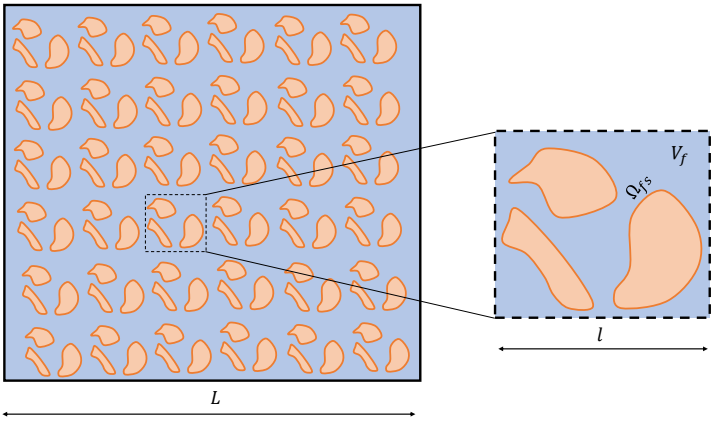

Figure 2.1: On the left, macroscopic scale description, and on the right microscopic scale description of a periodic porous media.

Named x the coordinate of wave propagation direction, space-averaged solutions of Eqs. (2.10), (2.11) can be written in terms of two frequency-dependent response functions to describe the overall acoustic behaviour of fluid saturating porous materials:

$$\frac{dp_1}{dx} = -\frac{i\omega\rho_m}{1-f_\nu}\langle v_1\rangle, \tag{2.14}$$

$$\langle T_1\rangle = \frac{1}{\rho_m c_p}\left(1-f_\kappa\right)p_1. \tag{2.15}$$

The angular brackets define the following averaging operator

$$\langle\cdot\rangle = \frac{1}{V_f}\int_{V_f}(\cdot)\,\mathrm{d}V$$

which is related to the spatial average over the fluid volume in the unit cell of the porous material. The unbolded quantity v_1 represent the x-component of the acoustic velocity vector $\mathbf{v}_1$. By substituting Eq. (2.15) and the spatially averaging of Eq. (2.12) in the continuity equation Eq. (2.9) and remembering the fundamental gas law $p_m/\rho_m = RT_m$, where $R = (\gamma-1)/\gamma\, c_p$ is the universal gas constant and γ the specific heat ratio, it follows that

$$\frac{d\langle v_1\rangle}{dx} = -\frac{i\omega}{\gamma p_m}\left[1+(\gamma-1)\,f_\kappa\right]p_1. \tag{2.16}$$

Thermoviscous functions f_ν and f_κ determine the dynamic complex behaviour of the porous material and they depend from its micro-geometry and from the fluid properties expressed as the *viscous* and *thermal boundary layers*

$$\delta_\nu = \sqrt{\frac{2\mu}{\omega\rho_m}}, \tag{2.17}$$

$$\delta_\kappa = \sqrt{\frac{2\kappa}{\omega \rho_m c_p}}. \tag{2.18}$$

Note that $P_r = \left(\delta_\nu/\delta_\kappa\right)^2$, where P_r is the fluid *Prandtl number*. An analytical formulation for these thermoviscous functions is provided in literature for elementary geometry pores (Fig. 2.2), such as slits, circular pores, rectangular pores and convex geometry such as pin array [14] (as reported in Tab. 2.1). Historically, thermoviscous functions were introduced by Rott [11] to characterize the visco-thermal interaction between solid skeleton and the oscillating fluid in thermoacoustic science. In acoustics, Zwikker and Kosten [15] introduced two complex quantities, the density $\tilde{\rho}$ and the bulk modulus $\tilde{K}$, to describe the behaviour of a porous material as an equivalent fluid. From a fluid-dynamic point of view, the dynamic behaviour of a fluid flow fulfilling a porous core can be expressed in terms of complex friction factor f_f and Nusselt number N_u [16]. Therefore, the complete characterization of acoustic porous media requires two dynamic frequency-depending parameters and it can be demonstrated that all the above approaches are equivalent. In fact, Liu and Garrett derived the equivalence between the complex friction factor and Nusselt number with the thermoviscous function [17]. While, Dragonetti *et al.* pointed out the equivalence between acoustic and thermoacoustic description of porous materials [18]

$$\tilde{\rho} = \frac{\rho_m}{1 - f_\nu} \tag{2.19}$$

$$\tilde{K} = \frac{\gamma p_m}{1 + (\gamma - 1)\, f_\kappa} \tag{2.20}$$

Geometry	Thermoviscous function f_j for ($j = \kappa$ or ν)
Parallel plate	$f_j = \frac{\tanh\left[(1+i)y_0/\delta_j\right]}{(1+i)y_0/\delta_j}$
Circular pore	$f_j = \frac{2J_1\left[(i-1)r_0/\delta_j\right]}{2J_0\left[(i-1)r_0/\delta_j\right](i-1)r_0/\delta_j}$
Rectangular pore	$f_j = 1 - \frac{64}{\pi^4}\sum_{m,n \text{ odd}}^{\infty}\left(m^2n^2\left[1 - i\frac{\pi^2\delta_j^2}{8a^2b^2}\left(b^2m^2 + a^2n^2\right)\right]\right)^{-1}$
Pin array	$f_j = -\frac{\delta_j}{i-1}\frac{2r_i}{r_0^2 - r_i^2}\frac{Y_1\left[(i-1)r_0/\delta_j\right]J_1\left[(i-1)r_i/\delta_j\right] - Y_1\left[(i-1)r_i/\delta_j\right]J_1\left[(i-1)r_0/\delta_j\right]}{Y_1\left[(i-1)r_0/\delta_j\right]J_0\left[(i-1)r_i/\delta_j\right] - Y_0\left[(i-1)r_i/\delta_j\right]J_1\left[(i-1)r_0/\delta_j\right]}$

Table 2.1: Thermoviscous functions for uniform cross-sectional geometries.

2.5 Electroacoustic network analogy

Considering the acoustic volume velocity $U_1 = \langle v_1 \rangle A_f \ [m^3/s]$, where A_f is the fluid cross-sectional area, Eqs. (2.14) and (2.16) can be written as

$$\frac{dp_1}{dx} = -\frac{i\omega\rho_m}{1 - f_\nu}\frac{U_1}{A_f}, \tag{2.21}$$

$$\frac{dU_1}{dx} = -\frac{i\omega A_f}{\gamma p_m}\left[1 + (\gamma - 1)\, f_\kappa\right] p_1. \tag{2.22}$$

At this point Eqs. (2.21) and (2.22) can be combined, eliminating U_1, to obtain a second-order differential equation in p_1

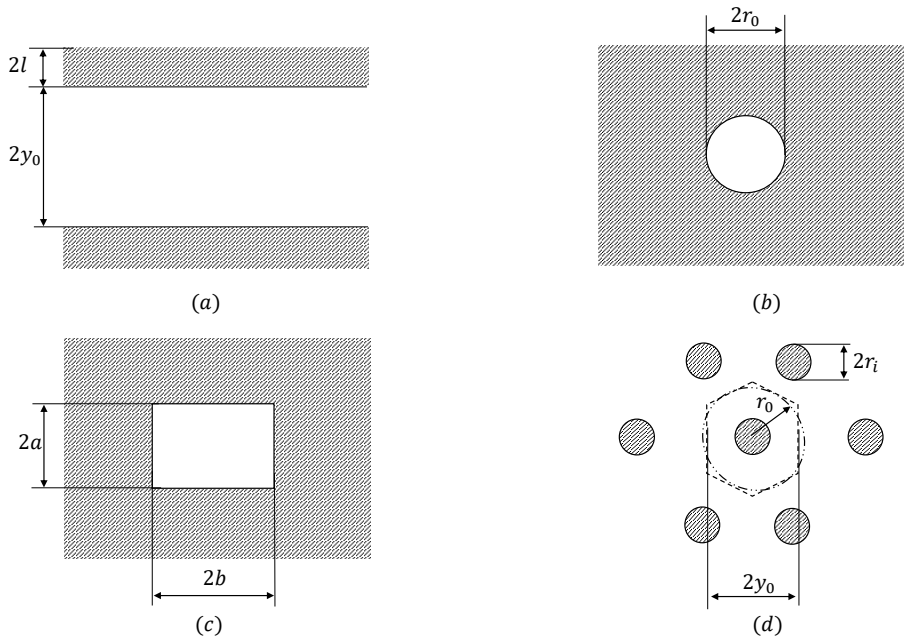

Figure 2.2: Uniform cross-sectional material: (a) parallel plate (or slit), (b) circular pore, (d) rectangular pore, (d) pin array.

$$\frac{d^2 p_1}{dx^2} + \frac{\omega^2 \rho_m}{\gamma p_m} \left[\frac{1 + (\gamma - 1) f_\kappa}{1 - f_\nu} \right] p_1 = 0. \tag{2.23}$$

This is *Rott's wave equation*, which becomes the classical *Helmholtz equation* in the case of mono-directional wave propagation in non-dissipative medium ($f_\nu = f_\kappa = 0$), where $k_A = \omega/c$ is the air wave number,

$$\frac{d^2 p_1}{dx^2} + k_A^2 \, p_1 = 0. \tag{2.24}$$

The acoustic wave propagation inside a dissipative porous material can be described through an electroacoustic analogy by using the acoustic transmission line [19]. A slab of the medium with length dx, much smaller than the acoustic wavelength λ, can be modelled as a lumped acoustic element provided with certain thermo-viscous properties, see Fig. 2.3 up. Eq. (2.21) and (2.22) can be expressed in the following forms

$$dp_1 = (Z_\nu dx) \frac{U_1}{A_f}, \tag{2.25}$$

$$dU_1 = (Y_\kappa dx) \, A_f p_1. \tag{2.26}$$

Z_ν represents the longitudinal impedance per unit length and it is strictly related to the viscous dissipation along the acoustic line

$$Z_\nu = -\frac{i\omega\rho_m}{1 - f_\nu} = -i\omega\tilde{\rho}, \tag{2.27}$$

and the transversal admittance Y_κ per unit length is linked to the thermal losses

$$Y_\kappa = -\frac{i\omega}{\gamma p_m} \left[1 + (\gamma - 1) f_\kappa \right] = -\frac{i\omega}{\tilde{K}}. \tag{2.28}$$

Linking Eqs. (2.27) and (2.28), yields

$$\sqrt{Z_\nu Y_\kappa} = i\omega\sqrt{\frac{\rho_m}{\gamma p_m}}\sqrt{\frac{1+(\gamma-1)\,f_\kappa}{1-f_\nu}} = i\omega\sqrt{\frac{\tilde{\rho}}{\tilde{K}}} = i\tilde{k}, \tag{2.29}$$

$$\sqrt{\frac{Z_\nu}{Y_\kappa}} = \sqrt{\frac{\gamma\rho_m p_m}{(1-f_\nu)\left(1+(\gamma-1)\,f_\kappa\right)}} = \sqrt{\tilde{\rho}\tilde{K}} = \tilde{Z}_c, \tag{2.30}$$

where $\tilde{k}$ and $\tilde{Z}_c$ are the complex wave number and the characteristic impedance of the transmission line (i.e. the porous material), respectively. With the assumption in Eqs. (2.29) and (2.30), Eq. (2.23) can be rearranged in a more compact style as

$$\frac{d^2 p_1}{dx^2} + \tilde{k} p_1 = 0. \tag{2.31}$$

Therefore, as an equivalent network, a porous material can be described as a certain number of double bipole linked in series, at limit an infinite number as reported in Fig. 2.3 down.

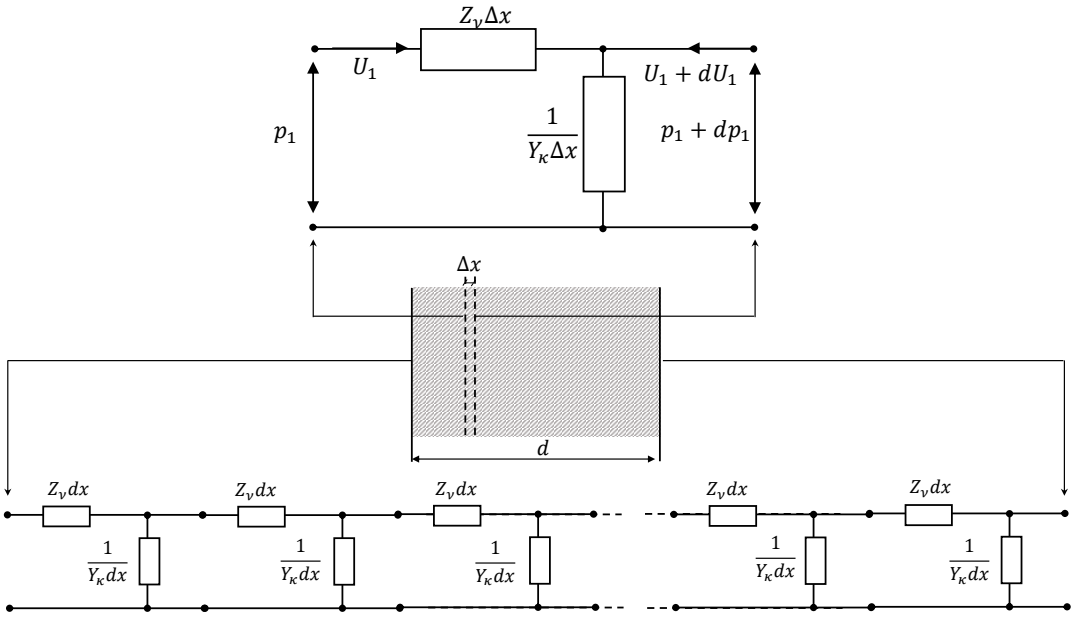

Figure 2.3: Electroacoustic analogy of: (up) a slab of a porous material ($\Delta x \ll \lambda$), and (down) the entire thickness of the sample.

2.5.1 Transfer Matrix approach

The acoustic pressure p_1 and volume velocity U_1 fields inside a porous material can be found from the solution of the second-order differential equation Eq. (2.44). They can be written as the sum of a progressive and regressive waves:

$$p_1(x) = Ae^{-i\tilde{k}x} + Be^{i\tilde{k}x}, \tag{2.32}$$

$$U_1(x) = \frac{A_f}{\tilde{Z}_c}\left[Ae^{-i\tilde{k}x} - Be^{i\tilde{k}x}\right]. \tag{2.33}$$

The Transfer Matrix [20] allows to link the state variable, pressure and volume velocity, between two sides of an acoustic medium (i.e. the back side $x = 0$ and the front side $x = d$, with d being the thickness of the material, Fig. 2.4):

$$\begin{bmatrix} p_1 \\ U_1 \end{bmatrix}_{x=d} = \begin{bmatrix} T_{11} & T_{12} \\ T_{21} & T_{22} \end{bmatrix} \begin{bmatrix} p_1 \\ U_1 \end{bmatrix}_{x=0} \tag{2.34}$$

From an electrotechnical analogy, it follows that

$$T_{11} = p_1(d) \quad \text{with} \quad p_1(0) = 1 \quad \text{and} \quad U_1(0) = 0, \tag{2.35a}$$
$$T_{21} = U_1(d) \quad \text{with} \quad p_1(0) = 1 \quad \text{and} \quad U_1(0) = 0, \tag{2.35b}$$
$$T_{12} = p_1(d) \quad \text{with} \quad p_1(0) = 0 \quad \text{and} \quad U_1(0) = 1, \tag{2.35c}$$
$$T_{22} = U_1(d) \quad \text{with} \quad p_1(0) = 0 \quad \text{and} \quad U_1(0) = 1. \tag{2.35d}$$

Therefore, from Eq. (2.35a) it results

$$p_1(0) = A + B = 1,$$
$$U_1(0) = \frac{A_f}{\tilde{Z}_c}(A - B) = 0,$$

and as a consequence $A = B = \frac{1}{2}$. It follows that

$$T_{11} = p_1(d) = \frac{1}{2}\left(e^{-i\tilde{k}d} + e^{i\tilde{k}d}\right) = \cos\left(\tilde{k}d\right), \tag{2.36}$$
$$T_{21} = U_1(d) = \frac{1}{2}\frac{A_f}{\tilde{Z}_c}\left(e^{-i\tilde{k}d} - e^{i\tilde{k}d}\right) = -i\frac{\tilde{Z}_c}{A_f}\sin\left(\tilde{k}d\right). \tag{2.37}$$

By following the same steps also for Eqs. (2.35c) and (2.35d), the complete Transfer Matrix for a porous material can be written as function of its complex dynamic parameters $\tilde{k}$ and $\tilde{Z}_c$ as

$$\begin{bmatrix} p_1 \\ U_1 \end{bmatrix}_{x=d} = \begin{bmatrix} \cos\left(\tilde{k}d\right) & -i\frac{\tilde{Z}_c}{A_f}\sin\left(\tilde{k}d\right) \\ -i\frac{A_f}{\tilde{Z}_c}\sin\left(\tilde{k}d\right) & \cos\left(\tilde{k}d\right) \end{bmatrix} \begin{bmatrix} p_1 \\ U_1 \end{bmatrix}_{x=0}. \tag{2.38}$$

If a small slice of the material is considered ($d = \Delta x \ll \lambda$), it results from the first-order Taylor expansion series that $T_{11} = T_{22} \approx 1$, $T_{12} \approx -i\tilde{Z}_c\tilde{k}\Delta x/A_f$ and $T_{21} \approx -iA_f\Delta x\tilde{k}/\tilde{Z}_c$ and by using the relations Eqs. (2.29) and (2.30), the Transfer Matrix for an infinitesimal slice of material can be written as

$$\begin{bmatrix} p_1 \\ U_1 \end{bmatrix}_{x=\Delta x} = \begin{bmatrix} 1 & -\frac{i\omega\tilde{\rho}}{A_f}\Delta x \\ -\frac{i\omega A_f}{\tilde{K}}\Delta x & 1 \end{bmatrix} \begin{bmatrix} p_1 \\ U_1 \end{bmatrix}_{x=0}. \tag{2.39}$$

2.6 Thermoacoustics

Theoretical study of thermoacoustic oscillations began in 1868 when Kirchhoff [13] calculated acoustic attenuation in a duct due to oscillatory heat transfer between solid isothermal duct wall and the gas sustaining the sound wave. The first thorough qualitative description of thermoacoustic oscillations was given by Lord Rayleigh. In his work, "The Theory of Sound" [21], he stated:

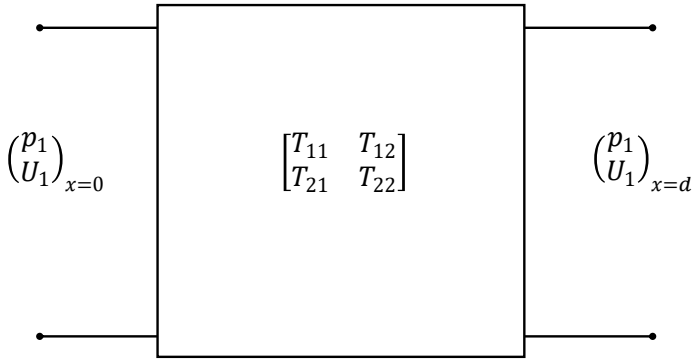

Figure 2.4: Transfer Matrix representation of a porous material.

"If heat be given to air at the moment of greatest condensation or taken from it at the moment of greatest rarefaction, the vibration is encouraged".

Thermoacoustics describes energy conversion processes that arise through the interaction of temperature and pressure oscillations in a sound wave with solid boundaries. In a space where no solid boundary is present, the acoustic oscillation is usually an adiabatic process. In fact, for standard temperature and pressure air and pressure amplitude of typical conversation temperature oscillation is about $10^{-4}\,^{\circ}C$, so it is not surprising that thermoacoustic effects are unnoticed in everyday life. Viscous and thermal boundary layers, however, are formed when a solid boundary is present in an acoustic field. As the fluid oscillates along the plate at the acoustic frequency, it experiences changes in temperature. Part of the temperature changes come from adiabatic compression and expansion of the fluid by the sound pressure and what is left is a consequence of the local temperature of the plate itself. The heat flow between the fluid and the solid boundary does not produce instantaneous changes in fluid temperature,instead, it creates a time delay, or time phasing, between temperature and pressure and motion, which is needed to drive the fluid through a thermodynamic cycle.

2.6.1 Thermoacoustic heat pumping process

Consider a solid plate placed in an acoustic field with direction of particle oscillation along its length as in Fig. 2.5 [6]. Suppose the pressure antinode (region of maximum pressure variation) is near the right end of the plate and the pressure node (region of zero pressure variation) is near the left end of the plate. A typical gas parcel oscillates over a distance ξ_1 about its mean position and its pressure varies between $p_m - p_1$ and $p_m + p_1$. During its displacement the parcel gets compressed and its temperature rises. This parcel then loses heat to the plate till its temperature equals that of the plate. As a result right end of the plate becomes a little warmer. The parcel then moves again to left end where its pressure as well temperature falls. The cold parcel warms up by picking heat from left end of the plate, making the left end of the plate colder. Thus, in one cycle the gas transports δQ amount of heat over a temperature difference of $2\xi_1 \nabla T_m$, absorbing $\delta W_2 - \delta W_1$ amount of acoustic power.

2.6.2 Thermoacoustic devices

Under the right operating conditions thermoacoustic concepts can be applied to realize two kinds of devices: *thermoacoustic refrigerator* (or *heat pump*) that convert sound wave energy in refrig-

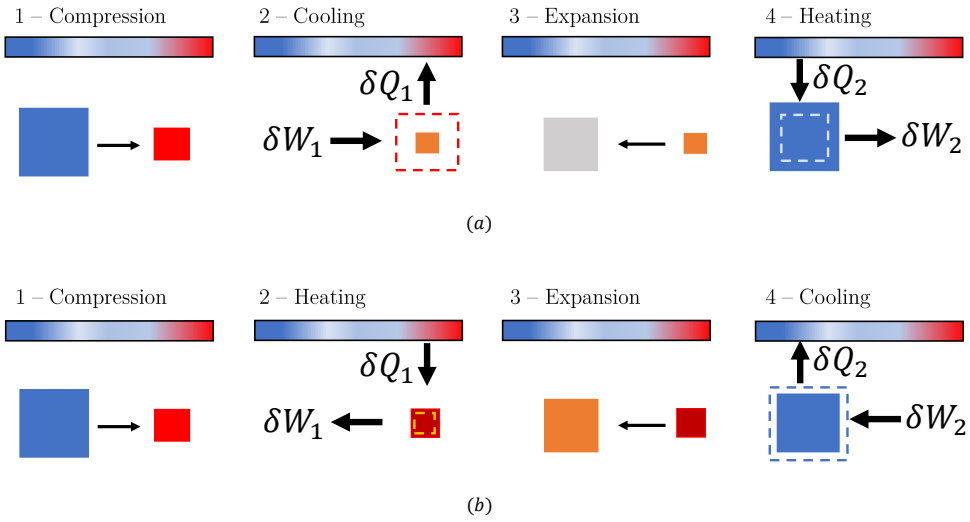

Figure 2.5: Thermoacoustic heat pumping process: (a) standing wave refrigerator, (b) standing wave prime mover.

eration or heating, *thermoacoustic engine* that convert heat in useful work. The energy conversion takes place thanks to the interaction between the oscillating fluid particles and the solid skeleton of a porous material suitable design with respect to the viscous and thermal boundary layer. This porous material, called *stack* or *regenerator*, suitably designed to allow the correct viscous and thermal interactions between the oscillating fluid and its solid surface in order to convert a mechanical energy (as a sound wave) into heat, and *vice versa*. Increasing the efficiency of these devices means to better understand the phenomena which occur in that porous core and then to find the optimal geometry for each specific case. Thermoacoustic devices can also be categorized depending on the phase shift between the pressure and velocity oscillations at the location of the stack. In a closed and empty resonator, such in Fig. 2.6.a, a pure *standing-wave* can be maintained and the pressure and velocity oscillations will be exactly 90 degrees out-of-phase. In an empty infinite tube (or a loop) a pure *traveling-wave* can be maintained, so that the pressure and velocity oscillations are exactly in phase (Fig. 2.6.b). As soon as a stack is inserted in either of these tubes, the phasing between pressure and velocity will change because of partial reflection at the stack interfaces. Moreover, if a looped tube is considered as the type depicted in Fig. 2.6.c, with a resonator tube attached to it, the phasing will be affected even more. Generally, it is beneficial to use a stack inside a standing-wave device, where the pore size of the porous material are of the same order of magnitude of the thermal boundary layer, while a regenerator inside a traveling-wave device, where the pore size are much smaller than the thermal boundary layer. For this reason, thermoacoustic devices are usually classified as either standing-wave stack-based devices or traveling-wave regenerator-based devices.

2.6.3 Mathematical aspects of Thermoacoustics

In thermoacoustics, a static temperature gradient along the porous material, dT_m/dx, is artificially added by means of a hot and a cold heat exchanger. Instead of Eq. (2.8b), in this case the temperature field across the material is written as

$$T(x,y,z,t) = T_m(x) + \Re\left[T_1(x,y,z)e^{i\omega t}\right]. \tag{2.40}$$

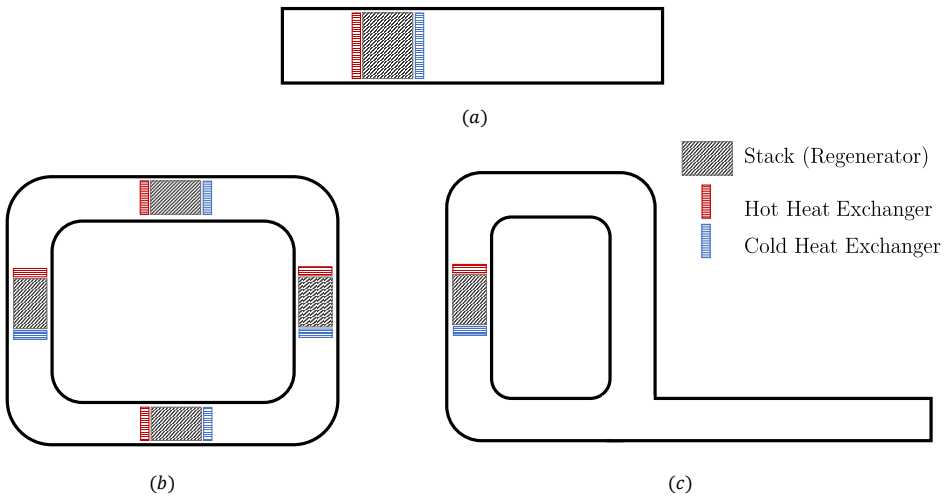

Figure 2.6: Schematic representation of Thermoacoustic devices: (a) pure standing wave device, (b) pure traveling wave device, (c) hybrid standing-traveling wave device.

Taking into account Eq. (2.40), Eq. (2.11) becomes

$$i\omega\rho_m c_p T_1 + \rho_m c_p \frac{dT_m}{dx} v_1 = i\omega p_1 + \kappa \nabla^2 T_1. \tag{2.41}$$

Therefore, the solution of linearized energy equation, Eq. (2.15), changes as

$$\langle T_1 \rangle = \frac{1}{\rho_m c_p} (1 - f_\kappa)\, p_1 + \frac{1}{i\omega A_f} \frac{dT_m}{dx} \frac{(1 - f_\kappa) - P_r\,(1 - f_\nu)}{(1 - f_\nu)\,(1 - P_r)} U_1, \tag{2.42}$$

while the Eq. (2.22) is re-written as

$$\frac{dU_1}{dx} = -\frac{i\omega A_f}{\gamma p_m} \left[1 + (\gamma - 1)\, f_\kappa\right] p_1 + \frac{(f_\kappa - f_\nu)}{(1 - f_\nu)\,(1 - P_r)} \frac{1}{T_m} \frac{dT_m}{dx} U_1. \tag{2.43}$$

By considering the statement from this Eq. (2.43), *Rott's wave equation* Eq. (2.23) is completed by another terms function of the applied thermal gradient across the porous material

$$\frac{d}{dx}\left(\frac{1 - f_\nu}{\rho_m} \frac{dp_1}{dx}\right) - \frac{(f_\kappa - f_\nu)}{(1 - P_r)} \frac{1}{\rho_m T_m} \frac{dT_m}{dx} \frac{dp_1}{dx} + \frac{\omega^2}{\gamma p_m} \left[1 + (\gamma - 1)\, f_\kappa\right] p_1 = 0. \tag{2.44}$$

This latter equation takes into account the variation along the x coordinate of the static values of all thermodynamic quantities, such as the density $\rho_m = \rho_m(x)$, the boundary layers $\delta = \delta(x)$ and the thermoviscous function $f = f(x)$.

Electroacoustic analogy in Thermoacoustics

Based on the Eq. (2.43), the Eq. (2.28) is now modified due to an added term on the right side of the equation

$$dU_1 = (Y_\kappa dx)\, A_f p_1 + g dx U_1, \tag{2.45}$$

where the new term g represents a sort of complex gain/attenuation constant for volume flow rate proportional to the local volume flow rate U_1 itself, and which arises only when the temperature gradient dT_m/dx along the channel is nonzero. Therefore, the representation of the network changes as in Fig. 2.7.

$$g = \frac{(f_\kappa - f_\nu)}{(1 - f_\nu)(1 - P_r)} \frac{1}{T_m} \frac{dT_m}{dx}. \tag{2.46}$$

This quantity has effect also on the electroacoustic analogy expressed by the transversal source element added. Therefore, the Transfer Matrix for an infinitesimal slice of porous material with an applied thermal gradient becomes from Eq. (2.47) to

$$\begin{bmatrix} p_1 \\ U_1 \end{bmatrix}_{x=\Delta x} = \begin{bmatrix} 1 & -\frac{i\omega\tilde{\rho}}{A_f}\Delta x \\ -\frac{i\omega A_f}{\tilde{K}}\Delta x & 1 + g\Delta x \end{bmatrix} \begin{bmatrix} p_1 \\ U_1 \end{bmatrix}_{x=0}. \tag{2.47}$$

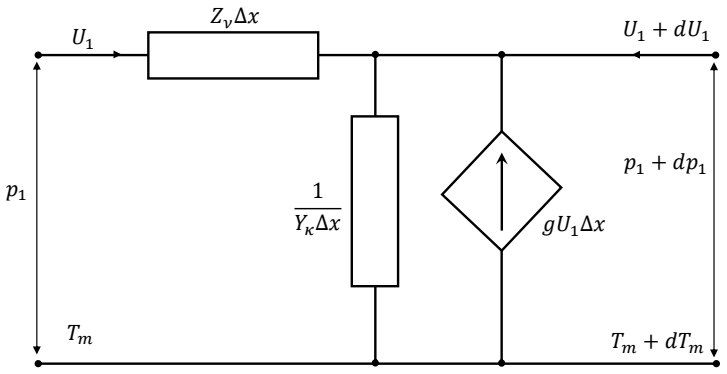

Figure 2.7: Electroacoustic analogy of a slab of a porous material subjected to a thermal gradient in a thermoacoustic device.

2.6.4 Analysis of heat capacity ratio in porous media

Porous cores in thermoacoustic engines (or heat pumps) are assumed to act as thermal reservoirs and to have isothermal behavior compared to oscillating gas parcels, meaning that a first-type Dirichlet boundary condition, expressed by Eq. (2.13b), is applied at the fluid-solid interface. In literature, to take into account of *imperfect* isothermal condition of solid skeleton of the material, Swift [6] introduced the *heat capacity ratio* parameter ϵ_s, obtained from the solution of the solid and fluid thermal field in the frequency domain. Therefore, the energy differential equation Eq. (2.41) is coupled with the energy equation describing the solid matrix temperature field

$$i\omega T_{1,s} = \frac{\kappa_s}{\rho_s c_s} \nabla^2 T_{1,s}. \tag{2.48}$$

$T_{1,s}$ represents the oscillating first-order term of the temperature of the solid skeleton

$$T_s = T_{m,s}(x) + \mathbb{R}\left[T_{1,s}(x, y, z) e^{i\omega t}\right], \tag{2.49}$$

and κ_s, ρ_s, c_s are respectively the thermal conductivity, the density and the specific heat of the solid material. Eqs. (2.41) and (2.48) are solved with a third type Robin boundary condition, taking into account that the oscillating temperature of the solid and fluid phase are equal and the heat flux of the two phases are opposite

$$\begin{cases} T_1 = T_{1,s} & \text{on} \quad \Omega_{fs}, \\ \kappa \dfrac{dT_1}{dx} = -\kappa_s \dfrac{dT_{1,s}}{dx} & \text{on} \quad \Omega_{fs}. \end{cases} \tag{2.50}$$

Based on these boundary conditions, the solution of energy equation, Eq. (2.42), becomes

$$\langle T_1 \rangle = \frac{1}{\rho_m c_p} \left(1 - \frac{f_\kappa}{1+\epsilon_s}\right) p_1 + \frac{1}{i\omega A_f} \frac{dT_m}{dx} \frac{\left[1 - \frac{f_\kappa}{1+\epsilon_s}\left(1 + \epsilon_s \frac{f_\nu}{f_\kappa}\right)\right] - P_r\,(1-f_\nu)}{(1-f_\nu)\,(1-P_r)} U_1, \tag{2.51}$$

while the averaged thermal field in the solid skeleton can be written from the analogue solution of the Eq. (2.48)

$$\langle T_{1,s} \rangle = T_{1,s}\big|_{\text{on } \Omega_{fs}}\, f_s. \tag{2.52}$$

Similarly to the dynamic thermal function f_κ of the fluid part, f_s is the dynamic thermal function representing the temperature fields inside the solid material and it depends both on the solid skeleton geometry and the *solid thermal penetration depth* $\delta_s = \sqrt{2\kappa_s/(\rho_s c_s \omega)}$, analogous to the thermal boundary layer δ_κ. For simple uniform cross-sectional geometry, it can be analytically derived. The *heat capacity ratio* parameter ϵ_s takes into account the thermal properties of the materials and the fact that its finite heat capacity does not allow the solid to be considered as a thermal energy tank. From an operative point of view, it can be evaluated as [22]

$$\epsilon_s = \frac{\rho_m c_p}{\rho_s c_s} \frac{f_\kappa}{f_s} \frac{\varphi}{1-\varphi}, \tag{2.53}$$

where $\varphi = V_f / \left(V_f + V_s\right)$ is the porosity of the porous medium, V_f and V_s the fluid and solid volume fraction respectively. In the following discussion, parallel plate geometry is taken into account (y_0 and l are respectively the semi-distance between two contiguous plates and the semi-width of the plate, see Fig. 2.2.a), where f_s has the same analytical description of f_κ for slits (reported in Tab. 2.1) and replacing δ_κ with δ_s. When $\epsilon_s \to 0$, the solid matrix has enough heat capacity to guarantee isothermal boundary condition $\left(T_{1,s} = 0\right)$ at the solid-fluid interface. In this case, through the whole solid section amplitude oscillation is almost equal to zero, Fig. 2.8. In this condition, the oscillating heat exchanged between fluid and solid is maximum. On contrary, $|\epsilon_s| \to \infty$ when solid has such low thermal capacity that an adiabatic boundary condition can be adopted ($dT_{1,s}/dx = 0$ on Ω_{fs}) as shown in Fig. 2.9, where in fluid there are no spatial gradients. In thermoacoustic cores (used for energy conversion) this is unwanted, because no thermoacoustic effect is possible without interaction between oscillating fluid and solid wall as a thermal energy tank. Between these two extreme cases, more in general there are spatial temperature gradients (and therefore time oscillation) both in the solid and in the fluid. The solid mean temperature lags behind the fluid mean temperature (Fig. 2.10). In all the three previous cases pictured in Figs. 2.8, 2.9 and 2.10, temperature oscillations T_1, y coordinate and time t are considered dimensionless with respect to adiabatic temperature $T_a = p_1 / \left(\rho_m c_p\right)$, $y_0 + l$, and frequency f respectively, so that trends are independent of pressure input p_1, physical lengths y_0, l and frequency f. At the fluid-solid interface, temperature gradient is not continuous because thermal conductivities are different.

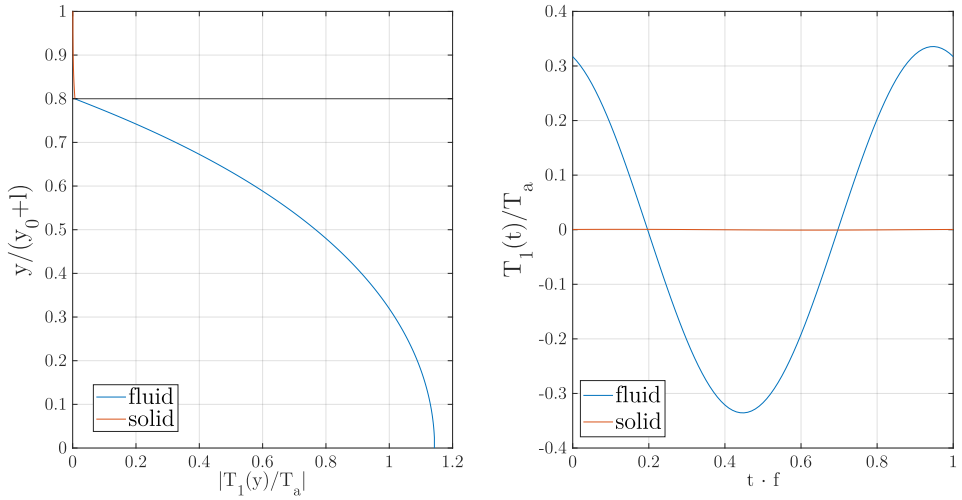

Figure 2.8: Distribution of module of temperature oscillations (left), time oscillations (right), in the *quasi*-isothermal case: $y_0/\delta_\kappa = 2, \quad l/\delta_s = 3, \quad \varepsilon_s = 0.0047$.

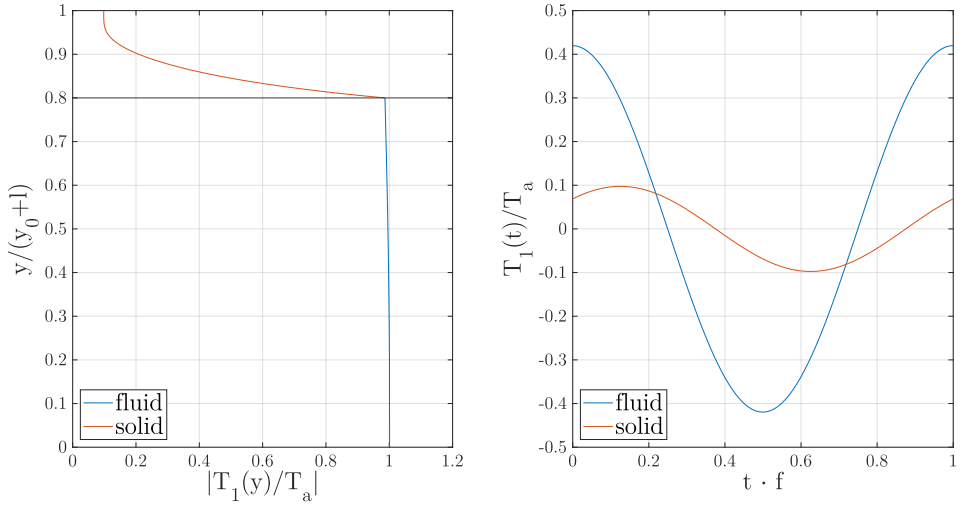

Figure 2.9: Distribution of module of temperature oscillations (left), time oscillations (right), in the *quasi*-adiabatic case: $y_0/\delta_\kappa = 2, \quad l/\delta_s = 3, \quad \varepsilon_s = 47$.

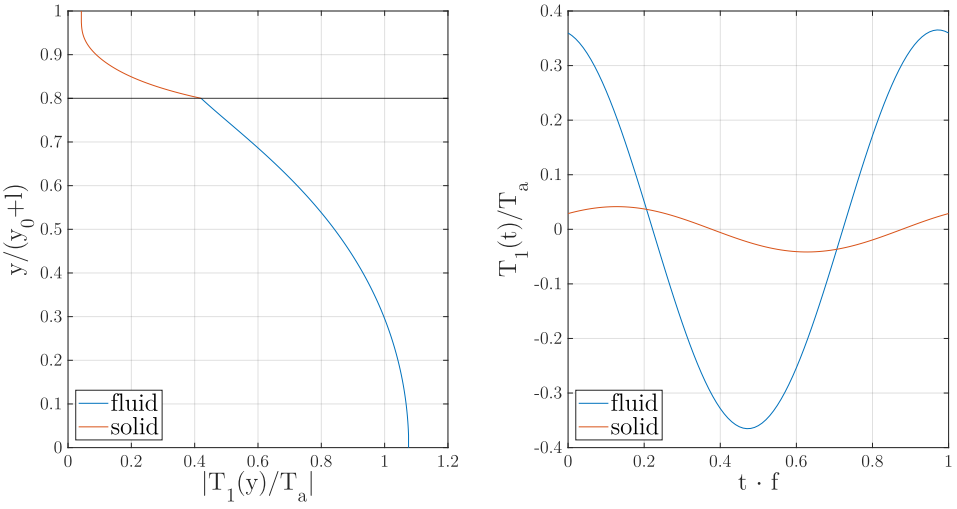

Figure 2.10: Distribution of module of temperature oscillations (left), time oscillations (right), in the general case: $y_0/\delta_\kappa = 2, \quad l/\delta_s = 3, \quad \varepsilon_s = 0.47$.

Chapter 3

The Equivalent Fluid Model

Contents

3.1 Introduction

As reported in Sec. 2, the complete characterization of acoustic porous media requires two dynamic frequency-depending parameters: the thermoviscous functions, or equivalently the dynamic friction factor and Nusselt number, or the complex density and the complex bulk modulus. As it will be shown in this Section, dynamic behaviour of a porous material can be also expressed in the same way by the dynamic viscous and thermal tortuosity, or the dynamic viscous and thermal permeability). In acoustics, different models have been developed to describe sound propagation in porous media. For simple uniform cross-section, such as circular pore, parallel slit, pin array, analytical solutions are available in literature depending only on geometrical parameters. For random porous media, such as high porosity fibers, empirical correlations are provided by Delany and Bezley [23], further revisited by Miki [24], where the airflow resistivity σ is required as input parameter. Said f the sound frequency, this empirical model can be considered reliable in the range $0.01 < f/\sigma < 1$, elsewhere it returns non-physical results. Wilson [25] defined a middle frequency range model through the definition of the vorticity-mode relaxation time, and the entropy-mode relaxation time. This model does not fit the asymptotic behaviour in the low and high frequency range. Semi-phenomenological models have been developed to characterize the behaviour of a general porous structure through the knowledge of static parameters, so-called transport, non-acoustical, parameters. In literature, the most used semi-phenomenological model is the Johnson-Champoux-Allard-Lafarge [26, 27, 28] model (referred from this point as JCAL, for brevity). It requires the knowledge of six parameters: the porosity φ, the airflow resistivity σ (equivalent to the static viscous permeability $k_0 = \mu/\sigma$), the thermal Λ' and viscous Λ characteristic lengths, the high frequency limit of tortuosity α_∞ and the static thermal permeability k_0'. These latter parameters link the microstructural feature of the porous medium with its macroscopic behaviour. They are strictly linked with the high and low frequency asymptotic behaviour of the material. JCAL model can be considered valid in the whole acoustic frequency range. Furthermore, Pride [29] introduced other two parameters, the static thermal α_0' and viscous α_0 tortuosity, to improve the low frequency description in case of pores with possible constriction (so-called JCAPL model). The reasons why JCAL model is the most used one in literature are its frequency range validity and the possibility to evaluate both numerically and experimentally all the transport parameters involved. The complete model (JCALP) is not diffused due to the impossibility to measure experimentally and to verify Pride's parameters values. They can be only evaluated numerically, but the precise geometry is required. The outline of the Section 3 is reported in follows. In subsection 3.2, the empirical models provided for different kind of materials are summarized. In subsection 3.3 the Johnson-Champoux-Allard-Lafarge semi-phenomenological model is recalled with its asymptotic limit for complex density and bulk modulus. The definitions of each transport parameters are given in subsection 3.4. Subsection 3.5 shows experimental techniques to assess non-acoustical parameters, while computational approaches to evaluate them are presented in subsection 3.6.

3.2 Empirical models

Delany and Bazley [23] developed a simple empirical model of the acoustic complex characteristic impedance and wave number of a porous material based on its airflow resistivity σ. The model is based on numerous impedance tube measurements (see Sec. 5) in order to obtain robust constant for statistical regression procedure. The mathematical structures of the correlations are

$$\tilde{Z}_c = \rho_m c \left[1 + C_1 \chi^{-C_2} - i C_3 \chi^{-C_4}\right] \tag{3.1}$$

$$\tilde{k} = \frac{\omega}{c}\left[1 + C_5\chi^{-C_6} - iC_7\chi^{-C_8}\right] \tag{3.2}$$

where $0.01 < \chi = \frac{\rho_m f}{\sigma} < 1$ expresses the validity range proposed by Delany and Bazley. The validity of this model for lower and higher frequencies was further extended by Bies and Hansen [30]. Subsequently Miki [24], Garai and Pompoli [31], Dunn and Davern [32] provided different values of the constants $C_1 - C_8$ for various materials. These constants are reported in Table 3.1.

Material type reference	C_1	C_2	C_3	C_4	C_5	C_6	C_7	C_8
Rockwool/fiberglass (Delany and Bazley)	0.0571	0.745	0.087	0.732	0.0978	0.700	0.189	0.595
Rockwool/fiberglass (Miki)	0.070	0.632	0.107	0.632	0.160	0.618	0.109	0.618
Polyester fiber (Garai and Pompoli)	0.078	0.623	0.074	0.660	0.159	0.571	0.121	0.530
Polyurethane foam (Dunn and Davern)	0.114	0.369	0.099	0.758	0.168	0.715	0.136	0.491

Table 3.1: Values of parameters $C_1 - C_8$ for different empirical models.

3.3 Semi-phenomenological models

The semi-phenomenological Johnson-Champoux-Allard-Lafarge model provides a separated description of the dynamic viscous and thermal behaviour of a porous medium through respectively the complex density $\tilde{\rho}$ (equivalent to complex viscous permeability $\tilde{k}_\nu$ and complex viscous tortuosity $\tilde{\alpha}$) and the complex bulk modulus $\tilde{K}$ (or which is the same, complex thermal permeability $\tilde{k}'$ and complex thermal tortuosity $\tilde{\alpha}'$).

3.3.1 Johnson *et al.* model

Johnson, Koplik and Dashen [26] provided the analytic properties of the viscous behaviour of a porous material subjected to an infinitesimal oscillatory pressure gradient. In this work, an analytical formulation for the complex density $\tilde{\rho}$ is derived for the entire frequency range, starting from the exact high- and low- frequency parameters, k_0 and (α_∞, Λ) respectively. For visco-inertial effects, it results

$$\tilde{\rho} = \frac{\rho_m \alpha_\infty}{\varphi}\left[1 - i\frac{\omega_\nu}{\omega}\tilde{G}\right], \tag{3.3}$$

where

$$\tilde{G} = \sqrt{1 + \frac{1}{2}iM\frac{\omega}{\omega_\nu}}, \tag{3.4a}$$

$$M = \frac{8k_0\alpha_\infty}{\varphi\Lambda^2}, \tag{3.4b}$$

$$\omega_\nu = \frac{\mu\varphi}{\rho_m k_0 \alpha_\infty}. \tag{3.4c}$$

M and ω_ν are respectively the *viscous pore shape factor* and *viscous reduced frequency*. They allow to express the the complex viscous behaviour of a porous material by using dimensionless

parameters. The equivalence between dynamic viscous parameters can be expressed through the Darcy's law in dynamic regime and the definition of dynamic tortuosity as follow

$$\tilde{k}_\nu = \frac{\delta_\nu^2}{2i}\frac{\rho_m}{\tilde{\rho}}, \tag{3.5a}$$

$$\tilde{\alpha} = \frac{\tilde{\rho}}{\rho_m}, \tag{3.5b}$$

$$\tilde{k}_\nu = \frac{\delta_\nu^2}{2i\tilde{\alpha}}. \tag{3.5c}$$

In the description of dynamic viscous behaviour of sound propagating in a porous material, it can be highlighted that viscous losses prevail on inertia effects on low frequency and vice versa in high frequency regime. The high and low frequencies are related to the thermal and viscous boundary layer compared to the medium pore dimension, or a hydraulic radius $\left(\bar{r} \approx \Lambda'\right)$ taken as length reference. At low frequency limit, for $\Lambda'/\delta_\nu \to 0$, complex density at first order approximation can be written as

$$\tilde{\rho} = \frac{\rho_m}{\varphi}\left[\frac{\varphi}{2i}\frac{\delta_\nu^2}{k_0} + \alpha_\infty\left(1 + \frac{2k_0\alpha_\infty}{\varphi\Lambda^2}\right)\right] = \frac{\rho_m\alpha_\infty}{\varphi}\left(-i\frac{\omega_\nu}{\omega} + 1 + \frac{M}{4}\right). \tag{3.6}$$

and combining with Eq. (3.5a), it follows that

$$\tilde{k}_\nu = \left[\frac{1}{k_0} + \frac{2i\alpha_\infty}{\varphi\delta_\nu^2}\left(1 + \frac{2k_0\alpha_\infty}{\varphi\Lambda^2}\right)\right]^{-1}. \tag{3.7}$$

At high frequency limit, for $\Lambda'/\delta_\nu \to \infty$, inertial effects prevail on viscous behaviour, and complex density can be express as

$$\tilde{\rho} = \frac{\rho_m\alpha_\infty}{\varphi}\left[1 + (1-i)\frac{\delta_\nu}{\Lambda}\right] = \frac{\rho_m\alpha_\infty}{\varphi}\left[1 + \frac{(1-i)}{2}\sqrt{\frac{\omega_\nu}{\omega}M}\right]. \tag{3.8}$$

As a consequence, the dynamic viscous tortuosity in high frequency approximation becomes

$$\tilde{\alpha} = \alpha_\infty\left[1 + (-i)\frac{\delta_\nu}{\Lambda}\right]. \tag{3.9}$$

3.3.2 Champoux-Allard-Lafarge model

Champoux and Allard [27] extended the concept of characteristic length introduced in the definition of the dynamic tortuosity by Johnson *et al.* to express the frequency dependence of the bulk modulus of the saturating fluid at high frequencies. Lafarge [28] improved the semi-phenomenological formulation provided by Champoux and Allard by adding the dependece from an another parameter, the static thermal permeability k_0'. Based on these assumptions, and by using an analogous dimensionless formulation as for the viscous behaviour, the dynamic bulk modulus can be written as

$$\tilde{K} = \frac{\gamma p_m/\varphi}{\gamma - (\gamma-1)\left[1 - i\frac{\omega_\kappa}{\omega}\tilde{G}'\right]^{-1}}, \tag{3.10}$$

where in this case

$$\tilde{G}' = \sqrt{1 + \frac{1}{2} i M' \frac{\omega}{\omega_\kappa}}, \tag{3.11a}$$

$$M' = \frac{8 k_0'}{\varphi \Lambda'^2}, \tag{3.11b}$$

$$\omega_\kappa = \frac{\kappa \varphi}{\rho_m c_p k_0'}. \tag{3.11c}$$

M' and ω_κ are respectively the *thermal pore shape factor* and *thermal reduced frequency*. Considering the equivalent *thermal* Darcy's law introduced by Lafarge (reported in the following subsection), the dynamic thermal permeability and thermal tortuosity result

$$\tilde{k}' = \frac{\delta_\kappa^2}{2i} \frac{\gamma}{\gamma - 1} \left(1 - \frac{p_m}{\tilde{K}} \right), \tag{3.12a}$$

$$\alpha' = \frac{\gamma - 1}{\gamma} \left(1 - \frac{p_m}{\tilde{K}} \right)^{-1}, \tag{3.12b}$$

$$\tilde{k}' = \frac{\delta_\kappa^2}{2 i \alpha'}. \tag{3.12c}$$

Thermal characterization of a porous material moves from an isothermal (low frequency, $\Lambda'/\delta_\kappa \to 0$) to adiabatic (high frequency, $\Lambda'/\delta_\kappa \to \infty$) behaviour. Therefore, Eq. (3.10) becomes in low frequency approximation as

$$\tilde{K} = \frac{\gamma p_m / \varphi}{\gamma - (\gamma - 1) \left(\frac{\varphi}{2i} \frac{\delta_\kappa^2}{k_0'} + 1 + \frac{2 k_0'}{\varphi \Lambda'^2} \right)^{-1}} = \frac{\gamma p_m / \varphi}{\gamma - (\gamma - 1) \left(-i \frac{\omega_\kappa}{\omega} + 1 + \frac{M'}{4} \right)^{-1}}, \tag{3.13}$$

and substituting this equation in Eq. (3.12a), it follows that

$$\tilde{k}' = \left[\frac{1}{k_0'} + \frac{2i}{\varphi \delta_\kappa^2} \left(1 + \frac{2 k_0'}{\varphi \Lambda'^2} \right) \right]^{-1}. \tag{3.14}$$

In the high frequency limit, the bulk modulus can be written as

$$\tilde{K} = \frac{\gamma p_m / \varphi}{\gamma - (\gamma - 1) \left[1 - (1 - i) \frac{\delta_\kappa}{\Lambda'} \right]} = \frac{\gamma p_m / \varphi}{\gamma - (\gamma - 1) \left[1 - \frac{(1-i)}{2} \sqrt{\frac{\omega_\kappa}{\omega}} M' \right]}. \tag{3.15}$$

Equivalently to Eq. (3.9), also the thermal tortuosity can be reported in the high frequency limit

$$\alpha' = \left[1 - (1 - i) \frac{\delta_\kappa}{\Lambda'} \right]. \tag{3.16}$$

As it can be seen from Eqs. (3.6),(3.8), (3.13), and (3.15), low and high frequency dynamic behaviour of porous material are described respectively from the permeabilities and the high frequency limit of tortuosity and the characteristic lengths. Generally, porous material for acoustic applications should be characterized by M and M' with order of magnitude around 1 (equal to 1 for straight cylindrical pore). In Figs. 3.1, 3.2, dimensionless complex density $\tilde{\rho}/\rho_m$ and bulk modulus $\tilde{K}/p_m$ are reported respectively versus the dimensionless frequencies axes ω/ω_ν and ω/ω_κ, as function of the set of quantities $\left(M, M', \alpha_\infty, \gamma, \varphi\right)$ to be independent from fluid properties.

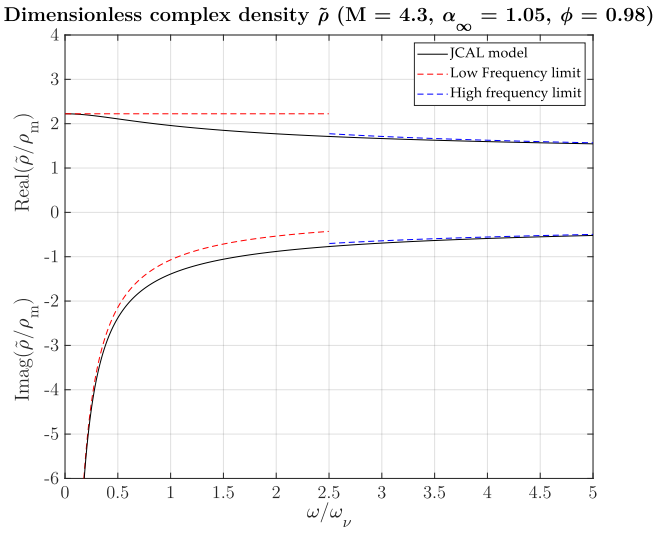

Figure 3.1: Dimensionless complex density $\tilde{\rho}/\rho_m$ from JCAL model.

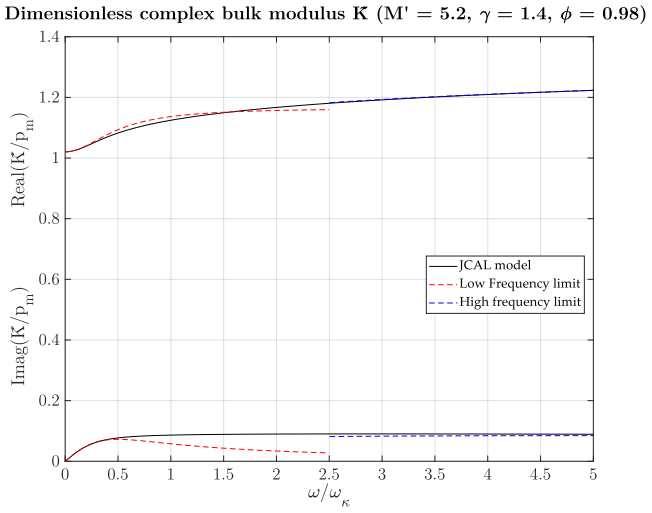

Figure 3.2: Dimensionless complex density $\tilde{K}/p_m$ from JCAL model.

3.3.3 Pride *et al.* model

Pride [29] corrected the low frequency description of JCAL model by adding two static parameters: the static thermal α'_0 and viscous tortuosity α_0. Therefore, in the so-called Johnson-Champoux-Allard-Pride-Lafarge (JCAPL) model eight input parameters are required and Eqs. (3.3) and (3.10) become

$$\tilde{\rho} = \frac{\rho_m \alpha_\infty}{\varphi}\left[1 - i\frac{\omega_\nu}{\omega}\tilde{D}\right], \tag{3.17}$$

$$\tilde{K} = \frac{\gamma p_m/\varphi}{\gamma - (\gamma-1)\left[1 - i\frac{\omega_\kappa}{\omega}\tilde{D}'\right]}, \tag{3.18}$$

where

$$\tilde{D} = 1 - P + P\sqrt{1 + \frac{iM}{2P^2}\frac{\omega}{\omega_\nu}} \tag{3.19a}$$

$$\tilde{D}' = 1 - P' + P'\sqrt{1 + \frac{iM'}{2P'^2}\frac{\omega}{\omega_\kappa}} \tag{3.19b}$$

$$P = \frac{M}{4\left(\frac{\alpha_0}{\alpha_\infty} - 1\right)} \tag{3.19c}$$

$$P' = \frac{M'}{4\left(\alpha'_0 - 1\right)} \tag{3.19d}$$

By setting $P = P' = 1$, JCAPL model recovers JCAL model. In literature, there are no direct (experimental) or indirect method (see Chap. 3) to assess α'_0 and α_0 values, and they can only be evaluated from a numerically point of view once the geometry is known. Due to these reasons, Pride modification of JCAL model is not so used in literature.

3.4 Definitions of transport parameters

3.4.1 Porosity

The porosity is defined as the relative fraction, by volume, of air contained within the material, and it can be operatively written as the ratio between the fluid part volume V_f and the total volume of the material V_t

$$\varphi = \frac{V_f}{V_t} = \frac{V_f}{V_f + V_s} = 1 - \frac{\rho_b}{\rho_m} \tag{3.20}$$

where V_s is the volume occupied by the solid skeleton. At the same time, porosity can be defined also considering the complement to unit of the ratio between the bulk density ρ_b of material and the density of the solid skeleton ρ_s.

3.4.2 Airflow resistivity

Static viscous permeability is defined as the low frequency limit of the dynamic viscous permeability $\tilde{k}_\nu$, Eq. (3.7) to characterize the dynamic behaviour of Darcy's law in frequency domain

$$\varphi\langle v\rangle = \frac{\tilde{k}_\nu}{\mu}\nabla p. \tag{3.21}$$

Dynamic viscous permeability is defined as a second order symmetric tensor due to its definition based on two vectorial quantities such as acoustic particle medium velocity $\langle v\rangle$ and the pressure gradient along a direction ∇p. The static viscous permeability is the reference value respect to the direction of wave propagation, and it is strictly related to the airflow resistivity from the relation

$$\sigma = \frac{\mu}{k_0}. \tag{3.22}$$

Airflow resistivity represents the most common parameters in the description of flow across porous media. It is defined as the ratio between static pressure gradient and the fluid velocity across the material

$$\sigma = \frac{\Delta p}{d\langle v\rangle} \tag{3.23}$$

where d is the sample thickness. Airflow resistivity unit is $Rayls$ (equal to $\left[Pa \cdot s/m\right]$), while permeability has the dimension of an area m^2.

3.4.3 Thermal characteristic length

Thermal characteristic length is a geometrical quantity defined as twice the ratio between the volume of fluid V on the fluid-solid wet surface $\partial\Omega$ (a generalized hydraulic radius)

$$\Lambda' = 2\frac{\int_V dV}{\int_{\partial\Omega} d\Omega}. \tag{3.24}$$

This parameter allows to describe the thermal exchange between fluid and solid skeleton due to the thermal effect generated by the compression and the rarefaction of particles. In particular, in high frequency limit thermal effects can been seen only near the wall of the skeleton of the porous material [26].

3.4.4 Viscous characteristic length

Viscous characteristic length is defined in the high frequency limit where the effect of viscosity is overcome by the forces of inertia. Due to this fact, it is defined as twice the ratio of the weighted by the velocity in the volume to that of the surface of an inviscid (no viscosity) fluid [26]

$$\Lambda' = 2\frac{\int_V v dV}{\int_{\partial\Omega} v d\Omega}. \tag{3.25}$$

3.4.5 High frequency limit of tortuosity

The high frequency limit of tortuosity (or tortuosity) depends on the microgeometry of the porous frame and is a dimensionless parameter. When the effect of viscosity becomes negligible, at high frequency when the viscous penetration depth tends to zero, the effective fluid density tends to $\rho_m\alpha_\infty$. Tortuosity is defined in the case of inviscid fluid as [26]

$$\alpha_\infty = \frac{\frac{1}{V_f}\int_V |v^2| dV}{\left(\frac{1}{V_f}\int_V |v| dV\right)^2}. \tag{3.26}$$

3.4.6 Static thermal permeability

Lafarge [28] introduced the dynamic thermal permeability $\tilde{k}'$ to improve the description of low frequency thermal behaviour of porous media, by setting an analogous *thermal* Darcy's law similar to Eq. (3.21)

$$\varphi\langle T\rangle = \frac{\tilde{k}'}{\kappa}\frac{\partial p}{\partial t}, \tag{3.27}$$

where $\langle T\rangle$ is the acoustic oscillating temperature averaged in the sample. Analogously, static thermal permeability $k_0{}'$ is defined as the low frequency limit of the thermal dynamic permeability, Eq. (3.14). The description of thermal behaviour involves scalar quantities such as the acoustic pressure and temperature fields. Therefore, thermal permeability is a scalar quantity depending only on the microgeometry of the material. In his work, Torquato pointed out the relations between the permeability and the trapping constant Γ of porous media [33]

$$k_0{}' = \frac{1}{\Gamma}. \tag{3.28}$$

In diffusion-controlled reactions problems, trapping constant is defined

$$\Gamma = \frac{s}{\varphi\langle m\rangle D}, \tag{3.29}$$

where D and s are respectively the diffusion coefficient and the rate of production of reactant in a steady-state fluid region with volume $\mathrm{d}V$ and $\partial\Omega$ the boundary surface between fluid and solid

$$D\nabla^2 m = -s \quad \text{in} \quad \mathrm{d}V, \tag{3.30a}$$

$$m = 0 \quad \text{in} \quad \partial\Omega. \tag{3.30b}$$

3.5 Measurement techniques

Different measurement techniques have been developed to assess the values of transport parameters for porous materials. Direct methods refer to methodologies which allow to directly estimate a parameter. Indirect method is based on the acoustical inversion of complex density and bulk modulus in order to assess all the transport parameters from the expressions given by Panneton and Olny [34, 35]. Inverse methods are based on optimization model to find out the best set of transport parameters that fit experimental curves.

3.5.1 Direct methods

Different experimental techniques to evaluate each transport parameter are reported in the following.

Porosity

Different approaches are adopted in the measurement of porosity. Beranek [36] proposed a method based on the height of the water in the two sides of the U-manometer linked to a chamber containing the sample, Fig. 3.3.a. This device was based on the equation of state for ideal gases. Panneton [37] provided a pressure/mass method based on four measurements in different operating conditions. Acoustical methodologies to assess the porosity value of a porous material are provided by Umonva *et al.* [38] and Fellah *et al.* [39]. In both papers, porosity and tortuosity are determined. The first one uses pulses with central frequencies close to 12 kHz, since in high frequency the inertial effects dominate over the viscous one in the sound propagation.

Airflow resistivity

Different experimental methodologies have been developed to assess the airflow resistivity of porous material. The most used technique is essentially based of the measuring the pressure across the material sustaining a constant volume velocity [40, 41], as shown in Fig. 3.3.b. The ASTM C522 [40] provides a Standard Test Method for airflow resistance of acoustical materials with $\sigma = 100 \div 10000\ Rayls$. The test requires a suction generator, a flowmeter and differential pressure measuring device low linear velocity $\left(< 50\ mm/s\right)$ and low-pressure difference across the sample (250 Pa) are required to avoid turbulence and non-linear effect. Bies and Hansen [30] also reproduced the set up reported in ASTM C522 and provided technical tips to take into account the typology of material (hard or soft skeleton) and to avoid air losses. Another method based on alternating airflow has also been standardized by ISO 9053-2 [42]. This method requires an oscillating piston which generates an alternating flow across the sample at the frequency of 2 Hz (Fig. 3.3.c). Dragonetti *et al.* [43] showed the possibility to evaluate airflow resistivity though an equivalent electro-acoustic network, by measuring the pressure inside the cavity in which the sample is placed in and the acoustic volume velocity with the pressure in the back cavity of the

loudspeaker, as shown in Fig. 3.3.d. In a range where the imaginary part of the ratio between these two acoustic pressures is linear with the frequency, airflow resistivity can be estimated as

$$\sigma = -\frac{\Im\left(\frac{p_{up}}{p_{dw}}\right)}{\frac{\omega V_{dw}}{\gamma p_m S} d} \tag{3.31}$$

Where V_{dw} and S are respectively the air volume of the back cavity of the loudspeaker and the cross-sectional area of the tube where the sample is placed.

High frequency limit parameters

Ultrasonic measurement set up are provided to assess the values of the characteristic lengths and the tortuosity, see Fig. 3.3.e. In the works of Leclaire *et al.* [44] and Fohr *et al.* [45], a method based on the utilizing the difference in physical properties of air and helium combining with high frequency limit of both viscous and thermal behaviour allows to evaluate the characteristic lengths. Due to linear behaviour of wavenumber at high frequencies (70–600 kHz), two slope, expressed in terms of Λ' and Λ, are obtained [Eq. (2), Ref. [44]]. Fohr *et al.* [45] carried out the measurement by positioning the sample between two ultrasonic transducers (40 kHz), one emitter and one receiver, as shown in Fig. 8. Two measures are carried out: with and without the tested samples. The relative time delay and amplitude attenuation caused by the tested material allow to extract both characteristic lengths and tortuosity [Eqs. (6) and (7), Ref. [45]], always based on the mathematical description of high frequency limit behaviour.

Static thermal permeability

Henry and Allard [46] and Debray *et al.* [47] showed an acoustic method to measure the trapping constant based on the low frequency limit of the bulk modulus (defined in terms of compressibility), see. Eq. (11) in Ref. [47]. This method replaces Tarnow's acoustic set up [48] for the measurement of compressibility based on the variations of the resonance frequencies in a cylindrical tube with and without the testing sample.

3.5.2 Indirect methods

The indirect method is based on the works of Panneton and Olny [34, 35], which provided inverse formula to assess the transport parameters from the knowledge of dynamic thermal $\tilde{K}$ and viscous $\tilde{\rho}$ behaviour. These two dynamic quantities can be experimentally estimated from acoustical measurements with three- [49]/four-microphones [50] techniques based on wave decomposition in impedance tube [42, 51]. A synthesis of calculation of these techniques is reported in Sec. 5. Other thermoacoustic methodologies to assess the dynamic visco-thermal behaviour of porous material are the lumped element techniques proposed by Di Giulio *et al.* (for $\tilde{\rho}$) [52] and Napolitano *et al.* (for $\tilde{K}$) [53]. These latter methods are particularly advices for low frequency measurements. The porosity can be estimated both from low and high frequency limit of dynamic bulk modulus as follow

$$\lim_{\omega \to 0} \tilde{K} = \frac{p_m}{\varphi}, \tag{3.32}$$

$$\lim_{\omega \to +\infty} \tilde{K} = \frac{\gamma p_m}{\varphi}. \tag{3.33}$$

At the same time, airflow resistivity can be obtained in the limit of low frequency of the imaginary part of dynamic density

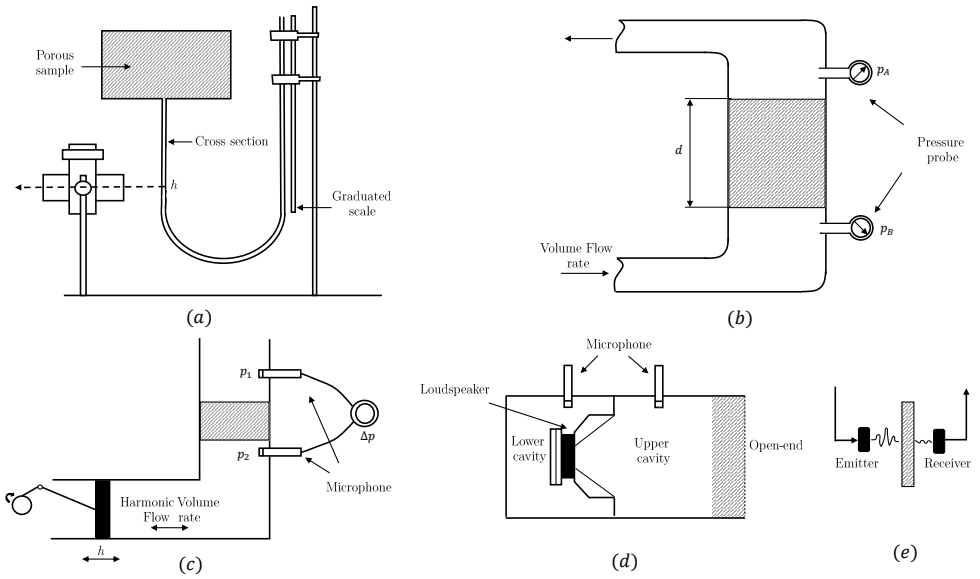

Figure 3.3: Schematic representation of: (a) Beranek's measurement system for porosity, (b) Airflow resistivity standard measurement from ISO 9053-1, (c) Alternating airflow method for measuring airflow resistance, ISO 9053-2, (d) Acoustical measurement of airflow resistivity (Dragonetti *et al.* set up, (e) Ultrasonic set up measurement for characteristic lengths and tortuosity.

$$\sigma = -\frac{1}{\varphi} \lim_{f \to 0} \Im\left(\omega \tilde{\rho}\right). \tag{3.34}$$

Known these parameters, the others four are obtained from the provided analytical solutions

$$\alpha_\infty = \frac{1}{\rho_m} \left(\Re\left(\tilde{\rho}\right) - \sqrt{\Im\left(\tilde{\rho}\right)^2 - \left(\frac{\sigma\varphi}{\omega}\right)^2} \right), \tag{3.35a}$$

$$\Lambda = \alpha_\infty \sqrt{\frac{2\rho_m \mu}{\omega \Im\left(\tilde{\rho}\right)\left(\rho_m \alpha_\infty - \Re\left(\tilde{\rho}\right)\right)}}, \tag{3.35b}$$

$$\Lambda' = \sqrt{2}\delta_\kappa \left[-\Im\left(\frac{\gamma p_m - \varphi \tilde{K}}{\gamma p_m - \varphi\gamma \tilde{K}} \right)^2 \right]^{-\frac{1}{2}}, \tag{3.35c}$$

$$k'_0 = \frac{\varphi \delta_\kappa^2}{2} \left[-\Re\left(\frac{\gamma p_m - \varphi \tilde{K}}{\gamma p_m - \varphi\gamma \tilde{K}} \right)^2 \right]^{-\frac{1}{2}}. \tag{3.35d}$$

Eqs. (3.35a)-(3.35d) are not obtained from asymptotic behaviour and they are valid in whole frequency range. Of course, the estimations of all the parameters are affected by uncertainties related to the impedance tube measurements [54, 55, 56, 57]. In particular, as it can be seen the accuracy of the estimation of φ and σ influence the assessment of the other four parameters.

3.5.3 Inverse methods

Inverse methods are essentially based on the minimization of cost function $C\left(\theta\right)$ in $\mathbb{R}^n$ space, where θ is the set of n parameters to be optimized, between experimental data and theoretical

model. The direct measures of these parameters are tedious and provide a less accuracy to respect to the porosity and airflow resistivity measurements. The inverse characterization of porous media based on acoustical measurement has been carried out for different model and parameters. Atalla and Panneton [58] firstly introduced this technique to assess the values of high frequency parameters $\theta = \left(\alpha_\infty, \Lambda, \Lambda'\right)$. Taking as reference the surface impedance $\tilde{Z}_s = -i\tilde{Z}_c \cot\left(\tilde{k}d\right)$, with d the sample thickness, carried out from experiments, cost function is defined as follow by [58]

$$C\left(\theta\right) = \frac{1}{2}\sum_{i=1}^{N} |\tilde{Z}_{s_i,\text{model}}\left(\theta\right) - \tilde{Z}_{s_i,\text{experimental}}|^2, \tag{3.36}$$

where N is the total number of computed frequencies in the range of interest. Solution of the mathematical problem is found for $\theta^* = \left(\alpha_\infty^*, \Lambda^*, \Lambda'^*\right)$ for which $C\left(\theta^*\right) = \min\left[C\left(\theta\right)\right]$. Of course, upper and lower boundary constrains to values must be set to avoid local minima of $C\left(\theta^*\right)$ with no physical meaning. Further studies have been conducted to improve the inverse characterization methodology. Dragonetti *et al.* [59] highlighted the complex values of $\tilde{Z}_s$ and proposed to find the minima of cost function in vector form dividing real and imaginary part

$$C\left(\theta^*\right) = \min\left\{\frac{1}{2}\sum_{i=1}^{N}\begin{bmatrix}\Re\left(\tilde{Z}_{s_i,\text{model}}\left(\theta\right)\right)\\ \Im\left(\tilde{Z}_{s_i,\text{model}}\left(\theta\right)\right)\end{bmatrix} - \begin{bmatrix}\Re\left(\tilde{Z}_{s_i,\text{experimental}}\right)\\ \Im\left(\tilde{Z}_{s_i,\text{experimental}}\right)\end{bmatrix}\right\}. \tag{3.37}$$

3.6 Numerical approaches

Numerical calculation of transport parameters is based on three uncoupled-steady problems:
• the Stokes flow problem, where viscous forces dominate over the inertial ones ($\omega \ll \omega_\nu$) and static viscous permeability k_0 can be estimated;
• the Laplace's problem, where high frequency limit ($\omega \gg \omega_\nu$) allows to consider the fluid inviscid and to calculate tortuosity α_∞ and characteristic lengths Λ;
• the Poisson's problem, which replaces the diffusion-controlled problem to assess static thermal permeability $k_0{}'$.
Each problem is defined in a Representative Elementary Volume (REV) of the material, or which is the same in a Periodic Unit Cell constituting the porous media. An example with the constitutive surfaces for the boundary conditions is reported in Fig. 3.4. The presented approach to assess transport parameters is generally called *Hybrid Multiscale* (HM) [84–94], while to achieve a complete dynamic description of the behaviour of material *Direct Multiscale* (DM) or *Direct Numerical Simulation* (DNS) approaches can be applied. An exhaustive synthesis of the computational approaches for modelling dynamic visco-thermal behaviour of porous material is reported in the benchmark of Zienlinski *et al.* [60].

3.6.1 Viscous flow

In the low Reynolds number, Stokes equation governs the behaviour of an incompressible Newtonian fluid

$$\mu\nabla^2 v - \nabla p = -G \quad \text{on} \quad V_f, \tag{3.38}$$

where the applied boundary conditions are

$$\nabla \cdot v = 0 \quad \text{in} \quad V_f, \tag{3.39a}$$
$$v = 0 \quad \text{on} \quad \Omega_{fs}, \tag{3.39b}$$
$$v \cdot n = 0 \quad \text{on} \quad \Omega_{\text{lateral}}, \tag{3.39c}$$
$$p = p_{up} \quad \text{on} \quad \Omega_{up}, \tag{3.39d}$$
$$p = p_{dw} \quad \text{on} \quad \Omega_{dw}. \tag{3.39e}$$
$$\tag{3.39f}$$

p_{up} and p_{dw} are the pressure conditions on the top Ω_{up} and bottom Ω_{dw} faces of the unit cell, respectively. Therefore, a macroscopic pressure gradient $\left(G = \nabla p / L = p_{dw} - p_{up}\right)$ is applied, with L the dimension of the cell in the direction of wave propagation. v is the velocity of fluid and no-slip boundary condition and periodicity are respectively applied to fluid-solid interface $\left(\Omega_{fs}\right)$ and lateral boundaries $\left(\Omega_{f,\text{lateral}}\right)$. The static viscous permeability can be evaluated from the averaged velocity over the fluid volume

$$k_0 = \mu \frac{\langle v \rangle \cdot e}{G}, \tag{3.40}$$

where e is the unit vector of the direction of wave propagation, and angular brackets indicate the average over the fluid volume.

3.6.2 Inertial flow

In high frequency range, viscous boundary layer becomes negligible, and the fluid behaves as an inviscid perfect one. According to the works of Johnson *et al.* [26], Brown [61] and Avellaneda and Torquato [33], this problem is equivalent to the problem of electric conduction, where the conducting fluid fills the porous media having a constant conductivity. Laplace's problem can be written as

$$\nabla^2 \phi = 0 \quad \text{in} \quad V_f, \tag{3.41}$$

where the boundary conditions are

$$E = -\nabla \phi \quad \text{in} \quad V_f, \tag{3.42a}$$
$$E \cdot n = 0 \quad \text{on} \quad \Omega_{fs} \quad \text{and} \quad \Omega_{\text{lateral}}, \tag{3.42b}$$
$$\phi_{dw} = -p_{up} = -\Delta V/2 \quad \text{on} \quad \Omega_{up} \quad \text{and} \quad \Omega_{dw}. \tag{3.42c}$$

E and ϕ are respectively the local electric fields and the electric potential. Therefore, the high frequency of tortuosity and the viscous characteristic length can be evaluated as

$$\alpha_\infty = \frac{\langle E \cdot E \rangle_{V_f}}{\langle E \rangle_{V_f} \cdot \langle E \rangle_{V_f}}, \tag{3.43}$$

$$\Lambda = 2 \frac{\int_{V_f} E \cdot E \, \mathrm{d}V}{\int_{\Omega_{fs}} E \cdot E \, \mathrm{d}\Omega}. \tag{3.44}$$

3.6.3 Thermal problem

Eq. (3.27) pointed out by Lafarge [28] links the acoustic fluctuations of temperature to the time derivative of acoustic pressure. The static thermal permeability is useful to describe these thermal

effects in the fluid saturating a solid skeleton, which can be considered as a thermostat. Furthermore, the Poisson's problem becomes

$$\nabla^2 \tau = -1 \quad \text{in} \quad V_f, \tag{3.45}$$

where boundary conditions on τ are

$$\tau = 0 \quad \text{on} \quad \Omega_{fs}, \tag{3.46a}$$
$$\nabla\tau \cdot n = 0 \quad \text{on} \quad \Omega_{\text{lateral}}, \quad \Omega_{up} \quad \text{and} \quad \Omega_{dw}. \tag{3.46b}$$

Therefore, static thermal permeability is estimated as

$$k_0{}' = \varphi\langle\tau\rangle. \tag{3.47}$$

Porosity and thermal characteristic length are purely geometrical transport parameters not related to a specific physical field. Therefore, their values can be assessed only by using their definition, Eqs. (3.20) and (3.24), from the CAD geometry of the unit cell. An example of the three fields (viscous flow, electric potential and thermal flux) inside a Representative Volume of a porous material (here, tetragonal pin array) is shown in Fig. 3.5.

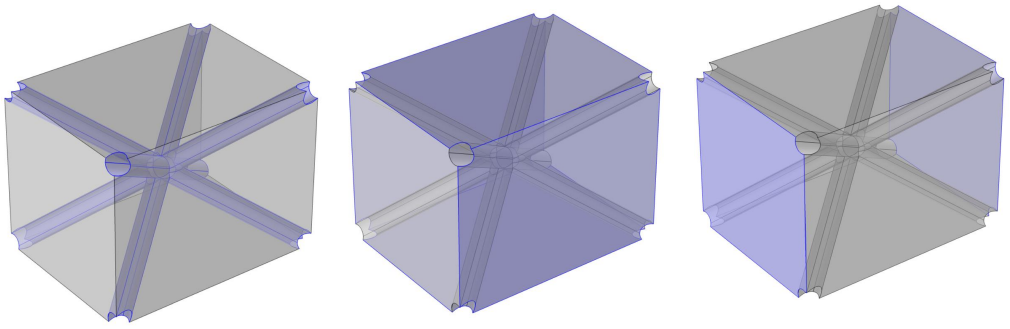

(a) (b) (c)

Figure 3.4: Surface for the boundary conditions: (a) fluid-solid interface Ω_{fs}, (b) lateral surface $\Omega_{lateral}$, (c) Ω_{up} and Ω_{down}.

3.6.4 Consistency of the parameters

Transport parameters are independent one from an another from their definitions, but the geometry of the solid skeleton imposes some constrains in the range of values they can assume. As it is shown in the work of Johnson *et al.* [26], the viscous characteristic length is always lower than the thermal one

$$\Lambda \leq \Lambda'. \tag{3.48}$$

At the same time, Avellaneda and Torquato [33] demonstrated the inequality between the static thermal and viscous permeability for all micro-geometries

$$k_0 \leq k_0{}'. \tag{3.49}$$

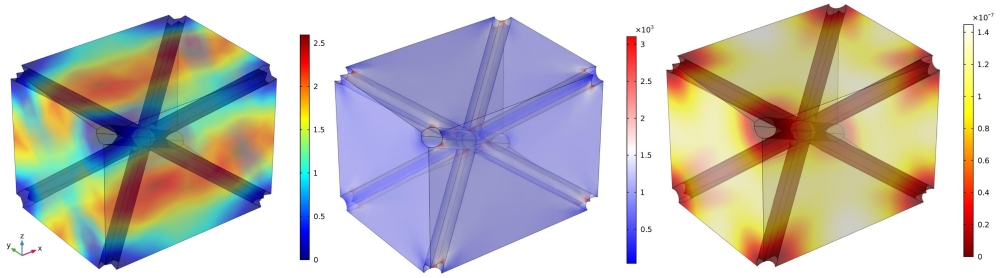

(a) (b) (c)

Figure 3.5: Fields of (a) the velocity v under an unitary differential pressure stimulus $\Delta p = 1$, (b) electric potential E under an unitary differential voltage stimulus $\Delta V = 1$, and (c) scaled temperature τ, for *Hybrid Multiscale* calculations of the tetragonal pin array.

Furthermore, for different typologies of material the tortuosity follows the Archie's empirical law [62]

$$\alpha_\infty = \left(\frac{1}{\varphi}\right)^r \tag{3.50}$$

where r is a coefficient depending on the material. Another check can be done on the values of viscous and thermal pore shape factor M and M' which are of the order of magnitude around the unit for classical porous material for acoustic applications. For example, in case of uniform cross section materials, mathematical description of viscous and thermal problems has the same form [14]. Therefore, it results that

$$\tilde{k}_\nu(\omega) = \tilde{k}'(P_r\omega), \tag{3.51a}$$
$$M = M' = 1, \tag{3.51b}$$
$$k_0 = k_0{}', \tag{3.51c}$$
$$\Lambda = \Lambda', \tag{3.51d}$$
$$\alpha_\infty = 1. \tag{3.51e}$$

In Fig. 3.6, dimensionless viscous and thermal permeabilities are reported in the case of uniform cross-sectional materials. As it can be seen, thermal and viscous problems are represented in the same form.

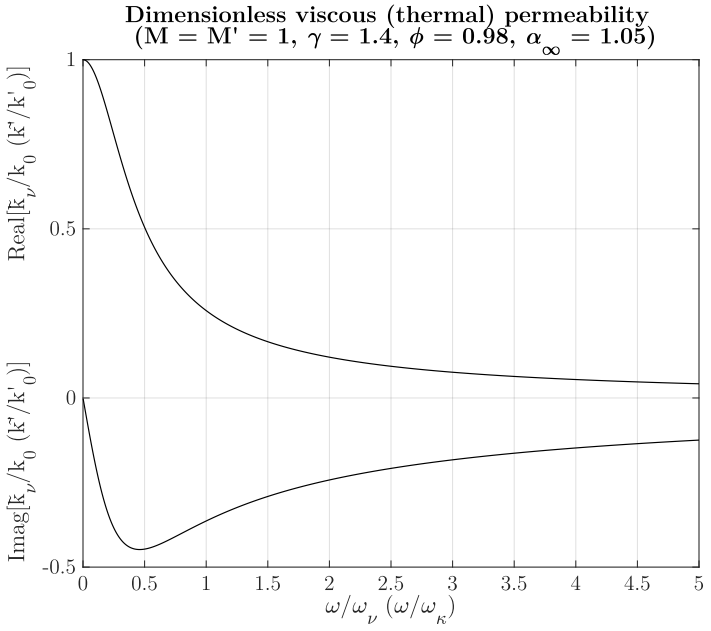

Figure 3.6: Dimensionless viscous (thermal) permeability for uniform cross-sectional materials. It can be noted that scaled velocity and temperature fields have the same mathematical description.

Chapter 4

New transport parameters models for unconventional thermoacoustic stacks

Contents

4.1 Introduction

To assess the dynamic behaviour of a porous material undergoing a sound wave excitation, its own transport parameters are required. The modern additive manufacturing (AM) technologies allow to realize innovative and multi-functional materials for different applications. In particular, AM techniques make possible to design a material with a precise-controlled micro-geometry. Therefore, from the spatial repetition of a chosen unit cell, an entire sample can be realized. This allow to investigate on the properties of the unit cell to design the overall material, and then to select the geometry suitable designed for a specific application. In recent years various AM technologies have already been used in the research and development of a variety of new acoustic materials, such as acoustic absorbers with passive destructive interference [63], hollow-sphere foams [64], 3D-printed fibrous materials [65], sound-absorbing micro-lattices [66]. Therefore, the possibility to have sets of correlations between micro-geometry and transport parameters helps in the design of a porous material with specified acoustic properties. The aim of this work is to realize thermoacoustic stacks by means of additive manufacturing, once the unit cell able to maximize the thermoacoustic energy conversion is found through the following developed models. In this section the transport parameters models are reported for three different typology of material: Tetragonal Pin Array [67], Wire Mesh [68] and 3D-Membrane Foams.

4.2 Tetragonal pin array

The lattice can be imagined as an arrangement of intersecting struts constituting the diagonals of a tetragon with a square base. According to the height or the size of the base of the tetragon, the struts can have different orientations with respect to the direction of the sound waves propagation. This study is motivated by the remarkable thermoacoustic potentialities of that material, and very similar type of lattices, shown in previous studies [69, 70, 71]. Parallel pin-array porous materials, shown in Fig. 4.1.a, also called pin-array stacks in case of thermoacoustic applications, are studied by Swift and Keolian [70] where the authors noted an increase in efficiency compared to other traditional stacks (circular pores and parallel plates). The enhanced thermoacoustic performance expected for cores with cylindrical elements is related to the fact that, for working fluids with Prandtl number $P_r < 1$, the convexity of the solid surface results in a greater ratio of thermoacoustic area to viscous area compared to other stacks provided with inner concave geometries. Swift pointed out that a practical realization of the pin-array stack geometry is a significant engineering challenge, and for this reason, he made it of a simple "large-scale" model (pin diameter $3.18mm$) and applied the principle of similitude. Thanks to the advent of additive manufacturing, it seems that the engineering challenge has been somewhat won and, apart from the relative difficulties related to times and costs of implementation, preliminary results on stainless steel pin-array elements confirm what Swift theoretically proved. Even more interestingly, the additive manufacturing allows the creation of ordered structures of struts with different orientation and not only "pins" parallel to the direction of flow, as studied by Swift or orthogonal to the direction of sound propagation (Fig. 4.1.b, as proposed by Matveev [72]). Lattices based on Tetragonal Body Centered (TBC) cells allow different orientation of the struts according to the desired height of the cell itself, reported in Fig. 4.1.c [67]. Moreover, the additive manufactured structures can be precisely controlled and realized by using different constituting materials.

Numerical simulations

In Fig. 4.2.a an entire view of a porous sample based on TBC unit cell (Fig. 4.2.b) is reported. Different TBC cells can be simulated by varying the main geometrical dimensions L_x, L_y, L_z and

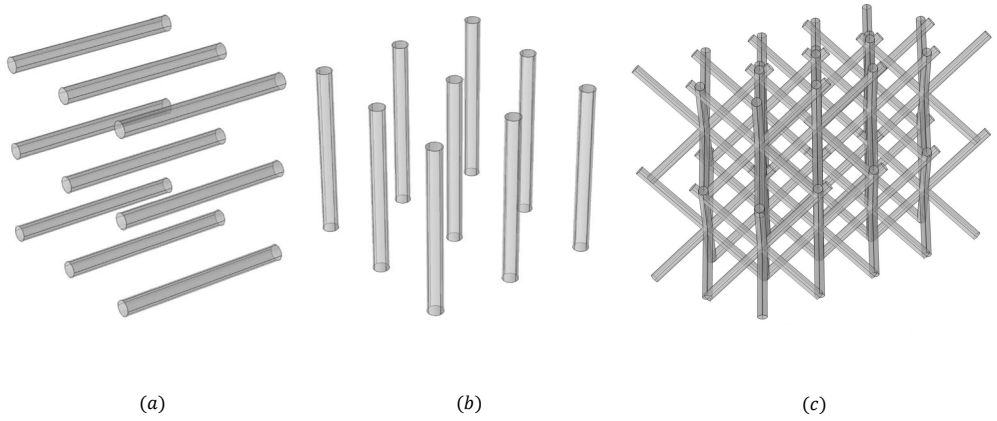

(a) (b) (c)

Figure 4.1: (a) Longitudinal pin array, (b) transversal pin array, (c) tetragonal pin array.

pin radii r_p. In that case, *Direct Numerical Simulation* approach has been used. Therefore, the linearized Navier-Stokes equations, Eqs (2.9), (2.10) and (2.11), in frequency domain are solved for a single unit cell in order to solve thermo-fluid dynamic fields inside the fluid volume. A pressure gradient Δp in the direction of wave propagation, symmetry on lateral boundaries $(v_1 \cdot n = 0)$ and no-slip isothermal wall $(v_1 = 0, T_1 = 0)$ at fluid-structure interface are applied as boundary conditions. Thermoviscous functions can be assessed by reversing Eqs. (2.14) and (2.15), once from the numerical results pressure, temperature, and velocity averaged fields over the fluid domain are known [73]

$$f_\nu = 1 - \frac{\langle v_1 \rangle}{u_{inv}}, \tag{4.1}$$

$$f_\kappa = 1 - \frac{\langle T_1 \rangle}{T_a}, \tag{4.2}$$

where $u_{inv} = \frac{i}{\omega \rho_m} \frac{\Delta p}{L_z}$ is defined as the inviscid velocity and $T_a = \frac{\langle p_1 \rangle}{\rho_m c_p}$ as the adiabatic temperature. Subsequently, from Eqs. (2.19) and (2.20), the complex density $\tilde{\rho}$ and the complex bulk modulus $\tilde{K}$ can be evaluated. Based on the Π-theorem, each dimensionless transport parameters can be expressed as function of two dimensionless quantities $\bar{L}_x = L_x/r_p, \bar{L}_z = L_z/r_p$. As consequence, an algorithm realized in MATLAB is used to perform a parametric optimization procedure where the transport parameters of the JCAL semi-phenomenological model, are extracted from the knowledge of complex density $\tilde{\rho}$ and bulk modulus $\tilde{K}$ provided by the FEM simulations performed on 324 different lattice cells, which are obtained by varying $\bar{L}_x, \bar{L}_z$ in a range of values from 8 to 25 and by fixing $r_p = 9e - 5m$. The procedure is based on Ordinary Least Squares method, described in Ref. [59]. Once the parameters have been obtained for each cell of the large set of cells simulated with FEM, a fitting procedure has been implemented to find out the coefficients of the second order polynomials for each parameter (adjusted R-square equal to 0.99 in each case)

$$\left[\varphi, \frac{\Lambda'}{r_p}, \frac{\Lambda}{r_p}, \alpha_\infty, \frac{k_0}{r_p^2}, \frac{{k_0}'}{r_p^2}\right] = A_1 + A_2\bar{L}_x + A_3\bar{L}_z + A_4\bar{L}_x^2 + A_5\bar{L}_x\bar{L}_z + A_6\bar{L}_z^2, \tag{4.3}$$

where the constant $A_{i=1-6}$ are reported in Tab 4.1.

Dimensionless parameter	A_1	A_2	A_3	A_4	A_5	A_6
φ	0.4787	0.03023	0.01335	-0.0006	-0.0001627	-0.0002149
Λ'/r_p	-0.9985	0.1024	0.08976	-0.001162	0.04551	-0.01226
Λ/r_p	0.3271	0.1772	-0.1711	2.728e-5	0.01215	0.005476
α_∞	1.373	-0.02005	-0.01669	0.0003822	0.0002203	0.0002946
k_0/r_p^2	1.31	-0.1572	-0.2395	0.02229	0.004712	0.007991
$k_0{}'/r_p^2$	2.804	-0.5023	-0.2478	0.01621	0.05014	-0.003899

Table 4.1: Constants $A_1 - A_6$ of TBC cell model for the evaluation of dimensionless transport parameters

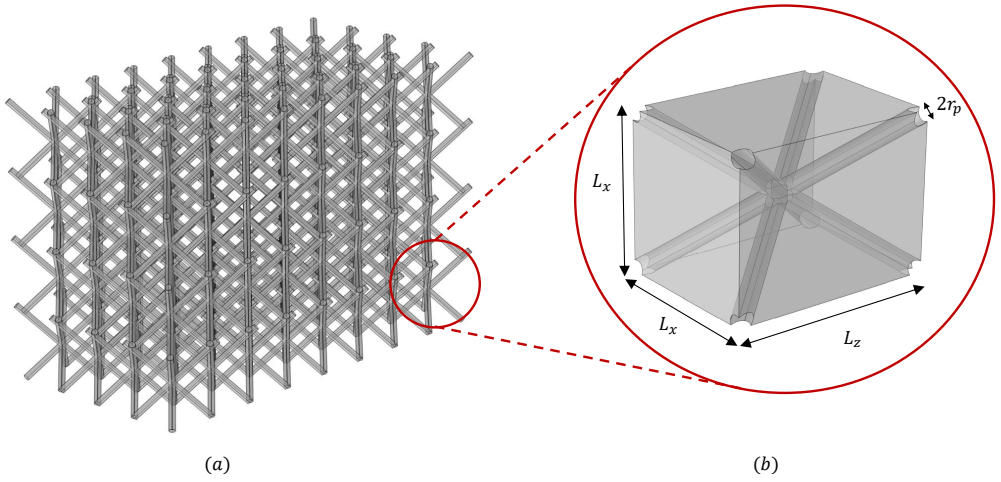

Figure 4.2: Tetragonal pin array: (a) the stack, (b) the unit cell.

4.3 Wire mesh

Wire meshes (or stacked screen bed), reported in Fig. 4.3, are largely used, because they are easy to realize with respect to other classical uniform cross-sectional stacks (parallel plates, circular pores and pin array); and they offer a low ratio between the fluid volume and the fluid-solid interface area which makes them suitable for travelling wave devices [3, 74, 75]. There is, however, a lack of an accurate model in the literature to describe the viscous and thermal properties of this kind of stacks. The performance predictions of these stacks are usually determined from semi-empirical correlations provided by Swift and Ward [76]. They are, however, restricted to a specific geometrical configuration in their current form, which limits their ability to study how thermoacoustic efficiency relates to the geometrical details of the wire mesh stack. Swift and Ward [76] proposed a description of the dynamic viscous and thermal-relaxation effects of these materials from the friction factor and heat transfer data of Kays and London [77], derived from a steady-state assumption

$$\frac{dp_1}{dx} = -i\omega\rho_m \left[1 + \frac{(1-\varphi)^2}{2\,(2\varphi - 1)}\right] \langle v_1 \rangle - \frac{\mu}{r_h^2}\left[\frac{c_1}{8} + \frac{c_2 R_{e,1}}{3\pi}\right] \langle v_1 \rangle, \tag{4.4}$$

$$\frac{d\langle v_1\rangle}{dx} = -\frac{i\omega}{\gamma p_m} p_1 + \frac{1}{T_m}\frac{dT_m}{dx}\langle v_1\rangle + \\ + \frac{i\omega}{T_m}\left[\frac{1}{\rho_m c_p}\frac{\left(g_c + e^{2i\theta_p} g_\nu\right)\varepsilon_h}{1+\varepsilon_h\left(g_c + e^{2i\theta_T} g_\nu\right)} p_1 - \frac{1}{i\omega}\frac{\left(g_c - g_\nu\right)\varepsilon_h}{1+\varepsilon_h\left(g_c + e^{2i\theta_T} g_\nu\right)}\langle v_1\rangle\right]. \tag{4.5}$$

Here, $r_h = 2A/p_{wet}$ is the hydraulic radius defined as the ratio between the cross-sectional area A and the wet perimeter p_{wet}, $R_{e,1} = 4|\langle v_1\rangle| r_h \rho_m/\mu$ is the complex Reynolds-number amplitude, θ_p and θ_T are respectively the phase angle between the oscillating velocity and pressure and oscillating velocity and temperature. $c_1(\varphi)$, $c_2(\varphi)$ and $\varepsilon_h(\varphi)$ are polynomial correlations expressed as functions of porosity, while g_c and g_ν can be assessed from trigonometric integrals. More details are reported in [78]. All these elements make heavy and tedious the general description of the visco-thermal behavior of such materials. Therefore, it would be desirable to extend the simple use of thermoviscous functions, f_ν and f_κ, to a convenient analytical formulation, as available for other canonical geometries (parallel plates, circular pores, pin arrays). Because f_ν and f_κ are intrinsic properties of the materials; the possibility to characterize the thermo-viscous functions for the wire mesh would allow making preliminary considerations on the behavior of these materials and then on their thermo-acoustic efficiency without simulating the entire device.

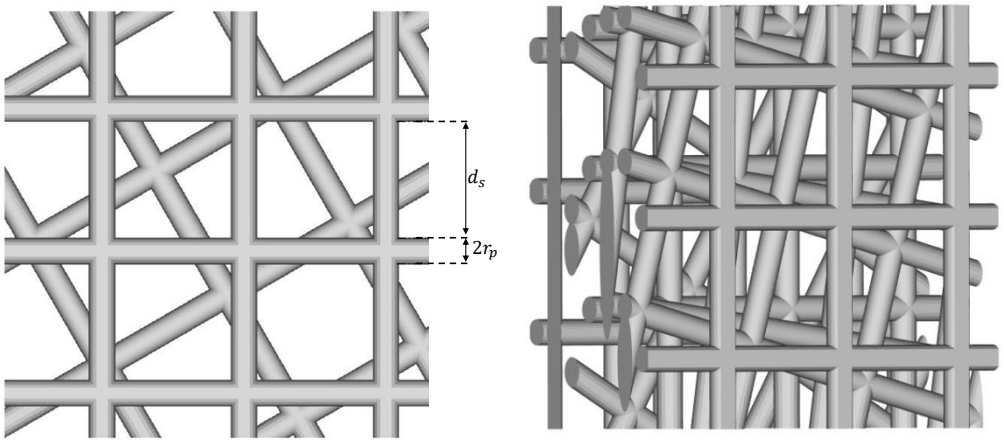

Figure 4.3: (a) Schematic representation of the wire mesh stack and its geometrical descriptors. (b) An illustrative example of wire mesh stack representative volume element. For the sake of clarity, only the solid skeleton of the wire mesh stack of through-thickness Dt is displayed.

Numerical simulations

The homogenization theory [12] highlights that when a scale separation exists, viscous and thermal effects can be decoupled. In particular, thanks to the JCAL model, the knowledge of the dynamic complex behaviour of the material is a function of only six non-acoustical parameters, which can be assessed from three boundary value problems, as reported in Subsec. 3.6. Wire meshes are practically obtained through superposition of several layers of grid, placed in a random way. It was

observed, from the numerical procedure reported throughout Appendix A, that the relative error of both the viscous and thermal permeability computations between two subsequent calculations corresponding to the number n of grid layers, was typically less than 5%, for $n = 6$. The maximum relative differences for the other transport parameters were less than 1%. The Representative Volume Element (RVE) was therefore considered in this study to be composed of six superimposed grid layers (Fig. 4.3.b). Lateral dimensions were imposed to be twice those of the thickness. Under these circumstances, it was observed that the lateral dimensions have no influence on the results when increasing their size. Simulations were carried out on 150 different unit-cells obtained by varying the strut radius r_p from 0.13 to 0.78 mm, and the distance between struts d_s from 1 to 3.5 mm. Note that this range of variations of r_p and d_s parameters encompasses the typical dimensions of commercial wire screens [79, 74]. It is also noteworthy that the geometry of wire mesh is characterized by intertwined metal filaments, while we constructed a simplified model of the wire mesh. The junction at two connected filaments was represented as a straight intersection. This model was found to be accurate enough for the prediction of the transport parameters of wire mesh stacks (Appendix A). Through Eqs. (3.20), (3.24), (3.40), (3.43), (3.44), (3.47), transport parameters were evaluated for each unit-cell. Subsequently, the general structure of the proposed correlations between geometrical descriptors and transport parameters was inspired from the ones provided by Luu *et al.* [80]. This was possible because of the similarity between wire mesh and fibrous structure. The proposed correlations are summarized in Tab. 4.2, together with some statistical indicators assessing the goodness-of-fit.

Correlation	R-Squared	SSE
$\varphi = 1 - 0.7099\frac{\pi r_p}{d_s+2r_p}$	0.9806	0.0493
$\Lambda'/r_p = \frac{\varphi}{1-\varphi-0.005133}$	0.9845	10.38
$\Lambda/r_p = 0.4825\frac{\varphi}{1-\varphi+0.04564}$	0.9802	1.284
$\alpha_\infty = \left(\frac{1}{\varphi}\right)^{0.5807}$	0.9657	0.1303
$\log_{10}\left(k_0/r_p^2\right) = 0.7765\log_{10}\left[\frac{\varphi^3}{(1-\varphi)^2}\right] - 0.9855$	0.9993	0.0605
$\log_{10}\left(k_0{}'/r_p^2\right) = 0.7258\log_{10}\left[\frac{\varphi^3}{(1-\varphi+0.3054)^2}\right] - 0.6741$	0.9992	0.1802

Table 4.2: Transport parameters' correlations for wire mesh stacks. R-squared is the coefficient of determination, while SSE denotes the sum squared errors of residuals.

4.4 3D-printed membrane foams

Foams is a dispersion of gas in a liquid or solid matrix. Its structure consists of membranes, ligaments (intersection of three membranes), and vertices (intersection of four ligaments) (Fig. 4.4). Whereas closed membranes are necessary to ensure the mechanical stability of liquid foam, they can be open in solid foam, allowing for the foam cells (pores) to be connected through windows [81, 82, 83]. Solid foams find applications in many fields, such as mechanical dampers, thermal, or/and acoustic insulation heat exchangers. As shown in Fig. 4.4, a typical PU foam microstructure can be seen as a collection of interlinked struts forming 3D structures as a packing of tetrakaidecahedra cells. Each cell is connected to others through pores. Materials with 100 % open pores are called "fully reticulated." In this case the interconnectivity between cells is maximal. If some of the pores are closed or partially closed by thin membranes, the material is called "partially reticu-

lated". Solid films or membranes in real porous media such as polyurethane or metallic foams only account for a very small fraction of material in the overall mass of the porous media. Yet, their role might be of primary importance in the understanding of transport and acoustical properties of these foams. As a long wavelength wave propagates, the viscoinertial and thermal interactions between the disordered interconnected pores and the surrounding air pose a fundamental physical challenge in the microstructural identification of features, which are characteristic of the overall transport phenomena. Realistic foam microstructures usually exhibit a distribution of pore size are widely used to simulate Polydisperse foams are simulated through the Random Laguerre tessellations, constructed by using a random dense packing of hard spheres with a distribution of sphere size that coincides with the pore size distribution (estimated from the characterized foam samples). The aim of this model is to predict the dynamic properties of membrane foams realized with additive manufacturing technique. This means that ordered monodisperse geometry are considered, refereed as 3D Membrane Foams. The main differences between the chosen unit cell and the classical reticulated tetrakaidecahedra cell are the absence of ligaments to link the membrane, and the no-negligible thickness of the membranes, as shown in Fig. 4.5.a. Therefore, the three geometrical descriptors which characterize the unit cell are the dimension of the unit cell D_t, the membrane thickness ξ and the membrane opening ratio defined as $t_0 = \sqrt{A_{open}/A_{membrane}}$ (ratio between the light green and red area in Fig.4.5.a).

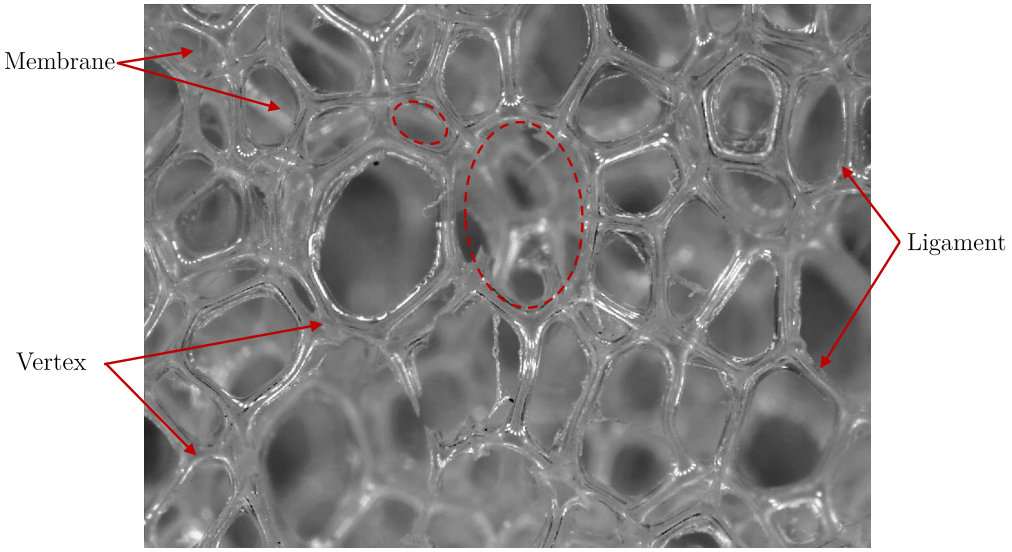

Figure 4.4: Solid polymeric foam for packaging under the optical microscope revealing the open-cell microstructure and showing vertex, ligaments, membranes and windows apertures (dashed lines). Photo source: *Wikimedia*.

Numerical simulations

As for the Wire Meshes, numerical simulations are carried out on the unit cell to assess the transport parameters through the scale separation hypothesis by using Stokes, Laplace and Poisson problems (Fig. 4.5.b). Taking advantage of the symmetry of the unit cell, only its one-eighth part is taken into account as fluid domain to reduce the computational costs. The limit range of the geometrical parameters are expressed through two dimensionless quantities as $0.2 < t_0 < 0.7$ and $0.003 < \xi/D_t < 0.2$. Furthermore, a numerical trick is adopted to help the convergence of transport parameters values. In fact, rounded edges of membrane are adopted to avoid singularity

points in the numerical grid. In Appendix B, it can be seen the convergence trend of the rounded versus non-rounded edges simulations. The structure of the correlations for the porosity φ and thermal characteristic length Λ' as functions of geometrical descriptors are derived analytically, while for inertial parameters Λ and α_∞ correlations are inspired from Doutres *et al.* [84] and for static viscous permeability from Langlois *et al.* [85]. The proposed correlation are reported in Tab. 4.3.

Correlation	R-Squared	SSE
$\varphi = 1 - \frac{9}{16}\left(1+2\sqrt{3}\right)\left(1-t_0^2\right)\frac{\xi}{D_t}$	0.9875	0.01649
$\Lambda'/D_t = \frac{2\varphi}{6\left(1-t_0^2\right)+\frac{\xi}{D_t}}$	0.9534	0.03528
$\Lambda'/\Lambda = \varphi^{0.2468}\left(\frac{1}{t_0}\right)^{0.9609}$	0.9556	3.254
$\alpha_\infty = 0.6668\left(\varphi\right)^{-0.4703}\left(\frac{1}{t_0}\right)^{0.9678}$	0.9641	1.984
$k_0/D_t^2 = 0.03249\varphi t_0^3$	0.9974	2.334e-6
$k_0{}'/D_t^2 = 0.04023\varphi^{3.265}t_0^{2.494} + 0.01097\left(\frac{\xi}{D_t}\right)^{-0.07873}$	0.9971	8.569e-7

Table 4.3: Transport parameters' correlations for 3D-printed membrane foams. R-squared is the coefficient of determination, while SSE denotes the sum squared errors of residuals.

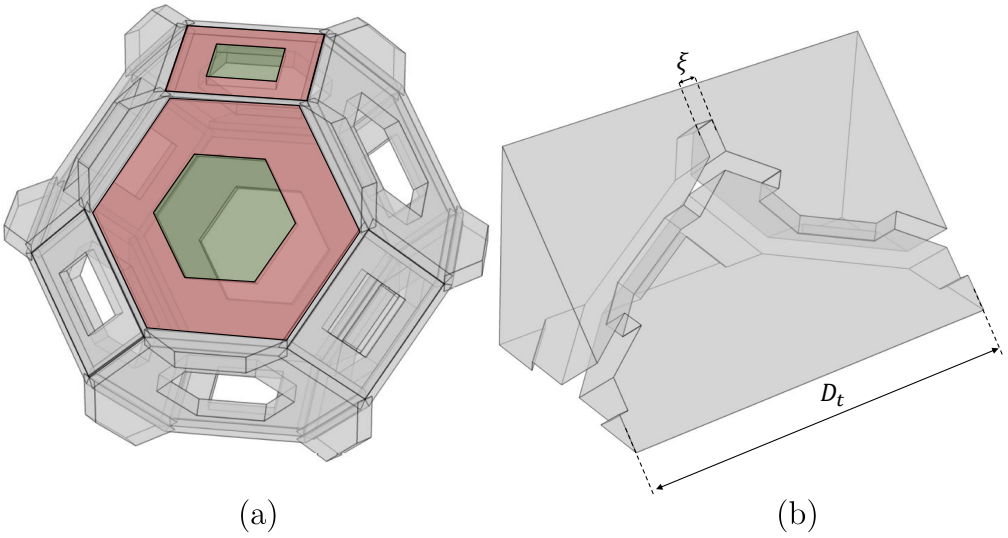

Figure 4.5: (a) The unitary solid skeleton of the 3D-membrane foam, (b) one-eighth part of the fluid volume unit cell adopted in the numerical simulations.

4.5 Thermal behaviour of the solid skeleton

As highlighted in Subsec. 2.6.4, to complete the thermoacoustic description of a porous material, the heat capacity ratio ε_s parameter is needed in order to take into account the imperfect isothermal condition provided by the solid matrix. The heat capacity ratio ε_s allows to express how far the

solid skeleton is from an isothermal condition [22]. This parameter turns out to be equal to zero for a perfect isothermal solid condition and tends towards infinity in the case of an adiabatic condition. ε_s can be assessed in an operative way by means of Eq. (2.53)

$$\epsilon_s = \frac{\rho_m c_p}{\rho_s c_s} \frac{f_\kappa}{f_s} \frac{\varphi}{1-\varphi}.$$

f_s is the dynamic thermal function (a solid dynamic thermal function understood as an analogue to f_κ for the fluid part) depending on the geometry of the solid structure and the *solid thermal penetration depth* $\delta_s = \sqrt{2\kappa_s/(\rho_s c_s \omega)}$. Therefore considering the above mentioned models, the dynamic thermal function f_s is the only missing parameter to assess the heat capacity ratio ε_s of Tetragonal Pin Array, Wire Mesh and 3D-printed membrane foams, and fulfil the overall thermoacoustic description of these stacks. In the cases of Tetragonal Pin Array and Wire Mesh, the solid structure geometry can be considered as an array of circular rods, for which an analytical formulation of the solid thermal function exists,

$$f_s = \frac{2J_1\left[(i-1)\, r_p/\delta_s\right]}{2J_0\left[(i-1)\, r_p/\delta_s\right](i-1)\, r_p/\delta_s}. \tag{4.6}$$

In the case of 3D-printed membrane foams, the geometry of the solid skeleton has a more complex shape which do not allow to use any analytical formula for f_s. Therefore, the idea is to adapt the Champoux-Allard-Lafarge model coupled with Dragonetti *et al.* relationship between $\tilde{K}$ and f_κ to characterize the dynamic thermal behaviour of solid skeleton. By combining Eqs. (3.10) and (2.20), it follows

$$f_s = 1 - \left[1 + \frac{\varphi_s k_s}{i k'_{0s} c_s \omega \rho_s} \sqrt{1 + i \frac{4 {k'_{0s}}^2 c_s \rho_s \omega}{k_s {\Lambda'_s}^2 \varphi_s^2}}\right]^{-1}, \tag{4.7}$$

where subscript s indicates the solid matrix properties. In Eq. (4.7), three novel transport parameters are introduced:

• the *solid porosity*, which is complementary to the classical porosity defined for the fluid part,

$$\varphi_s = 1 - \varphi. \tag{4.8}$$

• the *solid thermal characteristic length* defined as, in analogy with Eq. (3.24),

$$\Lambda'_s = 2\frac{\int_{V_s} dV}{\int_\Omega d\Omega} = \Lambda' \frac{1-\varphi}{\varphi} = \Lambda' \frac{\varphi_s}{\varphi}. \tag{4.9}$$

• the *solid static thermal permeability*, which has the same geometrical meaning of k'_0 but refereed to a volume corresponding to the solid fraction. Therefore, φ_s and Λ'_s are expressed as function of the transport parameters φ and Λ', for which the correlation are reported in Tab. 4.3. With respect to the first two solid thermal transport parameters, k'_{0s} needs to be assessed through numerical simulations, solving the Poisson's problem in the solid shape volume (Fig. 4.6). The comparison between the fitting curve and the FEM results is highlighted in Fig. 4.7. The correlation for the *solid static thermal permeability* as function of the geometrical parameters D_t, ξ and t_0 is reported in the following

$$\frac{k'_{0s}}{D_t^2} = 0.001999 t_0^{0.9161} \left(\xi/D_t\right)^{-0.186}. \tag{4.10}$$

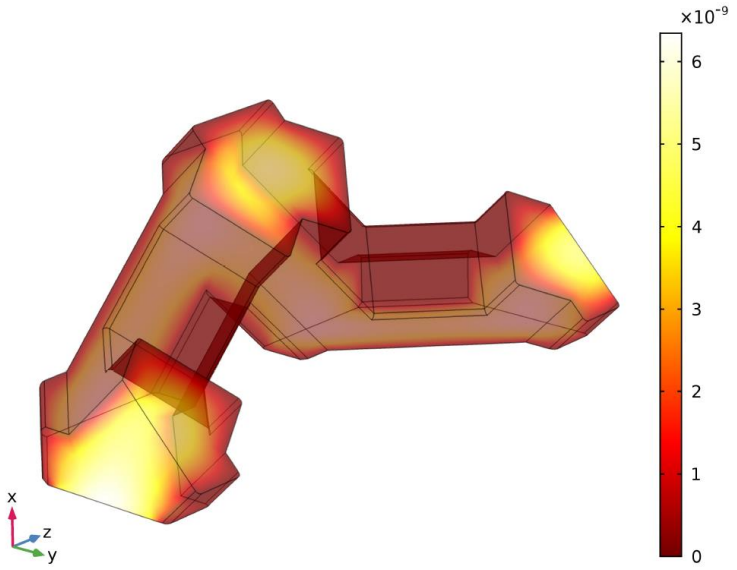

Figure 4.6: Scaled thermal field inside solid volume fraction geometry (one eighth part of the unit cell).

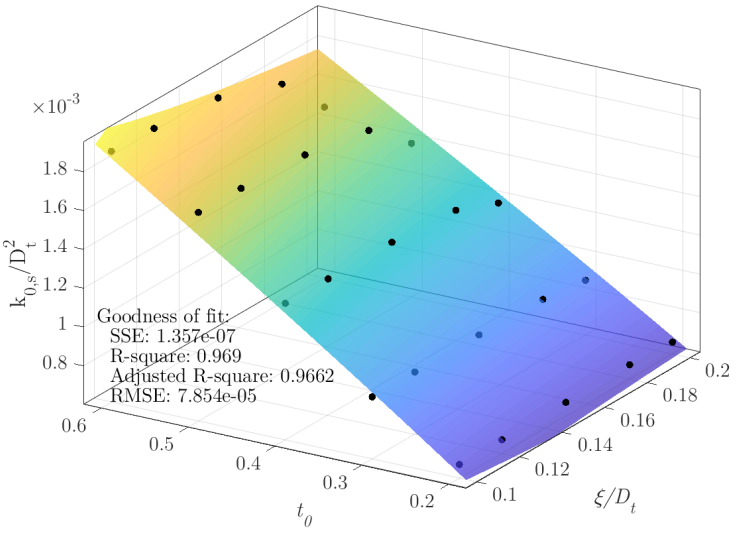

Figure 4.7: Comparison between the fitting curve and the FEM results (black point) for k'_{0s}/D_t^2. Statistical parameters of the goodness of the fit are reported.

Chapter 5

Experimental characterization of the dynamic behaviour of porous materials

Contents

5.1 Introduction

Experimental characterization of the dynamic frequency-dependent properties of a porous material is traditionally carried out through the standard three- and four- microphones techniques. These methodologies require the sample to be tested in a Kundt's tube (or *standing wave* tube). Based on the direct and reflected wave decomposition, the three- [49] and four-[50] microphones tests allow to characterize the transfer matrix between the two sides of the sample [86], Eq. (2.38), and as consequence, the complex density $\tilde{\rho}$ and bulk modulus $\tilde{K}$ (or equivalently the complex wave number $\tilde{k}$ and characteristic impedance $\tilde{Z}_c$, or the thermoviscous functions f_ν and f_κ). The frequency validity range of these two methodologies are linked to the geometrical dimensions of the setup, such as separation distances between adjacent microphones, the inner diameter of Kundt's tube. These technical limitations make it very difficult to obtain accurate measured dynamic properties of material for very low frequencies (under 500 Hz) [87]. Furthermore, it has to be considered that the low frequency range is where porous materials absorb the least amount of acoustic energy. On the other hand, in thermoacoustic applications, porous materials, usually refereed as stack or refrigerator, are used in low frequency range. This is one of the reasons why different measurement techniques have been developed to characterize the viscous and thermal behaviour of porous materials in a very low frequency range. Hayden and Swift [69] introduced a method to measure thermoviscous function f_κ. Wilen and Petculescu developed a method to directly characterize both thermoviscous functions f_ν and f_κ [88, 89, 90]. The limitations of these thermoacoustic methodologies are the complex instrumentation needed to provide the measure (such as a calibrated linear variable differential transformer or a laser beam off a mirror) and the accuracy of the data due to different order of magnitude of measured quantities (harmonic volume displacement and acoustic pressure). Therefore, two novel measurement techniques have been developed to assess experimentally the dynamic properties of porous materials in low frequency range based only on acoustic instrumentation, such as two microphones and a loudspeaker. In this section, a brief review of the standard three- and four microphones techniques is recalled and subsequently the two novel lumped element techniques for low frequency range measurement are presented [53, 52].

5.2 Three-microphones technique

The three-microphone method proposed by Salissou *et al.* [49] allows one to simultaneously determine the normal incidence sound absorption coefficient α, the normal incidence sound transmission loss coefficient $nSTL$, and the effective acoustic properties of the tested porous material by the impedance tube setup shown in Fig. 5.1.a. In this configuration, the porous sample is backed on the rigid termination. Here the sample is assumed to be homogeneous, symmetric, isotropic and acoustically rigid or limp (i.e., it behaves as an equivalent fluid).

From the two pressure transfer function measurements $H_{12} = \frac{p_1}{p_2}$ and $H_{23} = \frac{p_2}{p_3}$, respectively between microphones 2 and 1 and microphones 3 and 2, one can deduce the pressure ratio between the front $(x = 0)$ and the rear face $(x = d)$ of the porous layer as

$$H_{0d} = \frac{1 + r}{e^{ik_A L} + re^{-ik_A L}} H_{23}, \tag{5.1}$$

with r the complex reflection coefficient given by

$$r = \frac{e^{ik_A s} - H_{12}}{H_{12} - e^{-ik_A s}} e^{2ik_A L}. \tag{5.2}$$

Here, s is the spacing between microphones 1 and 2, L is the distance between microphone 2 and the front surface of the porous sample and d is the sample thickness, and $k_A = \omega/c$ is the wave number in the ambient fluid. The surface impedance for $x = 0$ is equal to

$$Z_s = \rho_m c \frac{1+r}{1-r}. \tag{5.3}$$

From the transfer matrix approach and considering that the velocity of the air particle at $x = d$ is equal to zero (*wall* condition), it is shown that the transfer function H_{0d} is equivalent to the first element of the normal incidence transfer matrix T_{11}. Thus, the wave number and the characteristic impedance of the material can be evaluated as

$$\tilde{k} = \frac{1}{d}\cos^{-1}\left(H_{0d}\right), \tag{5.4}$$

$$\tilde{Z}_c = iZ_s \tan\left(\tilde{k}d\right). \tag{5.5}$$

From Eqs. (2.29) and (2.30), the complex density and bulk modulus can be obtained, and as consequence the thermoviscous functions f_ν and f_κ by using Eqs. (2.19) and (2.20) also.

5.3 Four-microphones technique

The four-microphones technique [50], Fig. 5.1.b, allows to assess the amplitude of the direct and reflected wave in the front side and back side of the sample through the four pressure point picked up:

$$A = i\frac{p_1 e^{ik_A x_2} - p_2 e^{ik_A x_1}}{2\sin\left(k_A s\right)}, \tag{5.6a}$$

$$B = i\frac{p_2 e^{-ik_A x_1} - p_1 e^{-ik_A x_2}}{2\sin\left(k_A s\right)}, \tag{5.6b}$$

$$C = i\frac{p_3 e^{ik_A x_4} - p_4 e^{ik_A x_3}}{2\sin\left(k_A s\right)}, \tag{5.6c}$$

$$D = i\frac{p_4 e^{-ik_A x_3} - p_3 e^{-ik_A x_4}}{2\sin\left(k_A s\right)}. \tag{5.6d}$$

Therefore, the acoustic pressure and velocity in the front and rear face of the material can be evaluated as

$$p_0 = A + B, \qquad v_0 = \frac{A - B}{\rho_m c}, \tag{5.7a}$$

$$p_d = Ce^{-ik_A d} + De^{ik_A d}, \quad v_d = \frac{Ce^{-ik_A d} - De^{ik_A d}}{\rho_m c}. \tag{5.7b}$$

From the transfer matrix formulation, Eq. (2.38), the element T_{11} and T_{12} are estimated as

$$T_{11} = \frac{p_0 v_0 + p_d v_d}{p_0 v_d + p_d v_0}, \tag{5.8a}$$

$$T_{12} = \frac{p_0^2 - p_d^2}{p_0 v_d + p_d v_0}, \tag{5.8b}$$

$$T_{21} = \frac{v_0^2 - v_d^2}{p_0 v_d + p_d v_0}. \tag{5.8c}$$

In a similar way to the three microphones techniques, Eqs. (5.4) and (5.5), the complex wave number and the characteristic impedance are in this case equal to

$$\tilde{k} = \frac{1}{d}\cos^{-1}\left(T_{11}\right), \tag{5.9}$$

$$\tilde{Z}_c = \sqrt{\frac{T_{21}}{T_{12}}}. \tag{5.10}$$

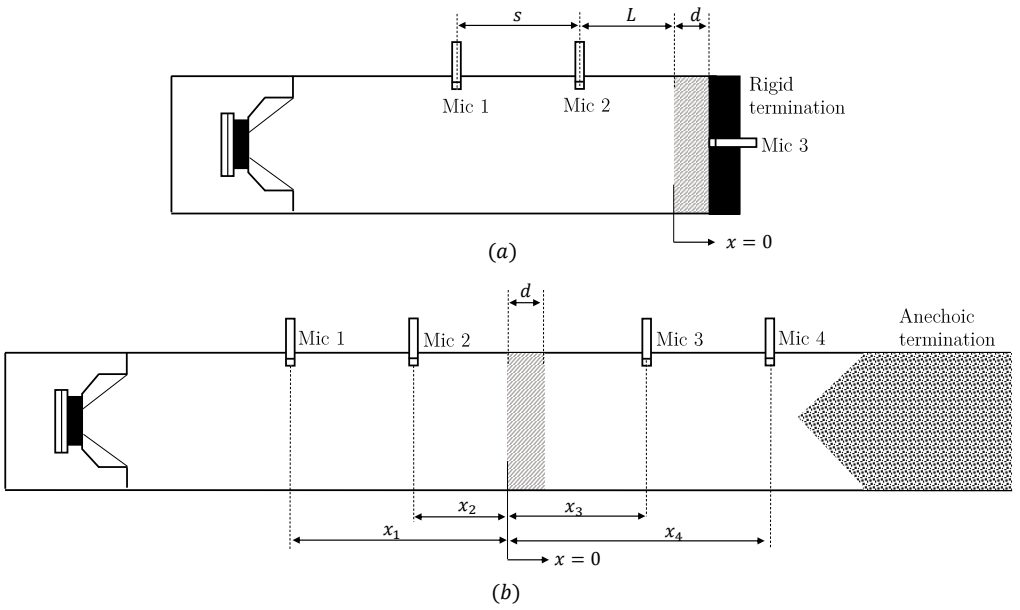

Figure 5.1: Three- (a) and four- (b) microphones techniques set up.

5.4 Novel low frequency lumped element techniques

As reported in subsec. 2.5.1, the wave propagation inside a porous material can be described as a certain number of double bipole linked in series, at limit an infinite number. While, under the lumped element hypotesis, a porous material can be represented by a single double bipole, with its longitudinal impendance $Z_\nu d$ and its transversal admittance $Y_\kappa d$. Lumped element measurement techniques are based on the assumption that the transfer matrix representing a porous material can be expressed, see Eq. (2.47),

$$\begin{bmatrix} p_1 \\ U_1 \end{bmatrix}_{x=d} = \begin{bmatrix} 1 & -\frac{i\omega\tilde{\rho}}{A_f}d \\ -\frac{i\omega A_f}{\tilde{K}}d & 1 \end{bmatrix} \begin{bmatrix} p_1 \\ U_1 \end{bmatrix}_{x=0}. \tag{5.11}$$

The fundamental hypothesis which allows to describe a porous material using only a double bipole is expressed as

$$|\tilde{k}d| < 0.5. \tag{5.12}$$

The quantity $|\tilde{k}d|$ is the absolute value of the complex dimensionless wave number, depending on the material properties $\tilde{k}$ and its thickness d.

5.4.1 Complex density

To measure the complex density $\tilde{\rho}$, viscous behaviour should be highlighted. Looking at the two-port network shown in Fig. 5.2, this can be accomplished if a very low impedance value Z_{rad} (ideally a short-circuit) is considered. This condition can be realized by placing the sample between the acoustic source and an open-end. It will be shown that this is equivalent to have a uniform acoustic volume velocity across the material (i.e. with reference to Fig. 5.2.b this means to have $U_{x=0} \approx U_{x=d}$). As shown in Fig. 5.3, the method proposed by Di Giulio *et al.* [52] is based on two measurements with (refereed as *full*) and without (refereed as *empty*) the material to be tested and by considering the same measurement set up. In this way, it is possible to assume the same boundary conditions or, in other words, the same acoustic impedance at the open-end (section $x = d$) in the two measurements. As will be shown shortly, the latter allows to assess the complex density $\tilde{\rho}$ without knowing the impedance value at the open end of the tube, $x = d$. In the empty case, neglecting the losses at the edges of the tube, (an ideal gas fulfils the opened cavity), it can be written as follows

$$\begin{bmatrix} p_1 \\ U_1 \end{bmatrix}_{x=d} = \begin{bmatrix} 1 & -\frac{i\omega\rho_m}{A_f}d \\ -\frac{i\omega A_f}{\gamma p_m}d & 1 \end{bmatrix} \begin{bmatrix} p_1 \\ U_1 \end{bmatrix}_{x=0}. \tag{5.13}$$

The acoustic pressure at the open-end section $x = d$ can be derived from Eqs. (5.11), (5.13) as function of the measured pressure in the section $x = x_{mic}$, named p_{up}, as follows

$$p_{x=d,full} = p_{up,full} - \frac{i\omega\tilde{\rho}}{A\varphi}\left(d - x_{mic}\right)U_{1,full}, \tag{5.14a}$$

$$p_{x=d,empty} = p_{up,empty} - \frac{i\omega\rho_m}{A}\left(d - x_{mic}\right)U_{1,empty}, \tag{5.14b}$$

where the lumped element hypothesis and the low value of the radiation impedance allow to assume the uniform volume velocity across the porous sample equal to U_1. By dividing both Eqs. (5.14a) and (5.14b) by U_1, the expressions of the surface impedance at open-end section are found for the full and empty cases. Therefore, by equalling these expressions it follows

$$\left(\frac{p}{U}\right)_{x=d} = \left(\frac{p_{up}}{U_1}\right)_{full} - \frac{i\omega\tilde{\rho}}{A\varphi}\left(d - x_{mic}\right) = \left(\frac{p_{up}}{U_1}\right)_{empty} - \frac{i\omega\rho_m}{A}\left(d - x_{mic}\right). \tag{5.15}$$

Assuming that the dimension of the air volume behind the loudspeaker (lower chamber) is much smaller than the wavelength, the acoustic volume velocity can be evaluated as [43]

$$U_1 = -i\omega\frac{V_{dw}}{\gamma p_m}p_{dw}, \tag{5.16}$$

where V_{dw} is the volume of the lower chamber and p_{dw} the acoustic pressure therein. By substituting Eq. (5.16) in (5.15), the complex density of the tested sample can be evaluated as

$$\tilde{\rho} = \varphi\left(\rho_m + \frac{\gamma p_m A}{\omega^2 V_{dw}\left(d - x_{mic}\right)}\left[\left(\frac{p_{up}}{p_{dw}}\right)_{full} - \left(\frac{p_{up}}{p_{dw}}\right)_{empty}\right]\right). \tag{5.17}$$

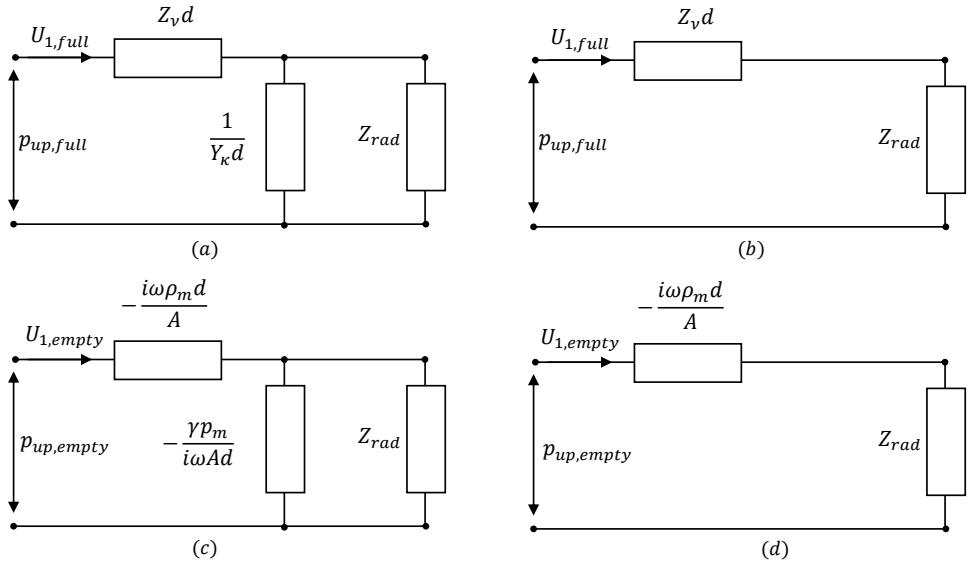

Figure 5.2: The acoustic transmission line of a porous material (a) and free air (c) placed close to an open-end section. The case of negligibility of the transveral acoustic impedance in the case of the material (b) and free air (d).

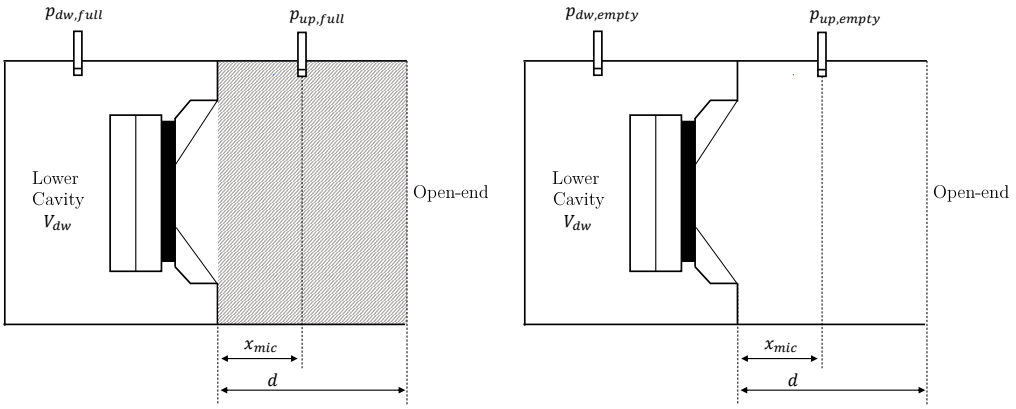

Figure 5.3: The acoustic setup to measure the complex density for the *full* configuration, on the left, and *empty* configuration, on the right.

Negligibility of radiation impedance

As reported in Fig. 5.2, a low value of the radiation impedance Z_{rad} is required to realize the short-circuit condition in the equivalent electro-acoustic network. The radiation impedance is expressed, for circular tube with inner radius R, as [20]

$$Z_{rad} = \frac{\rho_m c}{A}\left(\frac{(k_A R)^2}{4} + 0.6ik_A R\right). \tag{5.18}$$

The effect of the presence of radiation impedance can be considered negligible when $k_A R < 0.5$. Therefore, the greater the tube radius, the smaller the frequency range for which Z_{rad} is negligible. In some cases, the condition $k_A R < 0.5$ can be more restrictive than the one for the validity of lumped element approximation $|\tilde{k}d| < 0.5$. To clarify this statement, Fig. 5.4 reports $k_A R$ as a function of frequency, for three different radius values $(R = 3, 5, 10\ cm)$, compared with the values of $|\tilde{k}d| < 0.5$ obtained for a porous material with thickness of $3.5\ cm$ and three different values of airflow resistivity $\left(\sigma = 5000,\ 10000,\ 40000\ (Pa \cdot s)/m^2\right)$. It can be noted that, up to a certain radius of the tube and for higher value of airflow resistivity (or what is the same for higher value of thickness), $|\tilde{k}d| < 0.5$ is more restrictive than $k_A R < 0.5$ because the cut-off frequency is smaller. On the other hand, for higher values of R and smaller value of airflow resistivity (or what is the same for smaller value of thickness), the cut-off frequency it is affected by $k_A R$. In Fig. 5.4, numerical simulations on the same material ($d = 0.046\ m$ and $\sigma = 2600 Pa \cdot s/m^2$) are compared for different values of the tube radii: (a) $R = 3\ cm$ where the lumped-element condition is more restrictive than the impedance radiation negligibility, (b) $R = 5\ cm$ where the two limit condition are very close, (c) $R = 10\ cm$ where the negligibility of Z_{rad} provides a frequency limit smaller than the lumped-element condition.

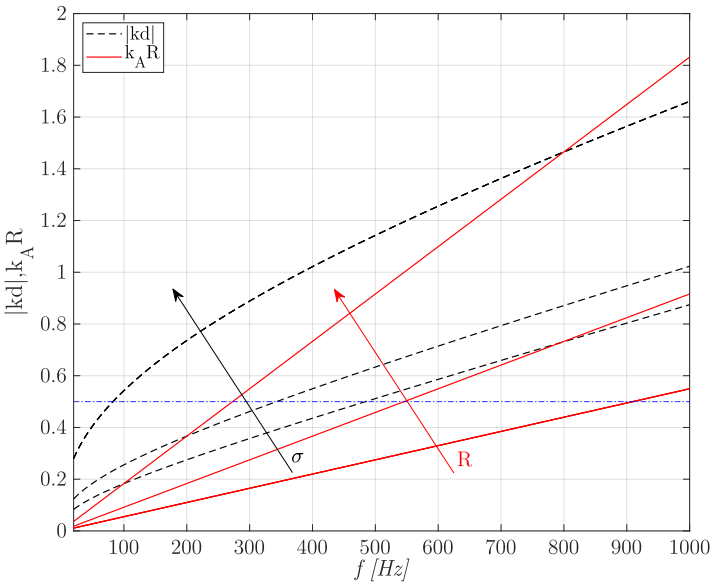

Figure 5.4: $|\tilde{k}d|$, for a porous material with thickness $3.5\ cm$ with three different values of airflow resistivity $\left(\sigma = 5000, 10000, 40000\ Pa \cdot s/m2\right)$ and $k_A R$, with three different dimensions of the tube radius $R = 3, 5, 10\ cm$ versus frequency.

5.4.2 Complex bulk modulus

Dynamic thermal behaviour of a porous material is expressed through its complex bulk modulus $\tilde{K}$, which determines the transversal admittance $Y_\kappa d$. Therefore, in order to characterize this quantity using an equivalent circuit representation, viscous behaviour should be neglected, i.e. the longitudinal viscous impedance [53]. The condition reported in Fig. 5.6 can be realized through

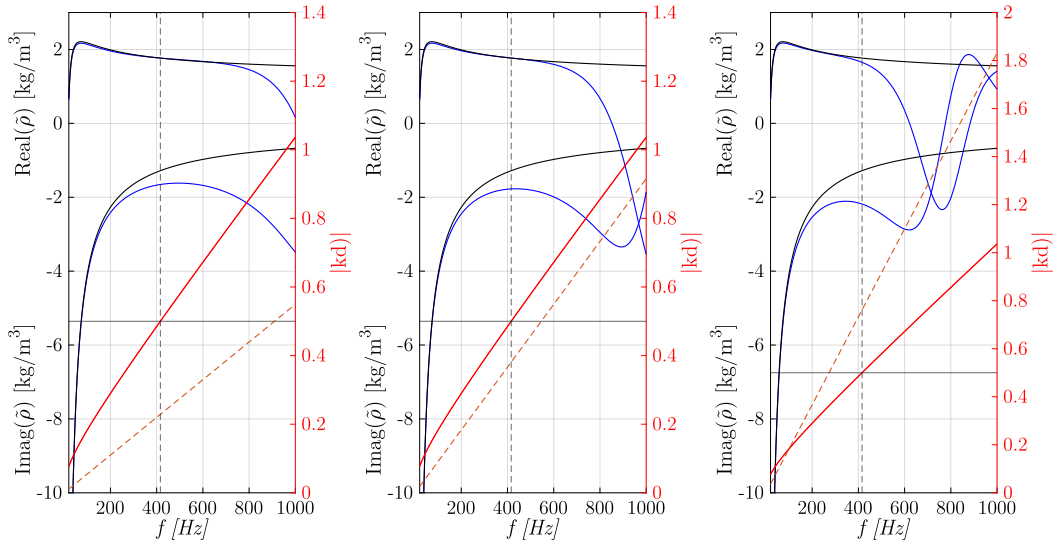

Figure 5.5: The comparison between $\tilde{\rho}_{theoretical}$ (black line) and $\tilde{\rho}_{lumped-element}$ (blue line) for a sample with thickness $d = 4.6\ cm$ and $\sigma = 2600\ Pa \cdot s/m^2$ plotted versus frequency f referred to as left y axes. The $|\tilde{k}d|$ parameter (continuous red line) and $k_A R$ (dashed red line) referred to as the right y axes: (a) $R = 3\ cm$, (b) $R = 5\ cm$, (c) $R = 10\ cm$. The black vertical dashed-dotted line represents the cut-off frequency corresponding to $|\tilde{k}d| = 0.5$ (red horizontal line). The black vertical dashed line represents the frequency corresponding to $k_A R = 0.5$.

two assumption: by adding a very high values transversal impedance, parallel to $Y_\kappa d$, borderline an infinite value such as a perfect hard wall condition, and neglecting the viscous impedance over the thermal one which mathematical means, using Eqs. (2.29) and (2.30),

$$Z_\nu d \ll \frac{1}{Y_\kappa d} \rightarrow \sqrt{\frac{Z_\nu d}{\frac{1}{Y_\kappa d}}} = \sqrt{Z_\nu Y_\kappa d^2} = |i\tilde{k}d| \approx 0. \tag{5.19}$$

Under this hypothesis, the acoustic pressure in the cavity where the material is placed in, which can be considered uniform $\left(p_{1,x=0} = p_{1,x=d} = p_{up}\right)$. Therefore, expressing $U_{1,x=0}$ from the Eq. (5.16), the surface admittance at the back-end section $x = d$ in the *full* and *empty* cases can be derived by dividing Eqs. (5.11), (5.13) for p_{up} as follows

$$\left(\frac{U_{x=d}}{p_{up}}\right)_{full} = -i\omega\frac{V_{dw}}{\gamma p_m}\left(\frac{p_{dw}}{p_{up}}\right)_{full} - i\omega\frac{V_{up}\varphi}{\tilde{K}}, \tag{5.20a}$$

$$\left(\frac{U_{x=d}}{p_{up}}\right)_{empty} = -i\omega\frac{V_{dw}}{\gamma p_m}\left(\frac{p_{dw}}{p_{up}}\right)_{empty} - i\omega\frac{V_{up}}{\gamma p_m}. \tag{5.20b}$$

These surface admittance (equivalently the surface impedance) are equal in the configurations *empty* and *full* since both are characterized by the same boundary conditions at the end section $x = d$, as in Fig. 5.7. Consequently, it follows that

$$\tilde{K} = \frac{\gamma p_m}{\frac{1}{\varphi} - \frac{V_{dw}}{V_{up}\varphi}\left[\left(\frac{p_{dw}}{p_{up}}\right)_{full} - \left(\frac{p_{dw}}{p_{up}}\right)_{empty}\right]}. \tag{5.21}$$

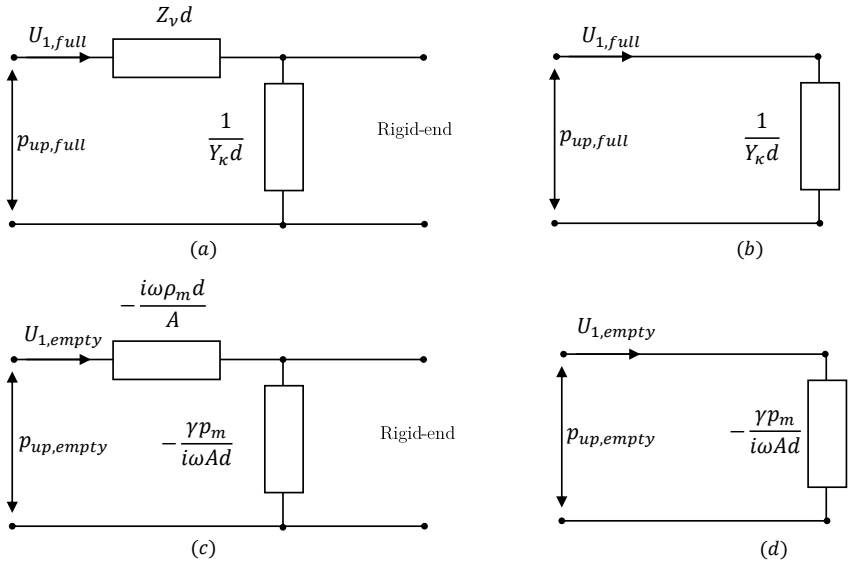

Figure 5.6: The acoustic transmission line showing: the complete thermo-viscous model and the model neglecting transversal viscous impedance respectively for the material (a) and (b), and in free air (c) and (d).

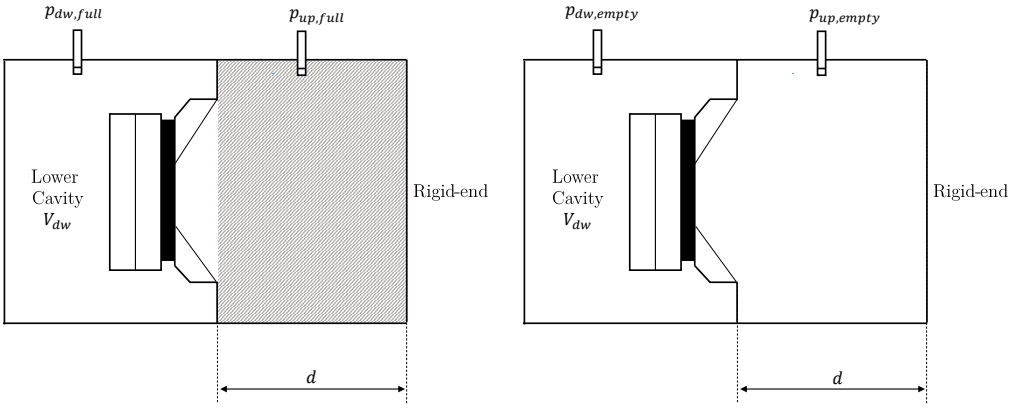

Figure 5.7: The acoustic setup to measure the complex bulk modulus for the *full* configuration, on the left, and *empty* configuration, on the right.

Negligibility of viscous impedance over the thermal admittance

The airflow resistivity is taken as a reference parameter for the viscous losses of the two materials and it is set to $\sigma = 1000\ Pa \cdot s/m^2$ and $\sigma = 10000\ Pa \cdot s/m^2$ in the two cases. The error provided by the lumped element approach, can be expressed as:

$$\epsilon\left(\omega\right) = \left|1 - \frac{\tilde{K}_{lumped\ element}}{\tilde{K}_{theoretical}}\right| \times 100, \tag{5.22}$$

with $\tilde{K}_{lumped\ element}$ and $\tilde{K}_{theoretical}$ the complex bulk moduli value given, respectively, by the numerical simulations and JCAL model. In Fig. 5.8 the values of the complex bulk modulus given by the numerical simulations and JCAL model are plotted versus the dimensionless parameter, $|\tilde{k}d|$ (upper x-axis). $|\tilde{k}d|$ is used to estimate the reliability range of the lumped approximation, since $|\tilde{k}d|$ is directly related to the phase variation and attenuation of the acoustic pressure throughout the porous material. By looking at the Figs. 5.8.a and 5.8.b, it is easy to verify that, for both materials, ϵ is smaller than 5% when $|\tilde{k}d| < 0.5$. Thus, $|\tilde{k}d| < 0.5$ can be taken as a criterion to assess the upper limit of frequency validity range of the proposed method. Eq. (5.19) implies that, limiting $|\tilde{k}d|$ to small values, the transversal viscous impedance Z_ν d is negligible with respect to the thermal impedance $1/Y_\kappa$ d of the material. Chosen $|\tilde{k}d| \approx 0.5$ as a limiting value, the surface plots in Fig. 5.9 and Fig. 5.10 show the range of application of the method in terms of frequency, material thickness and airflow resistivity values. Moreover, from Fig. 5.10, an important consideration can be done regarding the cut-off frequency for a fixed airflow resistivity value, the smaller the sample thickness, the higher the frequency limit. For a fixed the thickness value, the greater the airflow resistivity, the lower the frequency limit.

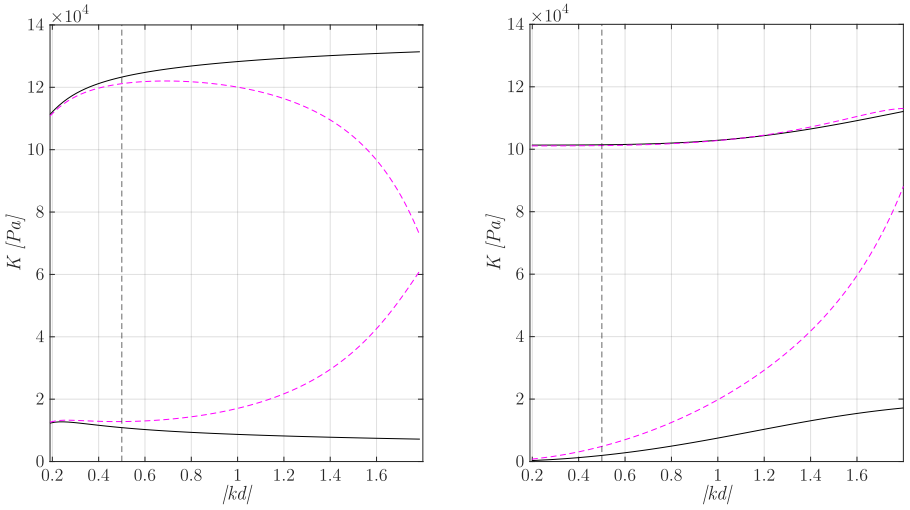

Figure 5.8: The comparison between $\tilde{K}_{theoretical}$ (black line) and $\tilde{K}_{lumped\ element}$ (magenta dashed line) for a sample with thickness $d = 0.08\ m$,$\varphi = 0.99$ and transport parameters $\Lambda = 2e-4\ m, \Lambda' = 2\Lambda, \alpha_\infty = 1, k_0' = 2k_0 = 2\mu/\sigma$, where $\sigma = 1000\ Pa \cdot s/m^2$ on the left and $\sigma = 10000\ Pa \cdot s/m^2$ on the right. black vertical dashed line represents the limit value $|\tilde{k}d| = 0.5$.

Microphone position

The lumped element technique requires a uniform acoustic pressure inside the porous sample but as seen in the previous section, there is always a certain variation on the acoustic pressure along the sample. This variation is sufficiently small, to obtain reliable results, when $|\tilde{k}d| < 0.5$. However, it is important to highlight the dependence of the measurement results from the position of the microphone in the upper cavity (see Fig. 5.11). The outcomes of several numerical simulations, which are intended to investigate this problem, are plotted in Fig. 5.12. It reports the value of the complex bulk modulus given by numerical simulations and obtained by the sound pressure picked at different positions in the upper chamber and compared with the $\tilde{K}_{theoretical}$. In particular, three microphone positions were considered in the upper cavity: front (blue line), rear (red line) and middle (magenta line) position. It can be observed that the best location for the microphone is in

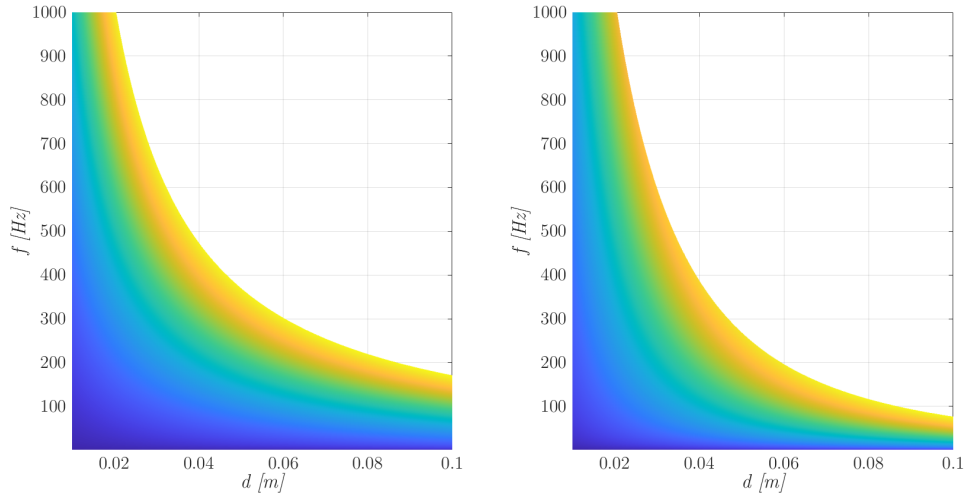

Figure 5.9: The surface plot of $|\tilde{k}d|$ as a function of the frequency range and specimen thickness for a sample with $\varphi = 0.99$ and transport parameters $\Lambda = 2e-4\ m, \Lambda' = 2\Lambda, \alpha_\infty = 1, k_0' = 2k_0 = 2\mu/\sigma$, where $\sigma = 1000\ Pa \cdot s/m^2$ on the left and $\sigma = 10000\ Pa \cdot s/m^2$ on the right.

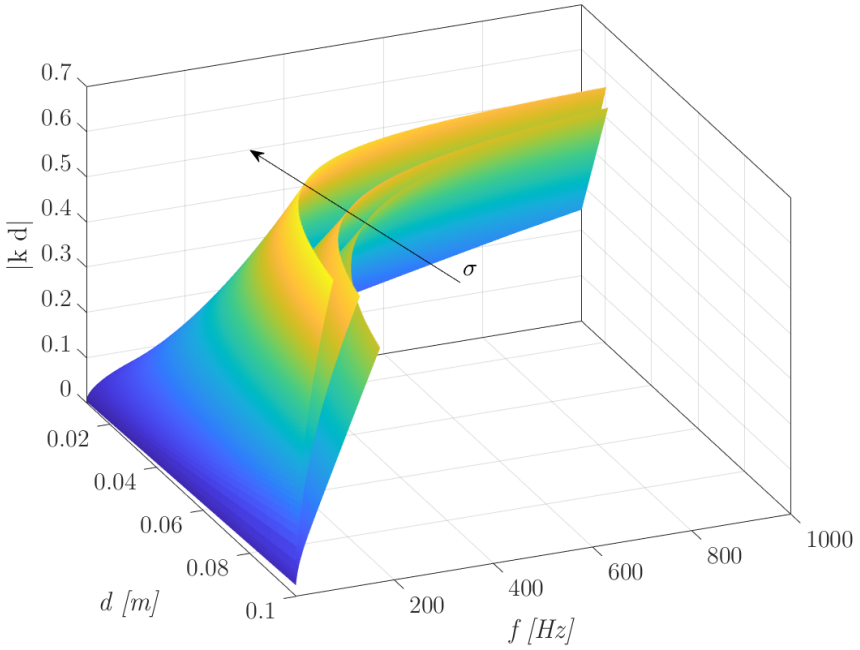

Figure 5.10: The 3D-surface plot of $|\tilde{k}d|$ for increasing values of the airflow resistivity σ.

the middle of the sample, as it provides approximately an averaged value of the sound pressure that occurs in the cavity, with and without porous material. Results in Fig. 5.12 show that the numerical value of the complex bulk modulus given by numerical simulations and obtained by front (blue line in Fig. 5.12) and rear (red line in Fig. 5.12) sound pressure can diverge from theoretical one also for values of $|\tilde{k}d|$ less than 0.5 whereas the agreement is good enough for results obtained by the middle microphone (magenta line in Fig. 5.12).

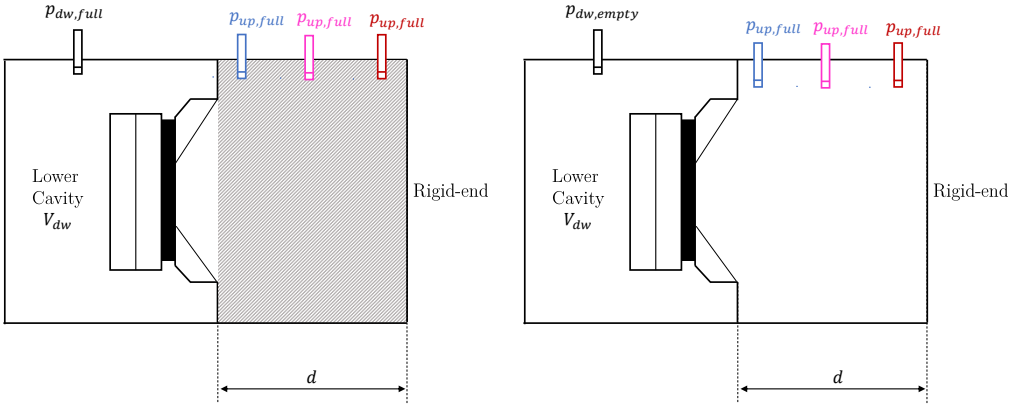

Figure 5.11: The different microphone positions along the porous material, indicating the behind section of the sample in red, the front section of the sample in blue, and the middle section of the sample in magenta.

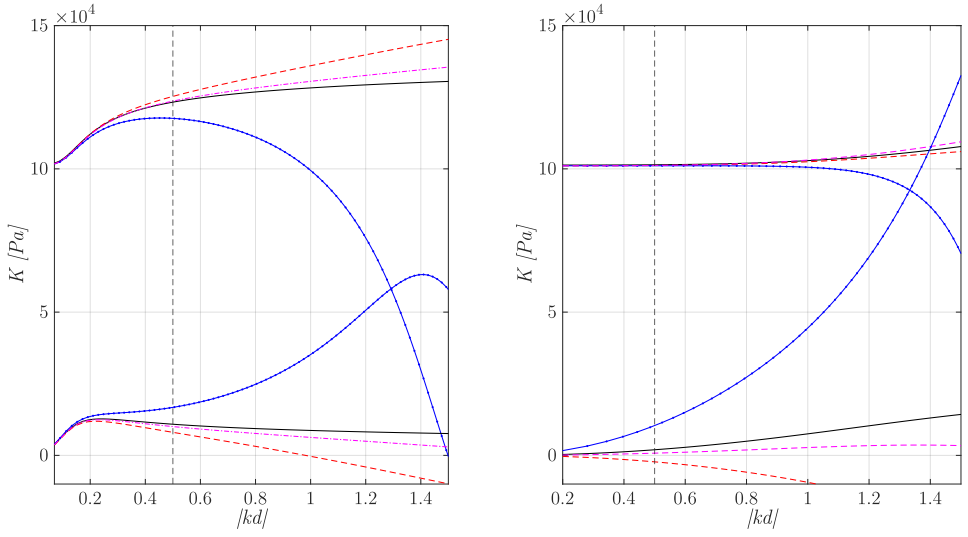

Figure 5.12: The comparison between $\tilde{K}_{theoretical}$ (black line) and $\tilde{K}_{lumped\ element}$, where the acoustic pressure p_1 is estimated behind (dashed lines, dashed red line), in front (blue point and line), and in the middle section (magenta dashed line) of the material. On the left and on the right, the materials have respectively the same transport properties as those in Fig. 5.8.a and 5.8.b. the black vertical dashed line (dashed lines) represents the limit value $|\tilde{k}d| = 0.5$.

5.5 Experimental results

The experimental apparatus for the low frequency measurements of the thermal and viscous functions inside porous media are sketched in Figs. 5.3 and 5.7. In particular, driver and sample holder must be sealed up to avoid air leakages. The first step is to provide accurate measurements of lower

and upper volumes, V_{dw} and V_{up}, that are fundamental for the calibration of the measurement system. An acoustic method for the evaluation of the volume cavities, i.e. acoustic compliance, is proposed by Dragonetti *et al.* [43]. The porous medium should occupy most of the volume in the upper cavity. Therefore, a movable termination has to be set at the end of the sample in the bulk modulus measurement while acoustic tubes with same inner radius different length of the sample must be employed. After a first estimation of the volume of the cavities, the only parameter of the sample that must be known is the open porosity φ. Therefore, two measures must be carried out: one without the testing sample, where the volume in the upper cavity is fulfilled only by air, and one with the testing sample. The different typologies of the samples with various thicknesses and airflow resistivity have been tested to validate the experimental methodology, such as: a fibrous material sample, triangular pore sample, Wire Mesh samples and 3D-membrane foams. Experimental data are partially extracted from the works of Di Giulio *et al.* [52], Di Giulio *et al.* [68] and Napolitano *et al.* [53]

Fibrous material

The tested fibrous sample is a polyester fiber specimen, commercially named Edilfiber. The airflow resistivity has been measured though the Dragonetti *et al.* [43] method and it is 1850 $Pa \cdot s/m^2$. The experimental results are compared with the results provided by Miki's model, which is reliable for fibrous material.
For the complex density measurements, results are plotted by using two y axes versus the frequency f on x axes: on the left the real and imaginary part of complex density, on the right the dimensionless $|\tilde{k}d|$ (continuous red line) and $k_A R$ (dashed red lines) parameters to highlight the validity range of the lumped element technique. It will be the lower frequency value between the two criteria: $|\tilde{k}d| < 0.5$ or $k_A R < 0.5$. The $|\tilde{k}d|$ parameter is proportional to the frequency, sample thickness and viscous dissipation (or viscous impedance $Z_\nu d$). Therefore, the higher the viscous dissipation (strictly related to airflow resistivity σ) or the sample thickness d, the lower the frequency validity range of lumped element technique. In Fig. 5.13 , results obtained for Edilfiber sample are reported. As it can be seen the deviation of experimental data from the model increases when the frequency decreases. This is attributed to the acoustic source which is not particularly designed for the pure low frequencies, and it has been adapted for the measurement frequency range.
Also in the case of the bulk modulus measurement, the data are plotted versus two x axes: the frequency on the lower axis and the parameter $|\tilde{k}d|$ on the upper axis. As expected, the experimental results are coherent with the theoretical predictions up to cut-off frequency (Fig. 5.14).

Triangular pore sample

This sample with uniform cross section areas has been tested, for which an analytical solutions for both $\tilde{\rho}$ and $\tilde{K}$ exist:

$$\tilde{\rho} = \rho_m \epsilon^2 \left[\epsilon^2 - 3\epsilon \coth(\epsilon) + 3\right], \tag{5.23a}$$

$$\tilde{K} = \gamma p_m \left(\gamma - \frac{\gamma - 1}{P_r \epsilon^2}\left[P_r \epsilon^2 - 3\sqrt{P_r}\epsilon \coth\left(\sqrt{P_r}\epsilon\right) + 3\right]\right)^{-1}. \tag{5.23b}$$

where $\epsilon = \frac{t}{2}\sqrt{\frac{3i\omega\rho_m}{\mu}}$, being t the dimension on the side of the triangle. As for the Edilfiber sample, results are reported against two y and x axes to highlight the validity range of the measurement techniques respectively in Figs. 5.15 and 5.16.

Wire Mesh

Three different Wire Mesh samples have been tested: in Fig. 5.17.a, Wire Mesh 1, $r_p = 0.35\ mm$, $d_s = 3.07\ mm$, in Fig. 5.17.b, Wire Mesh 2, $r_p = 0.3\ mm$, $d_s = 2.30\ mm$, and in Fig. 5.17.c, Wire Mesh 3, $r_p = 0.2\ mm$, $d_s = 1.63\ mm$. For these samples, the experimental results are reported in terms of the viscous and thermal functions, f_ν and f_κ, equivalent to complex density $\tilde{\rho}$ and bulk modulus $\tilde{K}$ through Eqs. (2.19) and (2.20). Figs. 5.18, 5.19, 5.20 compare the experimental results obtained though the lumped element techniques with the theoretical model combining the JCAL approach with the proposed transport parameter derivations (Tab. 4.2). Experimental data are generally in good agreement with the theoretical predictions both for the viscous and thermal behaviours. Based on the equations reported in Tab. 4.2 and the Eqs. (3.4c), (3.11c), the estimated values of the viscous $f_{\nu t} = \mu\varphi/\left(2\pi\rho_m\alpha_\infty k_0\right)$ and thermal $f_{tt} = \kappa\varphi/\left(2\pi\rho_m c_p k_0'\right)$ transition frequencies, for the three wire mesh samples that were characterized (Wire Mesh 1 to 3), are respectively equal to $19, 32, 65\ Hz$ and $14, 21, 45\ Hz$. Therefore, most of the measured behaviours of the viscous f_ν and thermal f_κ. functions correspond only to the inertial and adiabatic regimes. Some differences between the experimental data and the model were observed for the imaginary part of the thermal response function, f_κ (below 50 Hz). This resulted mostly because of difficulties inherent to the measurement technique, which requires a perfectly sealed setup to avoid air losses and an acoustic source able to support the front and rear compliance volumes. As said above, in the employed experimental setup the used acoustic source was not properly designed to work under such low frequencies. As a consequence, an increasing standard deviation was characterized when the frequency decreases. Specifically, the difference in amplitude between the experimental results and the model predictions for the thermal function f_κ of the Wire Mesh 1 (Fig. 5.18) resulted mostly from the fact that a larger thermal permeability k_0' was observed when compared with the other samples (Tab. 4.2). In agreement with the previous statement about the thermal transition frequency f_{tt}, the associated transition between the isothermal and adiabatic regimes of $14\ Hz$ indicates that an accurate measurement of both the real and imaginary part of f_κ would require a specifically designed experimental setup.

3D-membrane foams

3D-membrane foam samples have been realized through an additive manufacturing techniques, in particular, *Fused Deposition Modelling* (FDM) from plastic filaments has been used. FDM forms a 3D geometry by assembling individual layers of extruded thermoplastic filament, such as acrylonitrile butadiene styrene (ABS) or polylactic acid (PLA), which have melting temperatures low enough for use in melt extrusion in outdoor non-dedicated facilities. However, the complex geometries of the unit cell (Fig. 4.5.a) make difficult to have an high accuracy in the realization of the entire sample. Several issues can be highlighted, such as: the low opening ratio t_0 of the membrane which can determine the total closure of the membrane during the process, the small dimensions both of the unit cell and the thickness of the membrane which could not mechanically support the structure itself. Taken into account these realization problems, three unit cells have been chosen and realized based on the minimum dimension that can be printed with the employed technology, $0.8\ mm$. Therefore, the three samples (named S1, S2 and S3) have all the same dimension for the unit cell and the thickness of the membrane, respectively $D_t = 8\ mm$ and $\xi = 0.8\ mm$, and they differs for the opening ratio, which is fixed equal to $t_0 = 0.6$ for S3 (Fig. 5.21.a), $t_0 = 0.4$ for S2 (Fig. 5.21.b), $t_0 = 0.25$ for S1 (Fig. 5.21.c). All the samples have the same thickness $d = 6\ cm$. In order to underline the equivalence between the two dynamic parameters description of porous materials, results are reported in terms of complex density and bulk modulus for the Edilfiber and Triangular pore sample, the thermoviscous functions for the Wire Mesh samples, and finally in terms of dynamic permeabilities $\tilde{k}_\nu$ and $\tilde{k}'$ for the 3D-Membrane Foams. As for the Wire Mesh

samples, the experimental results compared to the theoretical model (transport parameters correlations in Tab. 4.3 coupled with JCAL semi-phenomenological model) are reported in Figs. 5.22, 5.23, 5.24. From each plot it can be highlighted that the low frequency limit of the real part of both viscous and thermal permeability achieves the static value, while the imaginary part tend to zero. Furthermore, plots with zoomed scale on y-axis are reported for each thermal permeability $\tilde{k}'$ in order to highlight the coherence between the model and the measured data. As expected, the sample S1 is characterized by the highest airflow resistivity (lowest static viscous permeability k_0) among the samples (respectively $k_0 = 2.4841e-8\ m^2, 1.0501e-7m^2, 3.7696e-7m^2$ for S1, S2 and S3). This is due the lower value of the opening ratio t_0 of the membrane which is the control parameter for the viscous behaviour. While, from a thermal point of view, the three samples behave in a very similar way, because the thermal permeability has a weak dependence on the opening ratio t_0 ($k'_0 = 8.7551e-7m^2, 9.6262e-7m^2, 1.2482e-6m^2$ for S1, S2 and S3). Additionally, the acoustic source is adapted to operate in a frequency range for which it was not specifically designed, rather than being a low frequency generator like a woofer. As a consequence, few deviations of the experimental results from the predictive model can be mentioned from Figs. 5.22 (right), 5.23, 5.24 (left), in particular under $50Hz$.

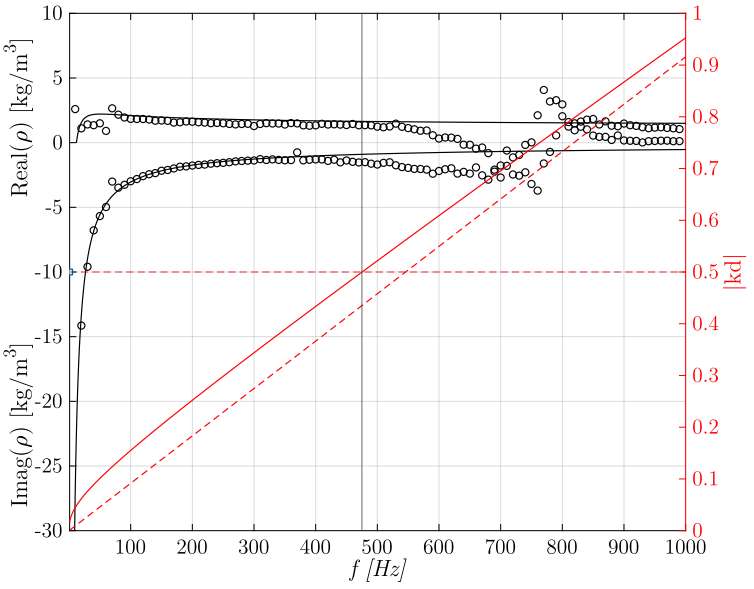

Figure 5.13: The Edilfiber showing Miki's model (continuous black line) and the experimental data (lumped element technique) referred to as the left y axes. The $|\tilde{k}d|$ parameter (continuous red line) and $k_A R$ (dashed red line) referred to as the right y axes. The vertical dashed-dotted line represents the cut-off frequency corresponding to $|\tilde{k}d| = 0.5 (k_A R = 0.5)$ (horizontal red line).

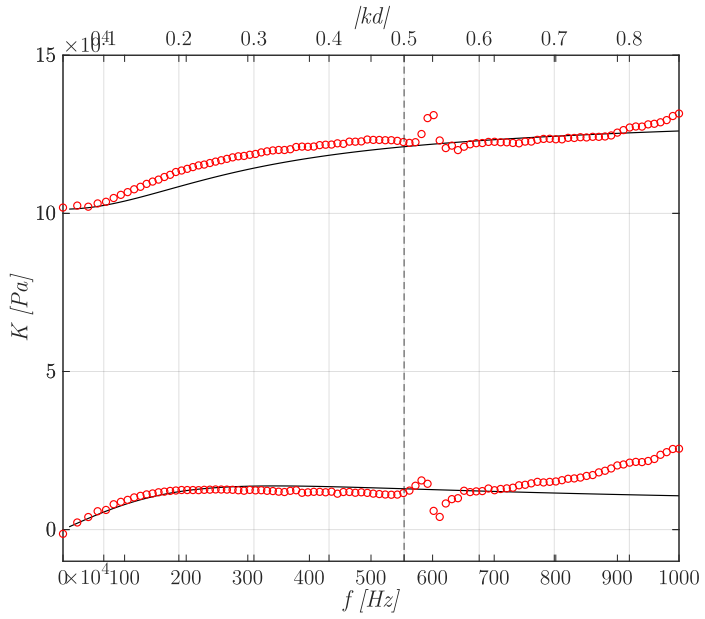

Figure 5.14: The Edilfiber, EF, showing Miki's model (continuous black line), experimental data (red circle points). The black vertical dashed line (dashed lines) represents the limit value $|\tilde{k}d| = 0.5$.

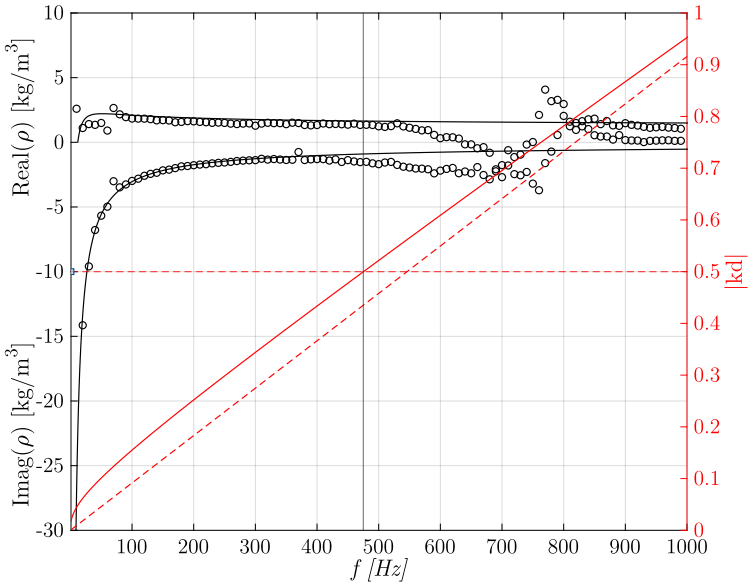

Figure 5.15: The Triangular pore sample showing the analytical curve, Eq. 5.23a (continuous black line) and the experimental data (circle points) referred to as the left y axes. The $|\tilde{k}d|$ parameter (continuous red line) and $k_A R$ (dashed red line) referred to as the right y axes. The black vertical dashed-dotted line represents the cut-off frequency corresponding to $|\tilde{k}d| = 0.5 (k_A R = 0.5)$ (horizontal red line).

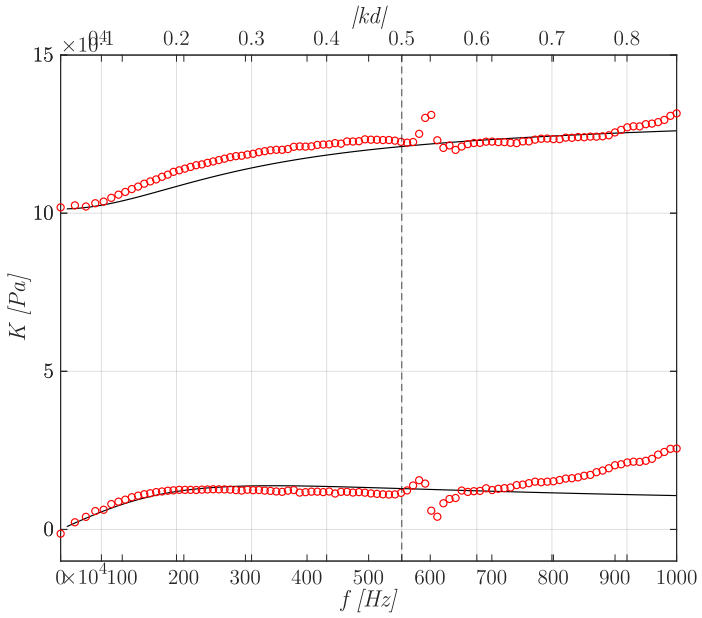

Figure 5.16: The triangular pore structure showing the analytical curve, Eq. 5.23b (continuous black line) and experimental data (circle points). The black vertical dashed line (dashed lines) represents the limit value $|\tilde{k}d| = 0.5$.

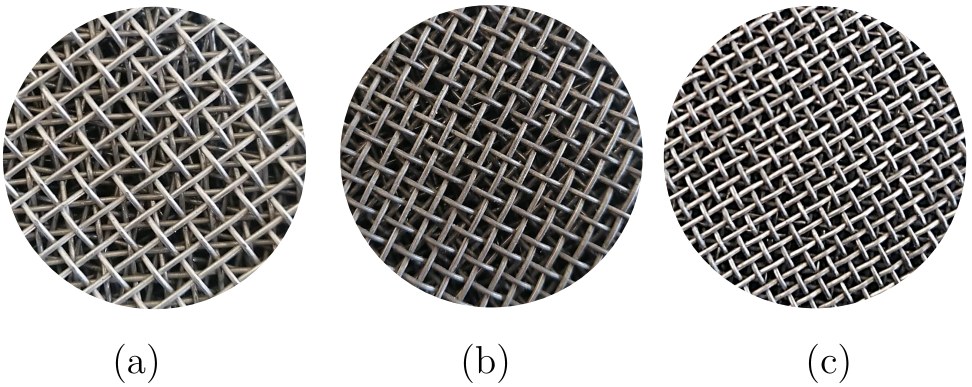

Figure 5.17: Three Wire Mesh samples: (a) Wire Mesh 1, $r_p = 0.35\ mm,\ d_s = 3.07\ mm$, (b) Wire Mesh 2, $r_p = 0.3\ mm,\ d_s = 2.30\ mm$, (c) Wire Mesh 3, $r_p = 0.2\ mm,\ d_s = 1.63\ mm$.

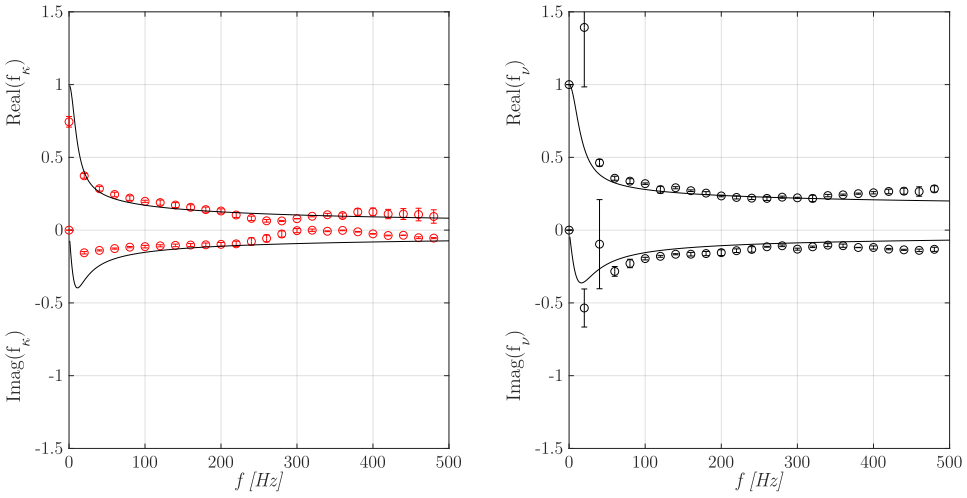

Figure 5.18: Wire mesh 1: Comparison between experimental results (red circular points, mean value $\pm$ standard deviation) and modelling approach (continuous black line). Real and imaginary parts of the frequency-dependent (a) thermal function f_κ and (b) viscous function f_ν.

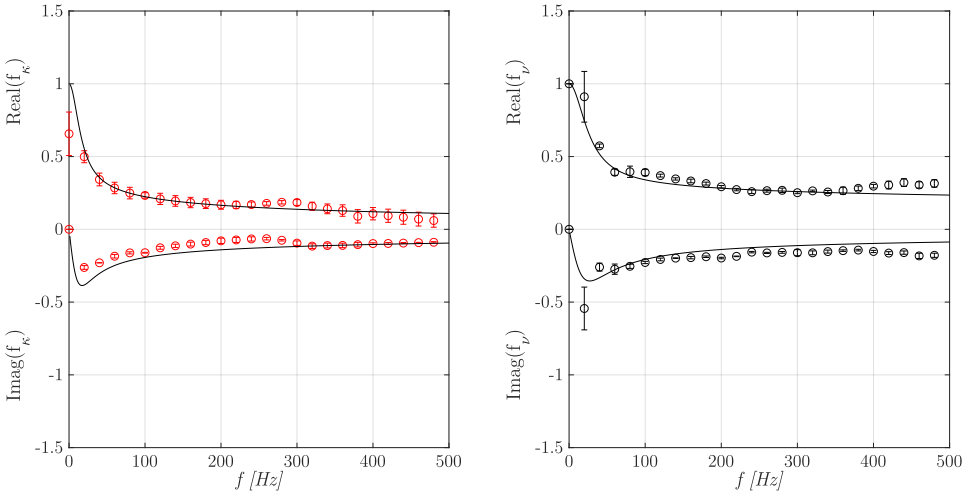

Figure 5.19: Wire mesh 2: Comparison between experimental results (red circular points, mean value $\pm$ standard deviation) and modelling approach (continuous black line). Real and imaginary parts of the frequency-dependent (a) thermal function f_κ and (b) viscous function f_ν.

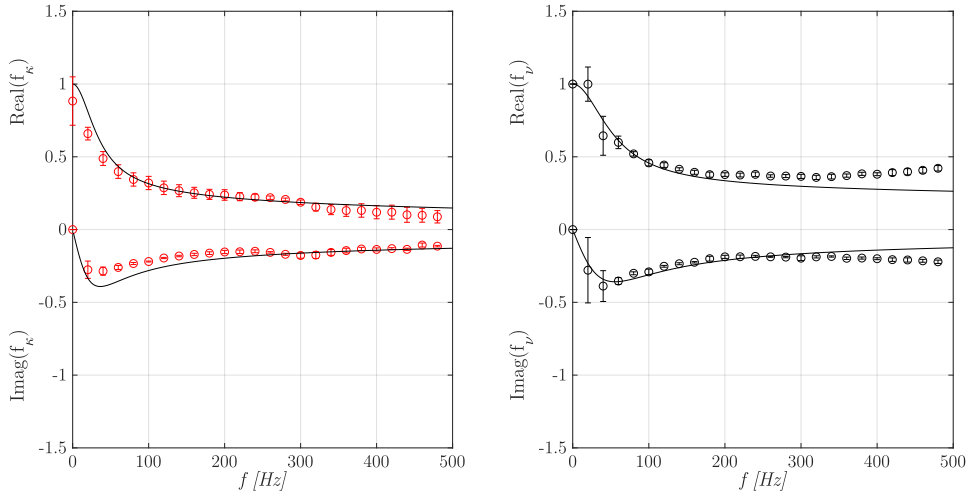

Figure 5.20: Wire mesh 3: Comparison between experimental results (red circular points, mean value $\pm$ standard deviation) and modelling approach (continuous black line). Real and imaginary parts of the frequency-dependent (a) thermal function f_κ and (b) viscous function f_ν.

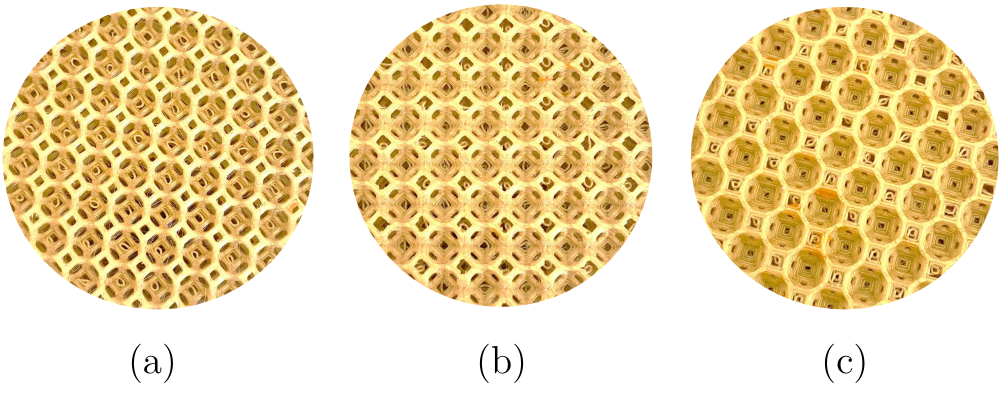

Figure 5.21: Three 3D-Membrane Foams samples: (a) S3, $D_t = 8\ mm$, $\xi = 0.8\ mm$ and $t_0 = 0.6$, (b) S2, $D_t = 8\ mm$, $\xi = 0.8\ mm$ and $t_0 = 0.4$, (c) $D_t = 8\ mm$, $\xi = 0.8\ mm$ and $t_0 = 0.25$.

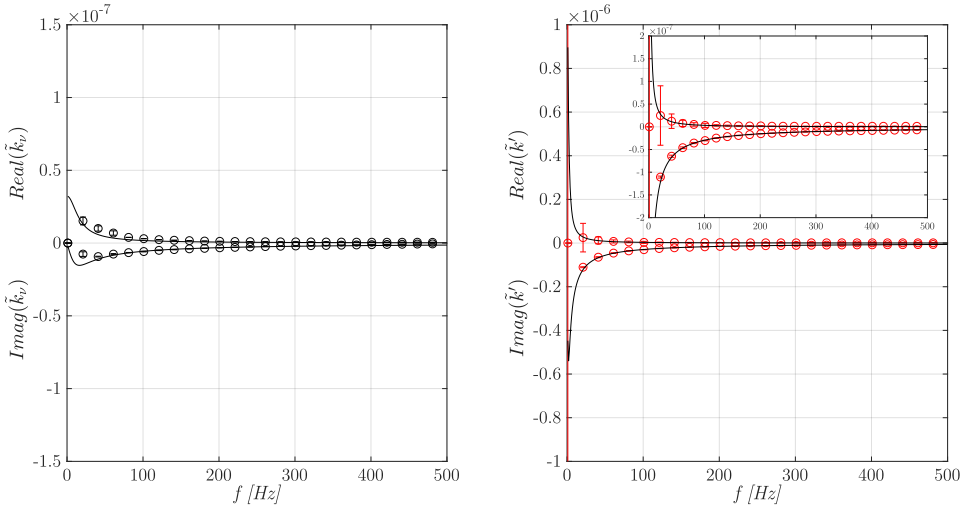

Figure 5.22: 3D-membrane foam S1: Comparison between experimental results (red circular points, mean value $\pm$ standard deviation) and modelling approach (continuous black line). Real and imaginary parts of the frequency-dependent viscous permeability $\tilde{k}_\nu$ (on the left) and thermal permeability $\tilde{k}'$ (on the right).

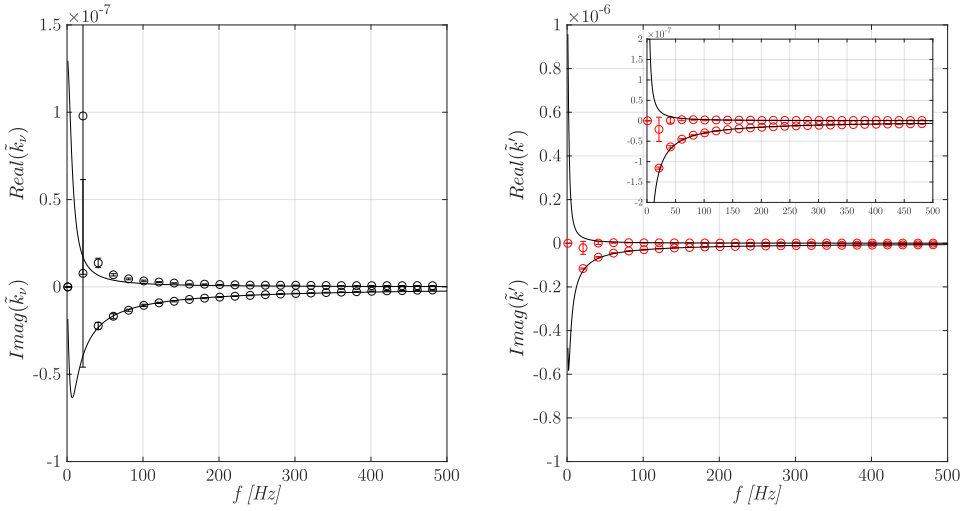

Figure 5.23: 3D-membrane foam S2: Comparison between experimental results (red circular points, mean value $\pm$ standard deviation) and modelling approach (continuous black line). Real and imaginary parts of the frequency-dependent viscous permeability $\tilde{k}_\nu$ (on the left) and thermal permeability $\tilde{k}'$ (on the right).

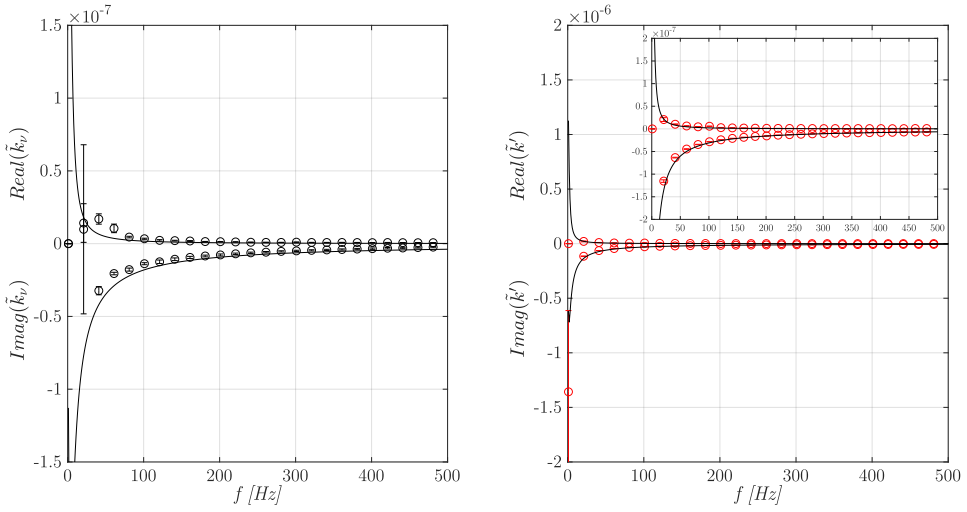

Figure 5.24: 3D-membrane foam S3: Comparison between experimental results (red circular points, mean value $\pm$ standard deviation) and modelling approach (continuous black line). Real and imaginary parts of the frequency-dependent viscous permeability $\tilde{k}_\nu$ (on the left) and thermal permeability $\tilde{k}'$ (on the right).

Chapter 6

Energetic criteria for selecting thermoacoustic stacks

Contents

6.1 Introduction

The interaction between an oscillating flow and the solid skeleton of a porous material gives rise to viscous and thermal power exchanges [15]. This is due to a diffusive process related to the particle velocity and temperature gradients of the oscillating flow which arises near the surface of the solid skeleton. This phenomenon can be used to dissipate sound power or to convert it into heat and *vice versa*. The summation of thermal and viscous losses contributes to sound absorption; it is therefore necessary to ensure that both of them are very high, in the desired frequency range [58]. In the models used to predict the sound absorption coefficient, little attention is usually paid to distinguish how much power is dispersed primarily due to the thermal relaxation process or associated to the viscous nature of the fluid. When small stimuli are applied, the linear and frequency-dependent response function of the porous system is dominated by viscous effects before the viscous characteristic frequency, and by inertia in the high frequency regime [12]. At the same time, for low frequencies the behaviour of the fluid is isothermal while for higher frequencies it tends to become adiabatic. For a medium consisting of pores having uniform cross section, the ratio between the viscous and thermal relaxation frequencies is equal to the Prandtl number. Therefore, for rectilinear and pores of uniform cross section, viscous and thermal losses can be maximized at a given frequency for a value of the characteristic dimension (semi-distance y_0 between the plates and the inner radius r_0 for the circular pores, see Fig. 2.2). Other relations depending on these parameters must be introduced when the geometry is more complex. For more complex geometry structures, the six parameters JCAL model can be used to predict the frequency-dependent behaviour of visco-inertial and thermal exchanges between the frame and saturating fluid [26, 27, 28]. In recent years these devices have attracted the attention of an ever-increasing number of researchers due to the energy crisis and its peculiar characteristics of constructive simplicity and cost-effectiveness [6]. Despite the similarities shared between acoustics and thermoacoustics, these disciplines have evolved somehow independently although one may take advantage of their specific advances. In thermoacoustic devices, a thermal gradient is imposed between the two opposite sides of a porous material by using two heat exchangers. For this reason, thermal exchanges between the fluid and the solid skeleton are increased with respect to the case of a uniform temperature distribution across the material. Regardless the case of a primary motor or reverse machine (heat pump or refrigerator), the goal is to maximize heat exchange and to minimize viscous losses. It is therefore desirable to design the device so that it works at the maximum heat exchange frequency. From what has been said previously it can be highlighted that tortuous pores allow to control this frequency with more degrees of freedom than the only hydraulic radius needed for the straight and uniform pores. The study of thermal and viscous exchanges will be addressed assuming that these effects can be separated. This hypothesis is generally accepted in the framework of small perturbations, and justified when a scale separation between the incident wavelength and the characteristic size of the pores is fulfilled: momentum and energy equations therefore allow describing visco-inertial and heat diffusion effects independently, as highlighted from the homogenization theory [12]. Regarding the thermoacoustic effects, the discussion is however more complex, because of the thermal gradient existing along the direction of propagation of the sound wave inside the material [10]; but this hypothesis can still be preserved as it will be shown in detail below. In this Section, the power exchanges within an air-saturated porous medium subjected to an oscillating flow will be analysed both for uniform cross-sectional materials and complex porous materials. The study will provide the criteria to select the thermoacoustic *stack* to be tested in a thermoacoustic devices. Furthermore, the numerical scheme to simulate the thermoacoustic phenomena which occur inside the porous core will be reported and different typologies of *stacks* will be compared.

6.2 Fluid-structure power exchanges in porous materials

Starting from the general definition of the sound power and considering the hypothesis of lower order viscosity, it is possible to separate the contributions of thermal and viscous powers that a moving fluid exchanges with the solid matrix. The time-averaged sound power $\dot{E}$ across the cross-sectional area of the material can be expressed as:

$$\dot{E} = \frac{\omega}{2\pi} \oint \Re\left[p_1 e^{i\omega t}\right] \Re\left[U_1 e^{i\omega t}\right] dt = \frac{1}{2}\Re\left[\widehat{p_1} U_1\right] = \frac{1}{2}\Re\left[p_1 \widehat{U_1}\right], \tag{6.1}$$

where hat quantities represent the complex conjugate. From the derivation of the time-averaged acoustic power $d\dot{E}$ produced in a length dx, it follows that

$$\frac{d\dot{E}}{dx} = \frac{1}{2}\Re\left[\widehat{p_1}\frac{dU_1}{dx} + \frac{dp_1}{dx}\widehat{U_1}\right]. \tag{6.2}$$

Formally, the pressure variation along x is not affected by the temperature variation, at least directly from Eq. (2.21)

$$\frac{dp_1}{dx} = -\frac{i\omega\rho_m}{1-f_\nu}\frac{U_1}{A_f},$$

In contrast, the variation of U_1 along x is more complex because it depends directly on the thermal gradient and on the oscillatory phenomenon itself, Eq. (2.43) considering also the imperfect isothermal condition of the solid skeleton:

$$\frac{dU_1}{dx} = -\frac{i\omega A_f}{\gamma p_m}\left[1 + (\gamma-1)\frac{f_\kappa}{1+\varepsilon_s}\right] p_1 + \frac{(f_\kappa - f_\nu)}{(1+\varepsilon_s)(1-f_\nu)(1-P_r)}\frac{1}{T_m}\frac{dT_m}{dx}U_1. \tag{6.3}$$

Substituting Eqs. (2.21) and (6.3) into the Eq. (6.2) leads to

$$\frac{d\dot{E}}{dx} = \frac{1}{2}\Re\left[-\frac{i\omega\rho_m}{1-f_\nu}\frac{|U_1|^2}{A_f} - \frac{i\omega A_f}{\gamma p_m}\left[1+(\gamma-1)\frac{f_\kappa}{1+\varepsilon_s}\right]|p_1|^2 + \right.$$
$$\left. + \frac{f_\kappa - f_\nu}{(1+\varepsilon_s)(1-f_\nu)(1-P_r)}\frac{dT_m}{dx}\frac{1}{T_m}U_1\widehat{p_1}\right]. \tag{6.4}$$

At this point the viscous resistance per unit length and the the thermal-relaxation conductance per unit length can be introduced as follow

$$r_\nu = \frac{\omega\rho_m}{A_f}\frac{\Im\left[-f_\nu\right]}{|1-f_\nu|^2}, \tag{6.5a}$$

$$\frac{1}{r_\kappa} = \frac{\gamma-1}{\gamma}\frac{\omega A_f \Im\left[-f_\kappa\right]}{p_m}, \tag{6.5b}$$

It can be easily proved, by combining the above Eqs.(6.5a) and (6.5b) with Eqs. (2.27) and (2.28), that

$$r_\nu = -\Re\left[\frac{Z_\nu}{A_f}\right], \quad \frac{1}{r_\kappa} = -\Re\left[Y_\kappa A_f\right].$$

In fact, the longitudinal complex impedance $Z_\nu dx$, as in Fig. 2.3, is characterized by an inertance and viscous resistance, while the transversal admittance $Y_\kappa dx$ by a compliance and a thermal

relaxation conductance. As in the case of electrical network, inertance and compliance do not take part to the dissipation process of the active power (dissipated power), but only the reactive power. As a consequence the acoustic intensity variation along the material is function of the resistance and conductance part of the impedance and the admittance. Therefore, by substituting Eqs. (6.5a) and (6.5b), together with Eq. (2.46), Eq. (6.4) is written as follow

$$\frac{d\dot{E}}{dx} = -\frac{r_\nu}{2}|U_1|^2 - \frac{1}{2r_\kappa}|p_1|^2 + \frac{1}{2}\Re\left[g\widehat{p_1}U_1\right]. \tag{6.6}$$

From Eq. (6.6), it can be seen how the term g represents the gain (or attenuation) of the acoustic power flowing along the porous material in thermoacoustic devices. In fact, this term g arises only when a non-zero thermal gradient ∇T_m is applied between the two sides of the material. Alternatively, by considering that

$$p_1 = |p_1|e^{i\theta_p}, \quad U_1 = |U_1|e^{i\theta_U}, \quad \Delta\theta = \theta_U - \theta_p,$$

and that

$$p_1\widehat{p_1} = |p_1|^2, \quad T_m\rho_m c_p = \frac{\gamma p_m}{\gamma - 1},$$

Eq. (6.4) can be rearranged and written as

$$\begin{aligned}\frac{d\dot{E}}{dx} = \frac{1}{2}\frac{\omega A_f(\gamma-1)}{\gamma p_m}\left\{-\Im\left[\frac{f_\kappa}{1+\varepsilon_s}\right] + \Gamma\Re\left[e^{i\Delta\theta}\frac{f_\kappa - f_\nu}{(1+\varepsilon_s)(1-f_\nu)(1-P_r)}\right]\right\}|p_1|^2 + \\ - \frac{1}{2}\frac{\omega\rho_m}{A_f}\frac{\Im[-f_\nu]}{|1-f_\nu|^2}|U_1|^2 = \frac{d\dot{E}_\kappa}{dx} + \frac{d\dot{E}_\nu}{dx}.\end{aligned} \tag{6.7}$$

From Eq. (6.7), it is possible to notice that the second term that multiplies $|U_1|^2$ represents the viscous term, $\dot{E}_\nu$, while the first term, the one that multiplies $|p_1|^2$ (named as $\dot{E}_\kappa$), represents the thermal contributions, i.e. represents the power heat exchanged between the fluid and the solid and depends strongly on the Γ parameter. This last parameter accounts for the presence of a thermal gradient along the direction of wave motion, which is necessary to trigger the thermoacoustic phenomenon. $\Gamma = \nabla T_m/\nabla T_{crit}$ is defined as the ratio between the applied thermal gradient (or raised) throughout the porous material and, the critical temperature gradient to trigger the thermoacoustic phenomenon $\nabla T_{crit} = T_m\omega A|p_1|/\rho_m c_p|U_1|$. Tab. 6.1 reports the three possible thermoacoustic cases.

$\Gamma > 1$	$\dot{E}_\kappa > 0$	Thermoacoustic engine
$\Gamma < 1$	$\dot{E}_\kappa < 0$	Thermoacoustic heat pump (or refrigerator)
$\Gamma = 0$	$\dot{E}_\kappa > 0$	Pure dissipation

Table 6.1: Thermal power amount in different cases as a function of the Γ parameter.

6.2.1 Uniform cross-sectional materials

To further elaborate on the potential of Eq. (6.6), the analysis will first focus on to the case of a material consisting of straight pores having a constant cross-section shape, like slits or circular pores (Fig. 2.2). The expressions of the functions f_ν, f_κ are reported in Tab. 2.1 for these pore

shapes. First, the analysis of the viscous and thermal resistances will be carried out inside a single pore. Next, the structure of Eq. (6.6) suggests to investigate to a greater extent how the value of the particle volume velocity and the acoustic pressure, combined with the viscous r_ν and thermal $1/r_\kappa$ resistances together with the ε_s factor and the porosity φ influence the energy conversion inside a porous material.

Viscous losses

Viscous losses depend on the square of the particle volume velocity $|U_1|^2$ (as the kinetic energy), on the angular frequency ω, and on the geometry of the porous material taken into account by means of the f_ν function; see Eqs. (6.5a) and (6.6). To investigate the role of the viscous resistance r_ν, in particular on the viscous losses, we first varied the value of the hydraulic radius $r_h = 1, 0.5, 0.2\ mm$ and tested the evolution of $-\Im\left[f_\nu\right]/|1-f_\nu|^2$ as a function of frequency (Fig. 6.1) for both circular pores ($r_h = r_0$ where r_0 is the pore radius) and slits ($r_h = y_0$, where y_0 is the semi-distance between two contiguous slits). The amplitude of $-\Im\left[f_\nu\right]/|1-f_\nu|^2$ decreases exponentially with frequency until a given frequency, which will be defined here as the viscous power transition frequency, $f_{tp\nu}$ (also reported as vertical line in the Fig. 6.1). For circular pore, $f_{tp\nu} \approx 3\mu/\left(\rho_m r_0^2\right)$; for slit, $f_{tp\nu} \approx 2.2\mu/\left(\rho_m y_0^2\right)$. In particular, the viscous losses due to pore geometry decrease in frequency, as a consequence of the viscous boundary layer decrease with increasing frequency, Eq. 2.18; the decrease being more pronounced before $f_{tp\nu}$ is attained. The product of the angular frequency ω and the function $-\Im\left[f_\nu\right]/|1-f_\nu|^2$ gives as result the viscous resistance r_ν, Eq. (6.5a). In Fig. 6.2 a nonlinear increase of the viscous resistance r_ν as a function of frequency can be observed. Fig. 6.2 also shows the drastic effect that the hydraulic radius r_h of the pores has on the overall value of the viscous resistance r_ν. Although the viscous resistance increased steadily and linearly as the hydraulic radius r_h decreased ($r_h > 0.4\ mm$), the results suggest that the viscous resistance r_ν increases strongly and nonlinearly with the lower studied values of the hydraulic radius r_h ($r_h > 0.4\ mm$). At a given hydraulic radius r_h, the slits display greater viscous resistances (losses) over the whole range of frequencies than the circular pores do. As frequency decreases ($\omega \to 0$), the flow inside the pores tends to be predominantly of the Poiseuille type (purely viscous). In this case, the viscous resistance r_ν tends to be equal to the airflow resistivity σ

$$\lim_{\omega \to 0} r_\nu\left(\omega\right) = \sigma. \tag{6.8}$$

Thermal losses

Thermal losses depend on the square of the sound pressure $|p_1|^2$ (such as the potential energy), on the frequency, as for viscous losses, and on the geometry of the porous material; see Eqs. (6.5b) and (6.6). In this case, the thermal resistance depends only on the imaginary part of the function f_κ, an imaginary part which is negative and characterized by a global minimum. Therefore, a global maximum should be associated to the thermal losses. Plotting $1/\left(r_\kappa \omega\right)$ in Fig. 6.3 as a function of frequency f and hydraulic radius r_h for both circular pores and slits confirms this statement. For a given value of the hydraulic radius r_h, a frequency corresponding to the thermal relaxation frequency $f_{\kappa,\max}$, where the thermal losses are maximized, exists. The maximum depends on the dimensionless parameter r_h/δ_κ, and occurs at the same frequency for circular pores and slits of given hydraulic radius r_h (in general for all pores with uniform cross-sections). For slits, the peak was found numerically to occur at $\max\left[1/\left(r_\kappa\omega\right)\right] \approx 1.1791 \times 10^{-6}\left[1/Pa\right]$ (with $\min\left[\Im\left(f_\kappa\right)\right] \approx -0.4172$), for $r_h/\delta_\kappa = y_0/\delta_\kappa = 1.1311$. For circular pores, $\max\left[1/\left(r_\kappa\omega\right)\right] \approx 1.067 \times 10^{-6}\left[1/Pa\right]$ (with $\min\left[\Im\left(f_\kappa\right)\right] \approx -0.3774$), for $r_h/\delta_\kappa = y_0/\delta_\kappa = 1.7818$. Results reported throughout Figs. 6.2 and 6.3 might be useful to compare the rates of thermal and viscous energies exchanged for the simple pore shapes which have been considered. Whereas the

slits geometry allows for the exchange of more thermal power at a given hydraulic radius than in the circular pores case (Fig. 6.3), the corresponding viscous losses are larger (Fig. 6.2). This is an important point for the design of thermoacoustic devices, which implies a choice of the pore geometry. For a selected geometry, one needs to ensure that an increase in the exchanged thermal power is not lost due to viscous losses. It is noteworthy that for rectilinear and uniform pores the single design variable is the hydraulic radius, while tortuous pores may correspond to more available parameters. We also note that in the analysis reported so far, a classical isothermal boundary condition was assumed at the interface between the fluid and solid ($\varepsilon_s \to 0$), such that the porous material is replaced by a single pore, with the porosity φ acting as a scaling factor. Clearly, the porosity φ corresponds to the fluid volume fraction that will interact with the structure and it is therefore related to the power exchange ratio. Consequently, increasing the porosity allows one to promote power exchanges, but at the expense of the solid volume fraction (thinner solid part). In the limit $\varphi \to 1$, the isothermal boundary condition at the solid skeleton interface may no longer be valid and the ε_s parameter has to be explicitly introduced. To further elaborate on the effect of the ε_s factor, in particular on the heat exchange at fluid-solid interface, the value of the ε_s parameter is varied by considering a specific case in the dilute limit when $\varphi \to 1$. The geometry used for the numerical application consists of solid slits, with $y_0 = 0.3\ mm$, $l = y_0/100$ being the semi-width of the solid part and $\varphi = y_0/(y_0 + l) = 0.99$. In Fig. 6.4.a is reported in black and red dotted lines the $\Im\left[-f_\kappa\right]$ for a perfect isothermal boundary condition and for real case, respectively. Eq. (6.5b) is derived for such a geometry, by taking Celcor as the solid part, a ceramic material whose thermophysical properties at $20°C$ are $c_s = 722\ J/(kg \cdot K)$, $\kappa_s = 2.5\ W/(m \cdot K)$ and $\rho_s = 2510\ kg/m^3$. The effect on the thermal performance can be understood from the fact that when the value of the ε_s parameter differs from zero, the corresponding factor $\Im\left[-f_\kappa/\left(1+\varepsilon_s\right)\right]$ is decreasing. Therefore, a departure from the perfect isothermal boundary condition ($\varepsilon_s \neq 0$) has a negative effect on thermal performance. The spectral quantities of $\Im\left[-f_\kappa/\left(1+\varepsilon_s\right)\right]$ has been computed for two different configurations of the boundary condition at the interface: ideal with $\varepsilon_s = 0$ (black dotted lines) and imperfect with $\varepsilon_s \neq 0$ (red dotted lines); see Fig. 6.4.a. Taking a non-isothermal boundary condition into account instead of the classical isothermal one when $\varepsilon_s \neq 0$ reduces the amplitude of the global minimum in the imaginary part of $\Im\left[-f_\kappa/\left(1+\varepsilon_s\right)\right]$. A more thorough discussion of these aspects would require a particular attention to the absorption of sound, as reported in the next section.

Sound absorption

In classical engineering, sound absorbing materials use a dissipating mechanism based on viscous losses. Thermal losses, however, turn out to be also appropriate. The description of dissipation phenomena introduced throughout Eqs. (6.5a), (6.5b) and (6.6) allows one to identify that viscous and thermal losses depend on the sound field created by a pseudo-standing wave within the material. In particular, the viscous dissipation is related to the particle velocity of air in the porous medium. When backed by rigid and impervious termination, the particle velocity at the face between the material and the rigid backing is always zero, which leads to reduce the particle velocity within the porous material itself. In particular, if the thickness of the material is small (when compared to the wavelength), the losses due to viscous dissipation might be negligible compared to the thermal ones. The amount of absorbed acoustic power by a porous material over a fluid area A_f, is defined in the condition of rigid and impervious back-end surface as

$$\alpha = \frac{\dot{E}_{diss}}{\dot{E}_{inc}}, \tag{6.9}$$

where $\dot{E}_{inc}$ is the incident power over the porous material surface and $\dot{E}_{diss}$ is the dissipated power across the porous material with thickness d

$$\dot{E}_{diss} = \int_0^d \left(\frac{\partial \dot{E}}{\partial x} \right) dx = \int_0^d \left(\frac{\partial \dot{E}_\nu}{\partial x} + \frac{\partial \dot{E}_\kappa}{\partial x} \right) dx = \dot{E}_{diss,visc} + \dot{E}_{diss,therm} \tag{6.10}$$

This coincides with a classical expression, which is possible to obtain with other techniques such as the transfer matrices or the surface impedances methods [58]. Fig. 6.4.b presents the amount of dissipated sound power $\dot{E}$ per unit area of fluid A_f due to viscous $\dot{E}_\nu/A_f$ (continuous line) and thermal $\dot{E}_\kappa/A_f$ (dashed line) effects. For the studied configuration, the dissipated sound power is dominated by thermal effects up to about $900Hz$. The expected value of the maximum dissipated sound power, for each frequency, that could be achieved from thermal effects is shown in dashed-dotted line; a value obtained if $\Im\left[-f_\kappa\right]$ displays its maximum value of 0.41 (Fig. 6.4.a). It is observed that the maximum dissipated power due to thermal effects occurs only at the thermal relaxation frequency $f_{\kappa,\max}$ (Fig. 6.4.b). Note that a variation of this thermal relaxation frequency $f_{\kappa,\max}$ would require a modification of y_0: as y_0 decreases, $f_{\kappa,\max}$ increases ($f_{\kappa,\max} \propto 1/y_0^2$) together with $f_{tp\nu}$. As it can be seen the viscous losses will become larger than the thermal ones at higher frequencies (Fig. 6.4.c). Also shown is the relative percentage of dissipated power due to viscous and thermal interactions with respect to the total dissipated sound power, as presented in Fig. 6.4.c. As the frequency increases, the relative contribution of viscous losses tends to increase and to be predominant with respect to the thermal ones. Finally, Fig. 6.4.d illustrates the value of the sound absorption coefficient $\alpha_{\max}$ that could be obtained if the thermal losses were maximized (dashed line) by setting the imaginary part of the thermal function $\Im\left[-f_\kappa\right]$ to a fixed and maximal amplitude (Fig. 6.4.a). This graph suggests that, if the thermal losses are predominant with respect to the viscous ones, they can be maximized at a given frequency by properly choosing the geometry (in this case y_0). Red curve that merges with the black one shows the absorption coefficient considering the $\varepsilon_s \neq 0$ values. It is slightly smaller but indicates that also thermophysical properties, in theory but little in practice, can affect the sound absorption coefficient.

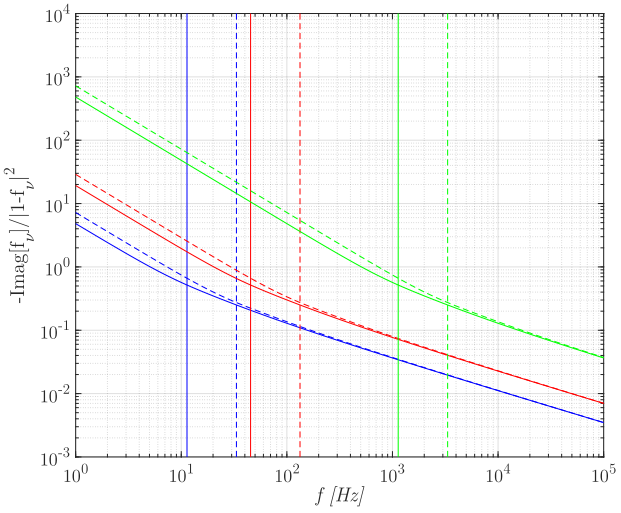

Figure 6.1: Evolution of $\Im\left[f_\nu\right]/|1-f_\nu|^2$ as a function of frequency for three different values of the hydraulic radius $r_h = 1, 0.5, 0.2\ mm$ for circular pores (solid line) and slits (dashed line). Vertical lines correspond to the viscous power transition frequency, $f_{tp\nu}$.

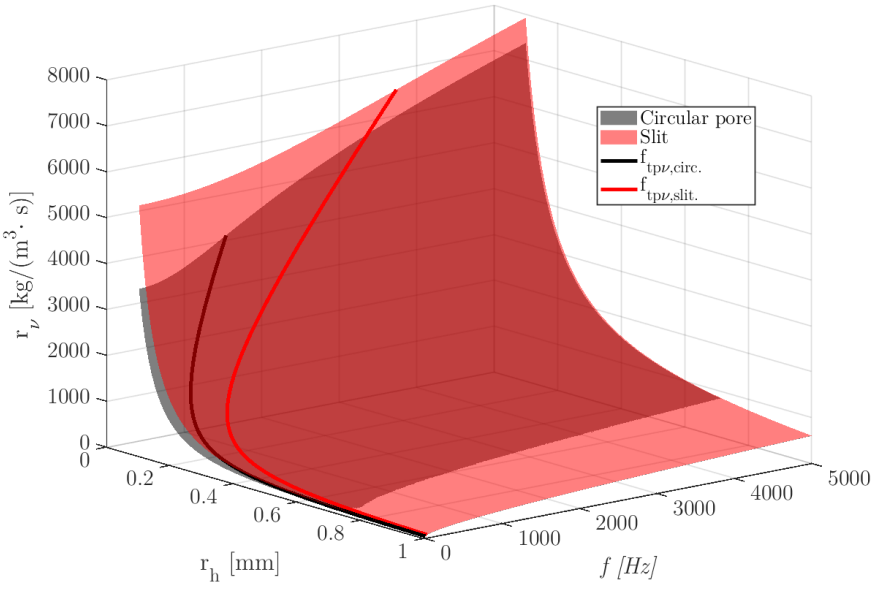

Figure 6.2: Viscous resistance r_ν as a function of frequency f and hydraulic radius r_h for circular pores (grey surface) and slits (red surface). The specific values of the viscous resistance r_ν at the viscous power transition frequencies $f_{tp\nu}$ are also reported within the range of studied hydraulic radii $0.1\ mm < r_h < 1\ mm$.

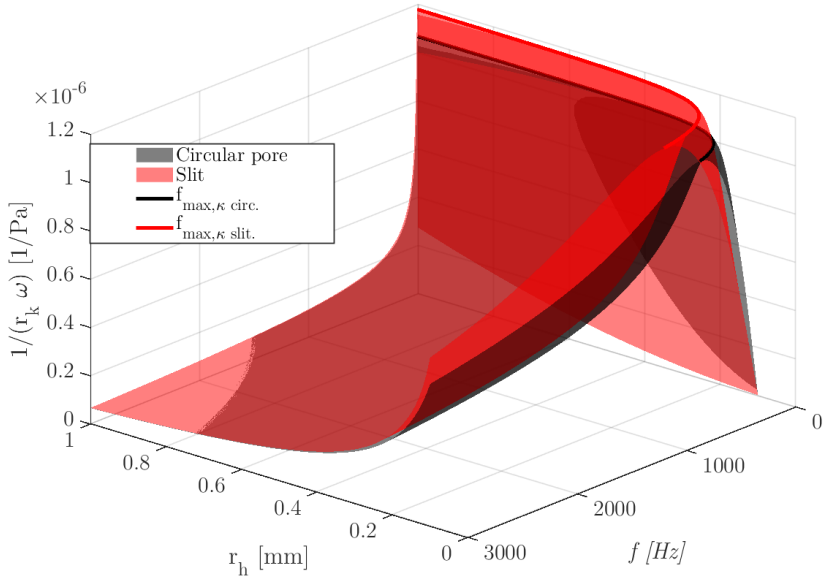

Figure 6.3: $1/\left(r_\kappa \omega\right)$ as a function of frequency f and hydraulic radius r_h for circular pores (grey surface) and slits (red surface). The specific values of $1/\left(r_\kappa \omega\right)$ at the frequencies corresponding to $f_{\kappa,\max}$ are also reported (same colours).

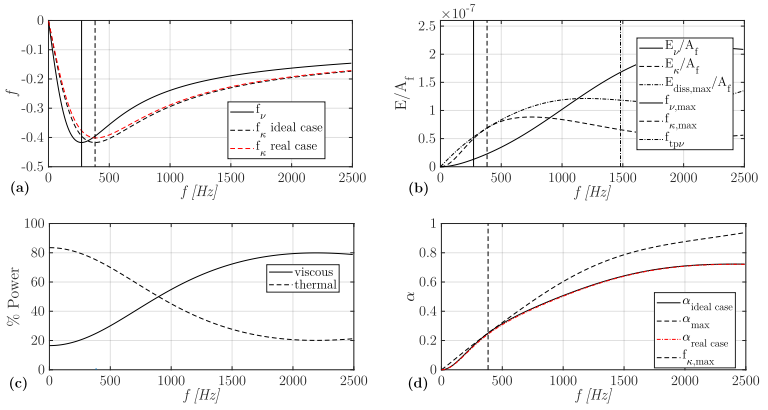

Figure 6.4: a) Imaginary part of f_ν (solid line) and f_κ (dashed line) in the ideal $\varepsilon_s = 0$ (black) and real $\varepsilon_s \neq 0$ (red) cases. b) Viscous $\dot{E}_\nu/A_f$ (solid) and thermal $\dot{E}_\kappa/A_f$ (dashed) powers over a fluid area; the maximum achievable thermal power $\dot{E}_{\kappa,\max}/A_f$ (dashed-dotted) and the related viscous $f_{\nu,\max}$ and thermal $f_{\kappa,\max}$ relaxation frequencies, together with the viscous power transition frequency $f_{tp\nu}$. c) Percentage of dispersed energies due to thermal and viscous effects (the sum is always equal to 100%). d) Absorption coefficient obtained by using Eq. (6.9) in the ideal and real cases, and the maximum absorption coefficient.

6.2.2 Generic porous materials

In the general case of complex tortuous pores, the thermal and viscous functions depend on several parameters. By using the Johnson-Champoux-Allard-Lafarge model to characterize the visco-thermal behaviour of a porous material, six transport parameters are required [26, 27, 28]. It is possible to note from Eq. (3.3) coupled with Eq. (2.19) that f_ν function depends on the static viscous permeability k_0 (or the airflow resistivity, $\sigma = \mu/k_0$), the viscous characteristic length Λ and the high frequency limit of the tortuosity α_∞. Instead, f_κ function depends on two parameters: the static thermal permeability k_0' and the thermal characteristic length Λ'. In the following, the role of these parameters in the responses of the viscous and thermal resistances has been tested. First, a parameter-variation study is performed to investigate the role of these transport parameters, in particular to evaluate if a different pattern of behaviour as that observed for the circular pores and slits could be obtained. Second, because these transport parameters are inter-dependent, and depend *in fine* on the microstructure of the porous material itself, correlations between microstructure and transport parameters available in the literature have been applied to ensure that the potentially interesting configurations identified during the parameter-variation study could be assessed from realistic microstructures.

Viscous losses

First, the viscous resistance r_ν as a function of frequency f and airflow resistivity σ for different values of Λ has been examined and reported as surface plot in Fig. 6.5. From the microstructural point of view, a reduction of Λ at constant σ could be obtained by increasing the cell size of a foam together with the opening ration t_0. The fact that the viscous resistance resistance r_ν increases with frequency and resistivity σ. Fig. 6 can be seen as a book that is leafed through by taking the page for low values of airflow resistivity and high values of frequency. The pages are raised as Λ decreases. A similar image can be obtained by considering the effect of the tortuosity α_∞ instead of the viscous characteristic length Λ (not reported here for the sake of brevity). In the latter case, the pages are raised as the tortuosity α_∞ increases. The consequence is that the viscous resistance

r_ν that might be understood as viscous losses also depends on the viscous characteristic length Λ (or on the tortuosity α_∞), in particular for high values of the frequency f and for low values of the airflow resistivity σ. In other circumstances, r_ν vary relatively little with Λ and α_∞. An easier appreciation of the viscous resistance variation r_ν can be obtained from two-dimensional graphs, by plotting the viscous resistance r_ν as a function of the airflow resistivity σ at a fixed frequency ($f = 500\ Hz$), for different values of the viscous characteristic length $\Lambda = 50\ \mu m$ (green line), $100\ \mu m$ (red line) and $350\ \mu m$ (black line), Fig. 6.6.a. The dependency of viscous resistance r_ν with resistivity σ can be described by a linear behaviour (dotted line) is the airflow resistivity display a value greater than a specific resistivity, $\sigma \geq \sigma_s$ (r_ν becomes independent of Λ):

$$\sigma_s \approx \sqrt{f} e^C, \tag{6.11}$$

where C is a constant that depends on both Λ and α_∞ as

$$C = 0.531\Lambda^{-0.2359} + 1.44\alpha_\infty^{0.513} \tag{6.12}$$

In Fig. 6.6.b, the resistivity σ of the porous material has been varied (specifically 5000, 20000, and $50000\ Pa \cdot s/m^2$), while the viscous characteristic length Λ has been modified for each previously determined resistivity; namely 50 (green line), 100 (red line), and 350 (black line) μm. Increasing the airflow resistivity σ significantly decreases the influence of the viscous characteristic length Λ. Therefore, the consequence of this statement is that for a constant and low resistivity value σ ($5000\ Pa \cdot s/m^2$), decreasing the viscous characteristic length Λ ($50\ \mu m$) corresponds to a significant increase of the viscous resistance r_ν (i.e. the viscous losses). The latter values of the viscous resistance r_ν can be even higher than for porous materials with much larger airflow resistivity σ while the viscous length Λ is increased ($\sigma = 20000\ Pa \cdot s/m^2$; $\Lambda = 100$ or $350\ \mu m$; $f \geq 0.5\ kHz$). Also displayed in the results reported in Fig. 6.6.b is that for high values of Λ ($350\ \mu m$ in this example), r_ν varied relatively little with frequency and was approximately equal to the quasi-static σ value (dashed horizontal lines), as from Eq. (6.8).

Thermal losses

The way in which the thermal losses vary with Λ' and k_0' is very complex. Fig. 6.7 reports $1/r_\kappa$ as a function of frequency and static thermal permeability for three different values of the thermal characteristic length. To better understand the meaning of Fig. 6.7 one can image to cut this figure with three different k_0' values as shown in Fig. 6.8. Fig. 6.8.a highlights that, for low k_0' values, the thermal losses are not influenced by Λ'. For intermediate values (Fig. 6.8.b) they increase as Λ' increases for almost the entire frequency range. For large values of k_0' (Fig. 6.8.c) the trend is reversed. It can be observed that for low frequencies, the behaviour is like the case of that in Fig. 6.8.b, while for the high frequencies low value of Λ' implies a large thermal loss. In the following a discussion on the trend of the maximums of $1/r_\kappa$ is reported. Fig. 6.9.a reports how the frequency at which the maximum of $1/r_\kappa$ is obtained, compared to the dimensionless frequency ω/ω_κ, varies as a function of a parameter M', defined in Eq. (3.11b). Fig. 6.9.b reports the maximum values of $\Im\left[-f_\kappa\right]$) versus the same M' parameters. These trends can be described by the following functions

$$\frac{\omega}{\omega_\kappa} = \begin{cases} 0.04M'^2 - 0.22M' + 1 & M' < 6 \\ 0.716M' - 3.176 & M' \geq 6 \end{cases} \tag{6.13}$$

$$\max(-\Im\left[f_\kappa\right]) = 0.3e^{-0.3752M'} + 0.2 \tag{6.14}$$

The meaning of Eqs. (6.13) and (6.14), reported in Fig. 6.9, are not intuitive and can be explained graphically, as shown in Fig. 6.10. It is possible to see that the frequency at which the maximum

of $1/r_\kappa$ is obtained decreases almost linearly with the increase of k_0' (Fig. 6.10.a), at least up to a limit value of k_0' which can be identified by the limit condition $M' = 6$ once φ and Λ' have been assigned. In this case, for simplicity, it has been assumed that $\varphi = 1$. At the same time, Fig. 6.10.b shows that also the maximum value of the function $\Im\left[-f_\kappa\right]$ decrease as k_0' increase, and therefore the maximum thermal power the fluid can exchange with the solid skeleton. Fig. 6.10.b highlights that, in general, to increase thermal exchange it is important to assure porous material characterized by a very large Λ' value. As far as the design of a thermoacoustic device is concerned, the results shown in Fig. 6.10 are of great importance for several reasons. The first certainly because it shows that the maximum value of $\Im\left[-f_\kappa\right]$ can be greater than that achieved in rectilinear and uniform pores. Furthermore, it makes clear that the frequency at which the maximum of $1/r_\kappa$ is obtained and the maximum value can be controlled with two different parameters, at least until $M' < 6$ reported with a dotted vertical line in the case of $\Lambda' = 100\ \mu m$. The case where $M' \geq 6$ is not very interesting because it is characterized by very low of $\max(\Im\left[-f_\kappa\right])$. In any case, the maximum thermal exchange is achieved for low values of k_0' and large values of Λ'. The results reported in Fig. 6.10, combined with those of Fig. 6.5, allow to make important considerations in the design of a tortuous porous material as a stack in a thermoacoustic engine. If the goal is to maximize the heat exchange, it is necessary to follow the recommendations set out above, that is design the porous material to have a very large Λ' value, but at the same time a very low value of k_0', see Fig. 6.10.b. Note that, from Fig. 6.10.a, the last condition implies working at too high frequency. But at high frequency, the losses of a viscous nature, (see Fig. 6.5), increase significantly and could completely delete the gain of thermal power. At the same time the less the frequency, viscous losses would decrease but the less is the maxima of the $\Im\left[-f_\kappa\right]$ function and therefore the heat exchange. Therefore, the only parameter to be act on is Λ', whatever the operating frequency of the device, and make sure that it is as high as possible.

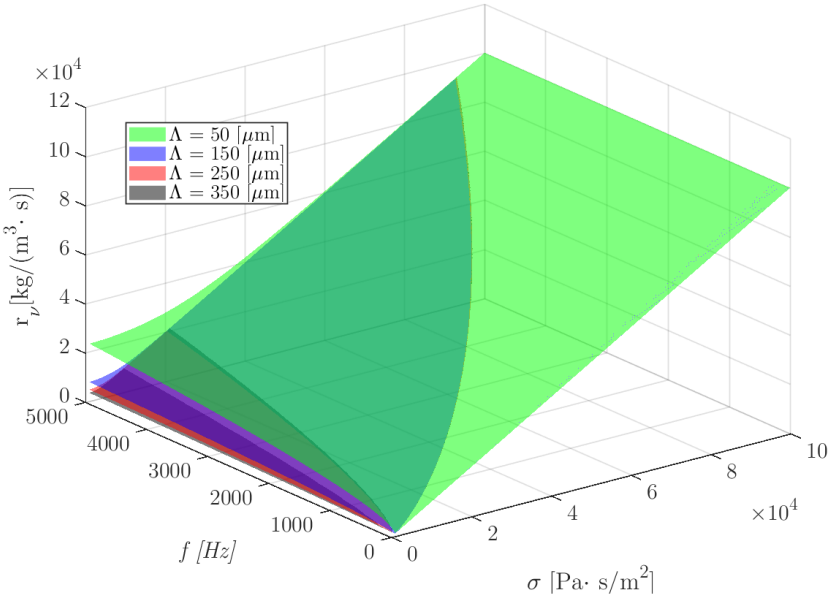

Figure 6.5: The viscous resistance r_ν as a function of the airflow resistivity σ and frequency f for three different values of the viscous characteristic length Λ.

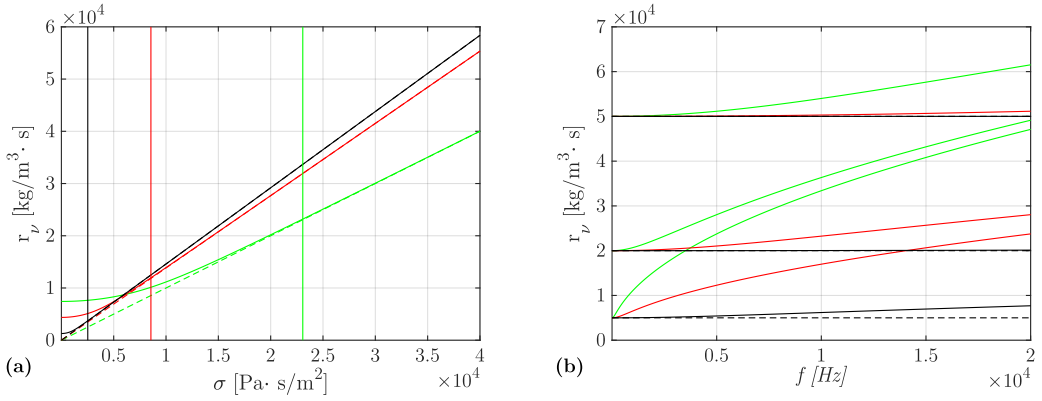

Figure 6.6: (a) Viscous resistance r_ν as a function of resistivity σ at fixed frequency $f = 500\ Hz$ for three different values of Λ [50 μm (green line), 100 μm (red line) and 350 μm (black line)]. The vertical lines represent the specific values of σ $\sigma \geq \sigma_s$ after which a linear behaviour is observed. (b) Viscous resistance r_ν as a function of frequency f for three different values of σ: 5000, 20000 and 50000 $Pa{\cdot}s/m^2$; with low frequency limit of r_ν equal to σ (Eq. 6.8) [$\Lambda = 50\ \mu m$ (green line), $\Lambda = 100\ \mu m$ (red line) and $\Lambda = 350\ \mu m$ (black line)].

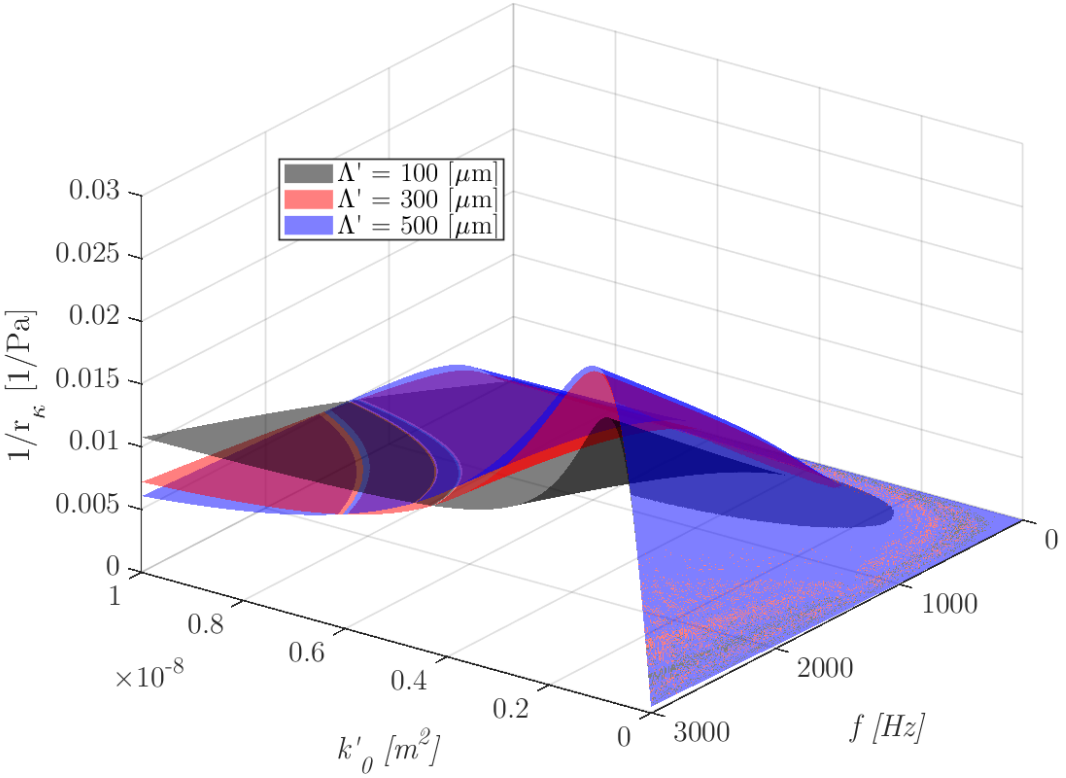

Figure 6.7: $1/r_\kappa$ vs k_0' and frequency for three values of Λ'.

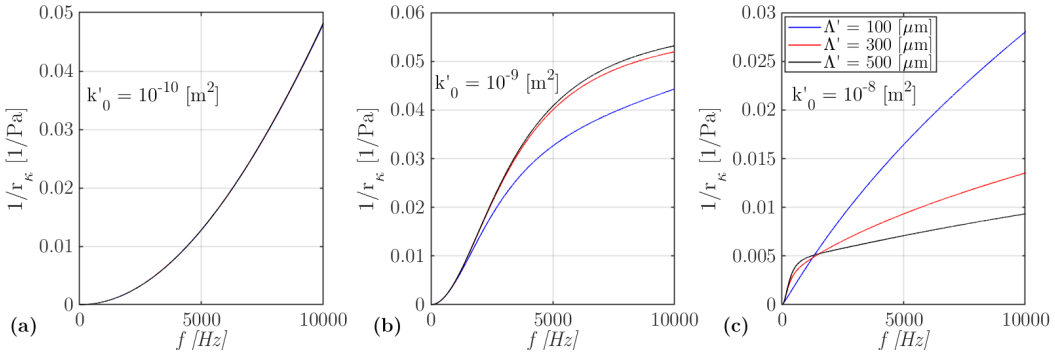

Figure 6.8: $1/r_\kappa$ vs frequency for three values of Λ' and three different values of k_0': (a) $10^{-10}\ m^2$, (b) $10^{-9}\ m^2$ and c) $10^{-8}\ m^2$.

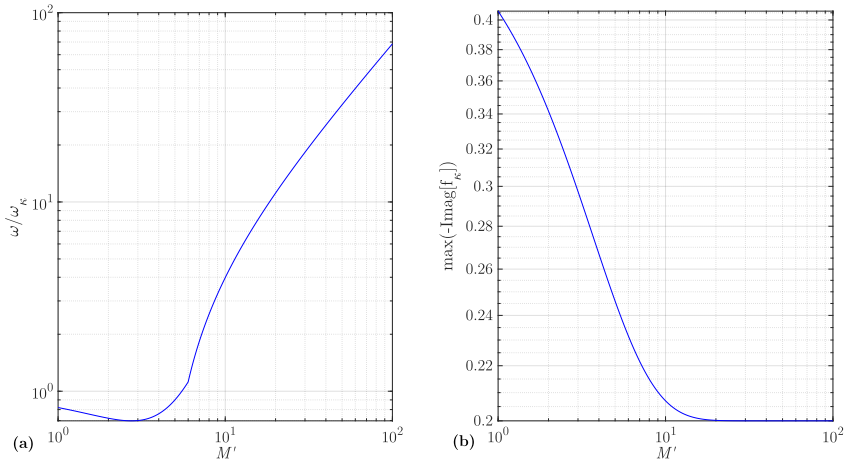

Figure 6.9: (a) maximum frequency of $1/r_\kappa$, compared to the frequency $\omega_{\max}/\omega_\kappa$, vs M' parameter; (b) maximum values of $\Im\left[-f_\kappa\right]$ vs M'.

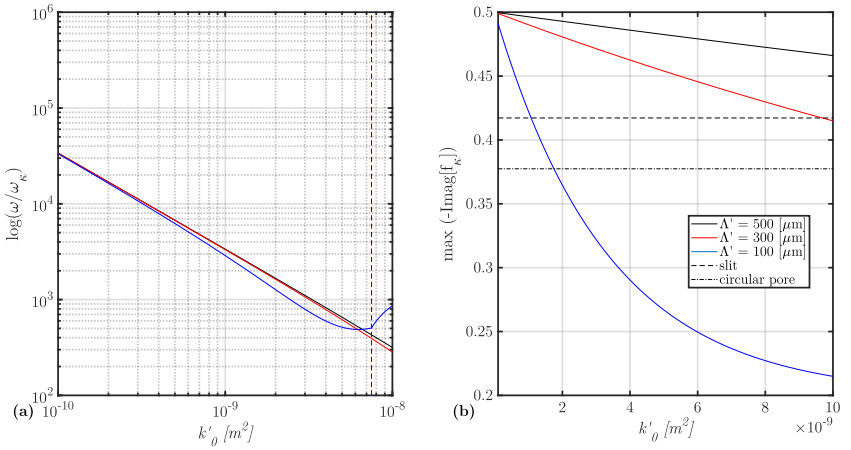

Figure 6.10: (a) $\omega_{\max}$ vs k_0', dotted-vertical line reports the case of $M' = 6$; (b) $\max(-\Im\left[f_\kappa\right])$ vs k_0'. All the curves are plotted in the hypothesis of $\varphi = 1$.

6.3 Total power

Fig. 6.11 introduces the topic of total power, indicated as $\dot{H}$, showing two typical control volumes of interest in thermoacoustics. Consider the thermoacoustic refrigerator shown in Fig. 6.11.a and 6.11.b, driven by a loudspeaker (or a piston) at the left and having thermal insulation around everything except the heat exchangers, so that heat can be exchanged with the outside world only at the two heat exchangers, and work can be exchanged with the outside world only at the piston. The principle of energy conservation can be applied to the control volume shown by the dotted line in Fig. 6.11. In steady state, time-averaged over an integral number of acoustic cycles, the energy inside the control volume cannot change, so the rate at which energy flows into that control volume must equal the rate at which energy flows out. What flows in is clearly the time-averaged mechanical power (which is exactly equal to the acoustic power flowing from the face of the loudspeaker into the gas). That must equal the sum of the two outflowing powers, labelled heat power and total power. Another typical important control volume is shown in Fig. 6.11.b, intersecting a stack or regenerator in two places, with thermal insulation around the immovable side walls. Here the only powers flowing are the total powers in and out of the two end surfaces of the control volume. Applying the principle of energy conservation (again, steady state and time averaged) to this control volume shows that total power in equals total power out. So total power cannot depend on x within a stack or regenerator (it has to be constant, independent of x). Rott's acoustic approximation to the total power flux in the x direction, time averaged and integrated over the cross-sectional area A of the channel, can then be written as

$$\dot{H} = \frac{1}{2}\rho_m \int \Re\left[h_1 \widehat{u_1}\right] dA - \dot{Q}_\kappa, \tag{6.15}$$

where $\dot{Q}_\kappa$ is the heat flowing via conduction through a solid. Said κ_{eq} the *equivalent* thermal conductivity of the porous material and $\dot{Q}_\kappa$ can be expressed in a general form as

$$\dot{Q}_\kappa = \kappa_{eq} A \nabla T_m = \kappa_{eq} A \frac{dT_m}{dx}. \tag{6.16}$$

where A is the overall cross-sectional area. For an ideal gas, it is true that

$$h_1 = c_p T_1 \tag{6.17}$$

By substituting Eqs. (6.17) and (6.16) in Eq. (6.15), it follows that

$$\dot{H} = \frac{1}{2}\rho_m c_p \int \Re\left[T_1 \widehat{u_1}\right] dA - \kappa_{eq} A \frac{dT_m}{dx}. \tag{6.18}$$

Using Eqs. (2.51) and (2.14) for respectively T_1 and u_1 and, performing the integration in Eq. (6.18) yields

$$\dot{H} = \frac{1}{2}\Re\left[p_1 \widehat{U_1}\left(1 - \frac{f_\kappa - \widehat{f_\nu}}{(1+P_r)\left(1-\widehat{f_\nu}\right)(1+\varepsilon_s)}\right)\right] + \\ + \frac{\rho_m c_p |U_1|^2}{2A\omega\,(1-P_r)\,|1-f_\nu|^2}\Im\left[\widehat{f_\nu} + \frac{\left(f_\kappa - \widehat{f_\nu}\right)\left(1+\varepsilon_s\frac{f_\nu}{f_\kappa}\right)}{(1+\varepsilon_s)\,(1+P_r)}\right]\frac{dT_m}{dx} - \kappa_{eq}\frac{dT_m}{dx}A. \tag{6.19}$$

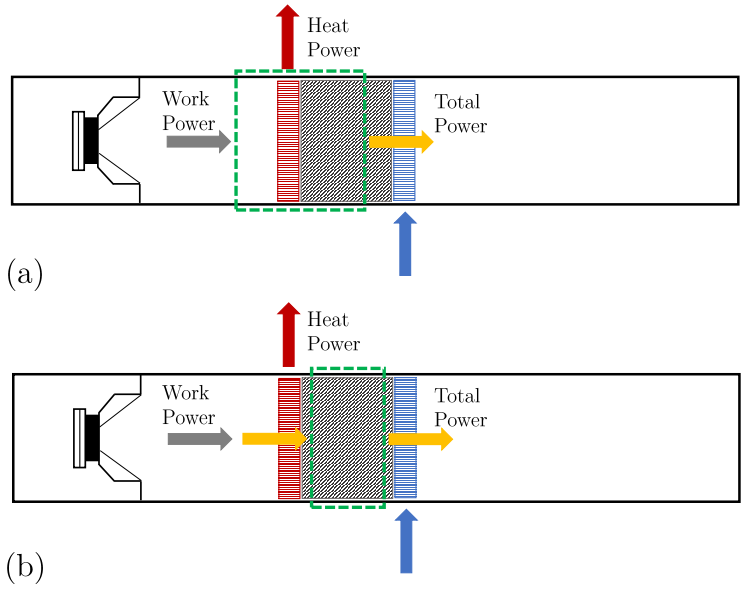

Figure 6.11: A standing-wave refrigerator, insulated everywhere except at the heat exchangers. (a) One useful control volume for thermoacoustics, enclosing the left end. (b) Another useful control volume, enclosing part of the stack.

6.3.1 Thermal conductivity models for stacks

To assess the heat flowing via conduction through the porous stack, it is fundamental to correctly estimate the value of the *equivalent* thermal conductivity κ_{eq}, as reported in Eq. (6.16). Swift [6] evaluates $\dot{Q}_\kappa$ as

$$\dot{Q}_\kappa = -\left(\kappa A_f + \kappa_s A_s\right) \frac{dT_m}{dx} = -\left(\varphi\kappa + (1-\varphi)\,\kappa_s\right) \frac{dT_m}{dx}. \tag{6.20}$$

Eq. (6.20) can be considered valid for uniform cross-sectional material, such as parallel plates, circular pores and longitudinal pin arrays, where heat flows in parallel between fluid and solid. For porous materials with a random solid skeleton distribution a more generic formulation, as reported in Eq. (6.16), should be used. κ_{eq} is the *equivalent* thermal conductivity of the porous medium and it depends both on fluid and solid thermal conductivity, the porosity and a geometrical factor which represents the solid distribution over the fluid in the porous material. Therefore, to complete the description of the complex porous material to be used as thermoacoustic stack, an analytical formulation of the *equivalent* thermal conductivity κ_{eq} is needed to correctly assess the conductive heat power $\dot{Q}_\kappa$. For several porous materials, such as Wire Mesh, models for assess the *equivalent* thermal conductivity are available in literature [91]. When there is a lack of analytical formulation in literature, numerical simulation based on *Finite Element Method* can be used to evaluate this parameter κ_{eq}.

Tetragonal Pin Array

Generally, fibers networks are composed by a large number of struts statistically oriented in the space, while pin array stack is characterized by a precise controlled geometry. Therefore, the aim is to have a thermal conductivity model particularized for the tetragonal with square base pin array depending on the pins 'orientation. The two-limit cases for the thermal conductivity are

represented by the longitudinal κ_L (Fig. 4.1.a) and the transversal κ_T pin array (Fig. 4.1.b), which analytical description are available

$$\kappa_L = \varphi\kappa + (1-\varphi)\,\kappa_s, \tag{6.21a}$$

$$\kappa_T = \left(\frac{\varphi}{\kappa} + \frac{1-\varphi}{\kappa_s}\right)^{-1}. \tag{6.21b}$$

An analytical model for thermal conductivity of tetragonal pin array is developed as weighted average between κ_L and κ_T as [92]

$$\kappa_{eq,TBC} = \Omega_{zz}\kappa_L + (1-\Omega_{zz})\,\kappa_T, \tag{6.22}$$

where $\Omega_{zz} = L_z^2/(L_x^2 + L_z^2)$ is the geometrical parameter indicating the orientation of the pin array to respect the thermal gradient direction. Since the parallel and transversal formulations of conductivity depend on the porosity φ, assessed through formulation provided by Di Giulio *et al.* [67] (Eq. (4.3) with the constant in Tab. 4.1), the proposed relation, Eq. (6.22), for the *equivalent* thermal conductivity is function only of the geometrical parameters of the unit cell $\left(L_x, L_z, r_p\right)$. Finite Element simulations have been carried out on the Representative Elementary Volume of the Tetragonal pin array porous material to verify the previous analytical expression of the effective thermal conductivity κ_{eq}. In Fig. 6.12.a., the fluid and solid volume fractions, respectively V_f and V_s, in which the thermal problem is solved, are shown. A temperature gradient is applied on the unit cell ($T = T_{up}$ on Ω_{up} and $T = T_{down}$ on Ω_{down}, first type Dirichlet's boundary conditions), while symmetry boundary conditions are imposed on the lateral boundaries ($\nabla T \cdot n = 0$) to reproduce the periodicity of the elementary volume. Based on these assumptions, the effective thermal conductivity can be assessed by picking up the volume average heat flux $\dot{q}_x\ \left[W/m^2\right]$ value along the thermal gradient $\left(\nabla T = T_{down} - T_{up}\right)$ direction

$$\kappa_{\text{FEM}} = -\frac{\dot{q}_x}{\nabla T} = -\frac{\dot{q}_x}{T_{down} - T_{up}} L_z. \tag{6.23}$$

In Fig. 6.12.b, the thermal field inside the unit cell is reported. The comparison between the predictive model, Eq. (6.22), and FEM results is reported in Fig. 6.13 for three different values of $\bar{L}_z = 10.5, 13.9, 17.3$.

Wire Mesh

For Wire Mesh, an extensive review of the *equivalent* thermal conductivity is reported in the work of Li and Peterson [91] In a first approach, the relation proposed by Alexander [93] is adopted

$$\kappa_{eq,WM} = \kappa \left(\frac{\kappa_s}{\kappa}\right)^{(1-\varphi)^{0.59}}. \tag{6.24}$$

3D-membrane foams

As for the Tetragonal Pin Array, Finite Element based simulations have been carried out in order to find a predictive correlation between microstructural parameters ξ, D_t and t_0 and the *effective* thermal conductivity of these structures. As for the case of Tetragonal Pin Array, for every typology of material κ_L and κ_T, Eqs. (6.21a) and (6.21b), represent the upper case (fluid and solid in parallel) and the lower case (fluid and solid in series) in the evaluation of the *effective* thermal conductivity. Therefore, by following the same logic above, Eq. (6.23), the *equivalent* thermal conductivity $\kappa_{eq,\text{MF}}$ formulation can be written as

$$\kappa_{eq,\mathrm{MF}} = 0.2203\kappa_L + (1 - 0.2203)\kappa_T, \tag{6.25}$$

where the correlation coefficient equal to 0.2203 guarantees a value of Adjusted R-square equal to 0.8438 and a low Sum of Squares Error fixed to 0.002624. The comparison between the fitting curve and the FEM results can be appreciated in Fig. 6.14.a, while in Fig. 6.14.b residual plot is reported.

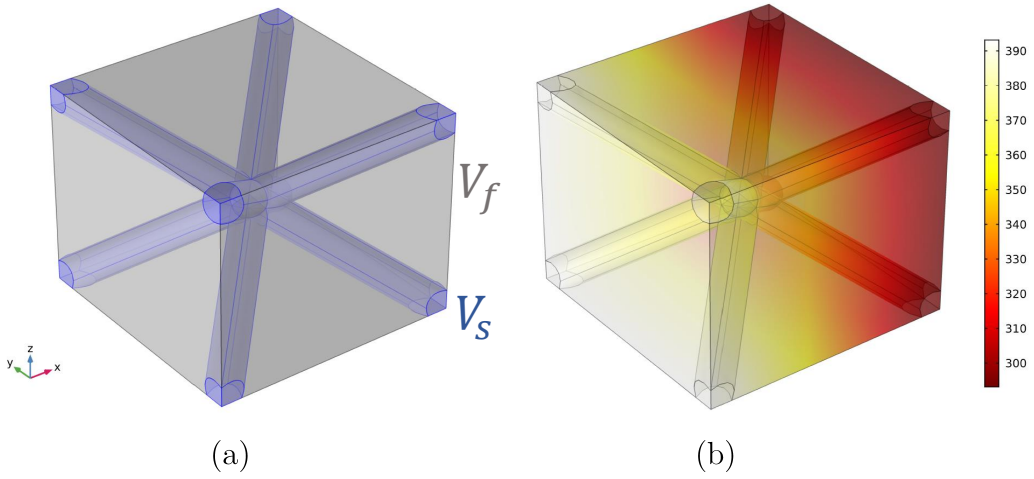

Figure 6.12: (a) Fluid and solid volume fractions. (b) The thermal field inside the unit cell ($T_{up} = 293\ K$ and $T_{down} = 393\ K$).

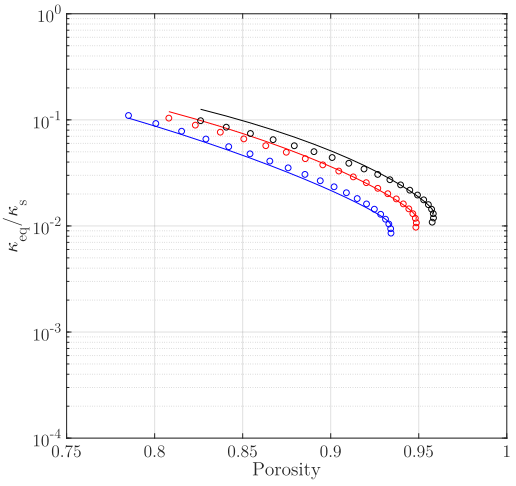

Figure 6.13: Comparison between FEM results (point) and predictive model (continuous line) of dimensionless *equivalent* thermal conductivity κ_{eq}/κ_s versus porosity φ $\left(\kappa/\kappa_s = 1.091e-4\right)$. In black, $\bar{L}_z = 17.3$. In red, $\bar{L}_z = 19.3$. In blue, $\bar{L}_z = 10.5$.

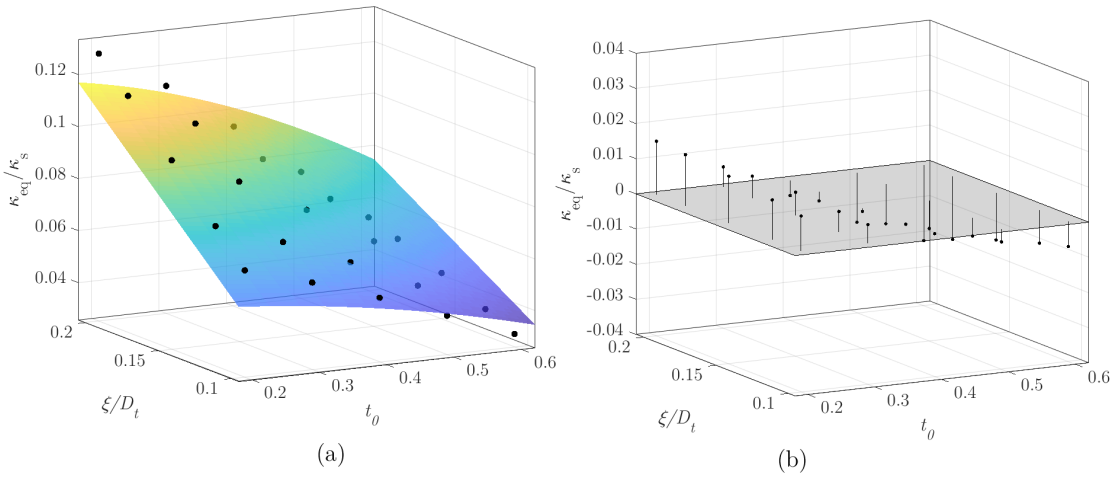

Figure 6.14: (a) Comparison the fitting curve and the FEM results (black point) for the dimensionless *equivalent* thermal conductivity $\kappa_{eq,\mathrm{MF}}/\kappa_s$. (b) residual plot of the correlation over the FEM results.

6.4 Simulation of thermoacoustic devices

To have a preliminary evaluation of the different stacks performance, numerical simulations are carried out on a standing wave thermoacoustic engine. Solving the thermoacoustic fields inside the stacks means to know the distribution of acoustic pressure $p_1(x)$, volume velocity $U_1(x)$ and static temperature $T_m(x)$ along the device. In particular, it is necessary to solve the system composed by Eqs. (2.21), (6.3) and (6.19)

$$\frac{dp_1}{dx} = -\frac{i\omega\rho_m}{1-f_\nu}\frac{U_1}{A_f},$$

$$\frac{dU_1}{dx} = -\frac{i\omega A_f}{\gamma p_m}\left[1+(\gamma-1)\frac{f_\kappa}{1+\varepsilon_s}\right]p_1 + \frac{(f_\kappa-f_\nu)}{(1+\varepsilon_s)(1-f_\nu)(1-P_r)}\frac{1}{T_m}\frac{dT_m}{dx}U_1,$$

$$\frac{dT_m}{dx} = \frac{\dot{H} - \frac{1}{2}\Re\left[p_1\widehat{U_1}\left(1-\frac{f_\kappa-\widehat{f_\nu}}{(1+P_r)\left(1-\widehat{f_\nu}\right)(1+\varepsilon_s)}\right)\right]}{\frac{\rho_m c_p|U_1|^2}{2A\omega(1-P_r)|1-f_\nu|^2}\Im\left[\widehat{f_\nu}+\frac{\left(f_\kappa-\widehat{f_\nu}\right)\left(1+\varepsilon_s\frac{f_\nu}{f_\kappa}\right)}{(1+\varepsilon_s)(1+P_r)}\right]-\kappa_{eq}A}.$$

The free software for the numerical simulations of thermoacoustic devices is DeltaEC [78]. However, it does not contemplate the use of complex porous material as stack, but only the uniform cross-sectional materials. Therefore, a MATLAB code, which works in a similar manner as DeltaEC, has been realized to take into account the new functions f_ν and f_κ given by the JCAL model coupled with the transport parameters correlations for each selected material [18]. In particular, in order to focus the attention only on the stack performance, the other components relative to the standing wave device such as the hot and cold duct and the hot and cold heat exchanger are not taken into account in the remainder of this discussion. Even if their characteristics affect the results of this analysis, their influence is almost the same regardless of the type of stack used. It is supposed that the standing wave can propagate in an *ideal* hot duct of length L_{hot} without losses, then entering in an *ideal* hot heat exchanger where it receives heat power $\dot{Q}_{\mathrm{hot}}$ equals to the total power $\dot{H}$ conserved into the stack (Fig. 6.15).

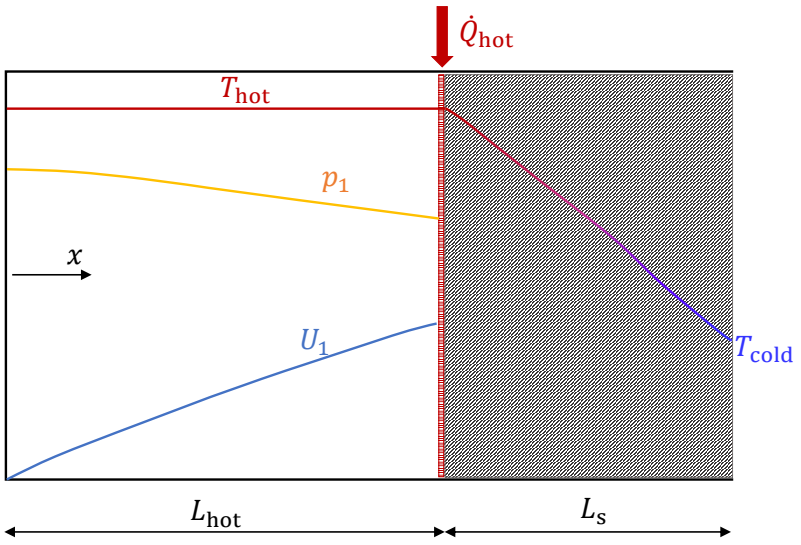

Figure 6.15: Sketch of a device used to numerically analyse the thermoacoustic performance of a stack.

6.4.1 Numerical procedure

Therefore, assuming a pure standing wave inside the device the boundary conditions to be fixed are: the acoustic pressure at $x = 0$ coordinate, named p_{run}, the hot and cold temperature between the two side of the stack, respectively T_{hot} and T_{cold} and the input heat power $\dot{Q}_{\text{hot}}$. From these hypotheses, the acoustic pressure, volume velocity and static temperature at the hot section of the stack can be assessed as

$$p_{1,x=L_{\text{hot}}} = p_s = \frac{1}{2}\left(e^{ik_A L_{\text{hot}}} + e^{ik_A L_{\text{hot}}}\right) p_{run}, \tag{6.26}$$

$$U_{1,x=L_{\text{hot}}} = U_s = \frac{1}{2}\frac{\left(e^{ik_A L_{\text{hot}}} - e^{ik_A L_{\text{hot}}}\right)}{\rho_m c} p_{run}, \tag{6.27}$$

$$T_{m,x=L_{\text{hot}}} = T_{\text{hot}}. \tag{6.28}$$

The fluid parameters, such as the air wavenumber k_A, the sound speed c and the density ρ_m, are all functions of the temperature and they must be assessed at the temperature T_{hot}. To solve the above differential equations system, the 1D-*Finite Differences* numerical scheme is adopted together with an iterative procedure. The stack is divided in N slices of length Δx, therefore Eqs. (2.21), (6.3) and (6.19) are discretized as follow

$$\frac{p_1^{i+1} - p_1^i}{\Delta x} = -\frac{i\omega\rho_m}{(1 - f_\nu) A_f}\frac{U_1^{i+1} + U_1^i}{2}, \tag{6.29}$$

$$\frac{U_1^{i+1} - U_1^i}{\Delta x} = \frac{i\omega A_f}{\gamma p_m}\left(1 + (\gamma - 1)\frac{f_\kappa}{1 + \varepsilon_s}\right)\frac{p_1^{i+1} + p_1^i}{2} + \\ + \frac{f_\kappa - f_\nu}{(1 - f_\nu)(1 - P_r)(1 + \varepsilon_s)}\frac{T_m^{i+1} - T_m^i}{\Delta x}\frac{U_1^{i+1} + U_1^i}{2}, \tag{6.30}$$

$$\frac{T_m^{i+1}-T_m^i}{\Delta x}=\frac{\dot{H}-\frac{1}{2}\Re\left[\frac{p_1^{i+1}+p_1^i}{2}\widehat{\frac{U_1^{i+1}+U_1^i}{2}}\left(1-\frac{f_\kappa-\widehat{f_\nu}}{\left(1-\widehat{f_\nu}\right)(1+P_r)(1+\varepsilon_s)}\right)\right]}{\frac{\rho_m c_p\left|\frac{U_1^{i+1}+U_1^i}{2}\right|^2}{2\omega A_f(1-P_r)|1-f_\nu|^2}\Im\left[\widehat{f_\nu}+\frac{\left(f_\kappa-\widehat{f_\nu}\right)\left(1+\varepsilon_s\frac{f_\nu}{f_\kappa}\right)}{(1+\varepsilon_s)(1+P_r)}\right]-\kappa_{eq}A}. \tag{6.31}$$

Eqs. (6.29) and (6.30) can be rewritten solving for the $i+1$ element as

$$p_1^{i+1}=p_1^i+C_1\frac{U_1^{i+1}+U_1^i}{2}\Delta x, \tag{6.32}$$

$$U_1^{i+1}=\frac{\left(2+C_3\Delta x+\frac{C_1C_3\Delta x^2}{2}\right)U_1^i+2C_2\Delta x p_1^i}{2-\frac{C_1C_2\Delta x^2}{2}-C_3\Delta x}, \tag{6.33}$$

$$T_m^{i+1}=T_m^i+\frac{\dot{H}-\frac{1}{2}\Re\left[\frac{p_1^{i+1}-p_1^i}{2}\widehat{\frac{U_1^{i+1}-U_1^i}{2}}\left(1-\frac{f_\kappa-\widehat{f_\nu}}{\left(1-\widehat{f_\nu}\right)(1+P_r)(1+\varepsilon_s)}\right)\right]}{\frac{\rho_m c_p\left|\frac{U_1^{i+1}+U_1^i}{2}\right|^2}{2\omega A_f(1-P_r)|1-f_\nu|^2}\Im\left[\widehat{f_\nu}+\frac{\left(f_\kappa-\widehat{f_\nu}\right)\left(1+\varepsilon_s\frac{f_\nu}{f_\kappa}\right)}{(1+\varepsilon_s)(1+P_r)}\right]-\kappa_{eq}A}\Delta x. \tag{6.34}$$

Where

$$C_1=-\frac{i\omega\rho_m}{(1-f_\nu)A_f}, \tag{6.35a}$$

$$C_2=\frac{i\omega A_f}{\gamma p_m}\left(1+(\gamma-1)\frac{f_\kappa}{1+\varepsilon_s}\right), \tag{6.35b}$$

$$C_3=\frac{f_\kappa-f_\nu}{(1-f_\nu)(1-P_r)(1+\varepsilon_s)}\frac{T_m^{i+1}-T_m^i}{\Delta x}, \tag{6.35c}$$

are functions of the static temperature in each slice, assessed as the mean value between T_m^i and T_m^{i+1}

$$C_1,C_2,C_3=f\left(\frac{T_m^{i+1}+T_m^i}{2}\right).$$

Here, the procedure starts by fixing the first iterative value

$$T_{m,\mathrm{I}}^{i+1}=T_m^i,$$

and then from Eqs. (6.32) and (6.33), p_1^{i+1} and U_1^{i+1} are found. Subsequently, from Eq. (6.34), the second iterative value named $T_{m,\mathrm{II}}^{i+1}$ is found. The procedure for each slice will stop when the following condition is satisfied

$$T_{m,\mathrm{j}}^{i+1}-T_{m,\mathrm{j\text{-}1}}^{i+1}<\epsilon, \tag{6.36}$$

where j is the n$^{\mathrm{th}}$ iteration and ϵ is the tolerance value chosen for the convergence.

6.4.2 Performance comparison of unconventional stacks

The performances of a thermoacoustic engines using three unconventional stacks (Wire Mesh, Tetragonal Pin Array and 3D-Membrane Foams) are compared by using the numerical scheme presented in the subsection above. Two dimensional sweeps are provided for the geometrical parameters of each stack, in particular: for Wire Mesh, $0.13\ mm < r_p < 0.78\ mm$ and $1\ mm < d_s < 3.5\ mm$; for Tetragonal Pin Array, $r_p = 0.09\ mm$, $8 < \bar{L}_x < 24$ and $8 < \bar{L}_z < 24$; for Membrane Foams, $D_t = 1\ mm$, $0.1 < \xi/D_t < 0.2$ and $0.2 < t_0 < 0.7$. The sketch used for the simulations is the one reported in Fig. 6.15. The applied boundary conditions are reported in Tab. 6.2. As it can be seen from Figs. 6.16, 6.17, 6.18, three different working frequencies $f = 100, 150, 200\ Hz$ have been chosen. The surface plots allow to recognize the set of the geometrical parameters where the stack is able to convert a positive amount of energy per unit time

$$\dot{E}_{\text{gain}} = \int \frac{1}{2} \Re \left[g p_1 \widehat{U}_1 \right] dx > 0. \tag{6.37}$$

It means that heat to mechanical energy conversion will take place. Otherwise, when $\dot{E}_{\text{gain}} < 0$, no conversion in mechanical energy will be and only dissipative process arises. In the case of Tetragonal Pin Array and Wire mesh stacks, positive and negative region $\dot{E}_{\text{gain}}$ are highlighted in the surface plots, Figs. 6.16, 6.17. It means that regions such as for very low value of $\bar{L}_z$ and high value of $\bar{L}_x$ for TBC, and for very low value of r_p and high value of d_s for Wire Mesh, heat to mechanical energy conversion is favoured, while in the region where $\dot{E}_{\text{gain}} < 0$ dissipated energy is increased due to the thermal relaxation processes. Regions where $\dot{E}_{\text{gain}} = 0$ are characterized by balanced effects between the thermoacoustic energy conversion and the losses. In the case of Membrane foams (Fig. 6.18), it can be noticed that, for the same operating parameters (Tab.6.2), no $\dot{E}_{\text{gain}} < 0$ regions exist which means only regions where heat to mechanical energy conversion will happen (low values of t_0), at least $E_{\text{gain}} = 0$ regions but the energy losses in that case are never incremented. Note that the color scale has been fixed equal for all the surface plots ($-30\ W < \dot{E}_{\text{gain}} < 15\ W$) and this is the reason why the plots in Fig. 6.18 look with uniform color (quite flat). For this reason, for each surface plot, a subplot is reported with a zoomed scale. Anyway, to be able to observe the thermoacoustic phenomenon arises the amount of energy gained per unit time $\dot{E}_{\text{gain}}$ must overcome the amount of energy dissipated for viscous and thermal interaction between the fluid and the solid skeleton of the stack $\dot{E}_{diss}$. This amount of energy is estimated through Eq. (6.10). Also for the dissipated energy per unit time $\dot{E}_{diss}$ subplots are reported in Figs. 6.19,6.20, 6.21, for each different material and operating frequency. It can be highlighted the high amount of dissipation provided by the membrane foam which is two order of magnitude greater than the one provided by the other typologies of stacks (note that the colormap scale are different for this material respect to Wire Mesh and Tetragonal Pin Array). Therefore, thermoacoustic phenomenon will take place when the sum of the gain energy and the dissipated energy per unit time is greater than zero

$$\dot{E}_{tot} = \dot{E}_{\text{gain}} + \dot{E}_{diss} > 0. \tag{6.38}$$

Figs. 6.22,6.23, 6.24 show the real potentiality of these kind of stacks to trigger the thermoacoustic phenomenon inside a device working with these operating conditions. What can be seen is that for Membrane foams seems to not be any combination of the geometrical parameters (D_t, ξ, t_0) for which thermoacoustic engine will work. While Wire Mesh and Tetragonal Pin Array provide several combinations for which the $\dot{E}_{tot} > 0$, in particular, for very low value of $\bar{L}_z$ and high value of $\bar{L}_x$ for TBC, and for very low value of r_p and high value of d_s for Wire Mesh. Finally, the Tetragonal Pin Array should be preferred respect to the Wire Mesh, because of the narrower $\dot{E}_{tot} > 0$ region. Last analysis is conducted on the quantities $\Im\left[-f_\kappa\right]$ and $\Im\left[-f_\nu\right]/|1 - f_\nu|^2$

proportional respectively to the thermal relaxation conductance and the viscous resistance offered by the material to the passing fluid (in this case air), see Eqs. (6.5b), (6.5a). In Fig. 6.25, 6.26 these quantities are plotted for the selected best stack in terms of $\dot{E}_{tot}$ against the dimensionless thermal and viscous frequencies, Eqs. (3.11c), (3.4c), black line for the Wire Mesh ($r_p = 0.13\ mm, d_s = 3.5\ mm$ for all the frequencies), blue line for the TBC ($r_p = 0.09\ mm, \bar{L}_z = 8, \bar{L}_x = 22.5$ for $f = 100\ Hz$, $r_p = 0.09\ mm, \bar{L}_z = 8, \bar{L}_x = 19.6$ for $f = 150, 200\ Hz$), and orange line for Membrane Foams ($D_t = 1\ mm, \xi/D_t = 0.1, t_0 = 0.2$ for all the frequencies). In bold red line the working region is highlighted taking into account that the operating frequency f is fixed as constant but along the stack there is a temperature variation which involves a fluid parameters variation and then in the ω_κ and ω_ν values. In particular, despite Membrane Foams are the material where $\dot{E}_{\text{gain}}$ is always positive, from Fig. 6.26 it can be seen how the viscous resistance is always the highest among the material. Therefore, these dissipations are not balanced by the gain converted and they results always the losses material to be employed in a thermoacoustic engine under these operating conditions.

Hot Duct Length	L_{hot}	$\lambda/4$
Stack Length	L_{stack}	$5\ cm$
Maximum Pressure	p_{run}	$5000\ Pa$
Hot Temperature	T_{hot}	$593\ K$
Cold Temperature	T_{cold}	$333\ K$
Heat Power	$\dot{Q}_{\text{hot}}$	$100\ W$

Table 6.2: Applied boundary conditions for the thermoacoustic engine simulations.

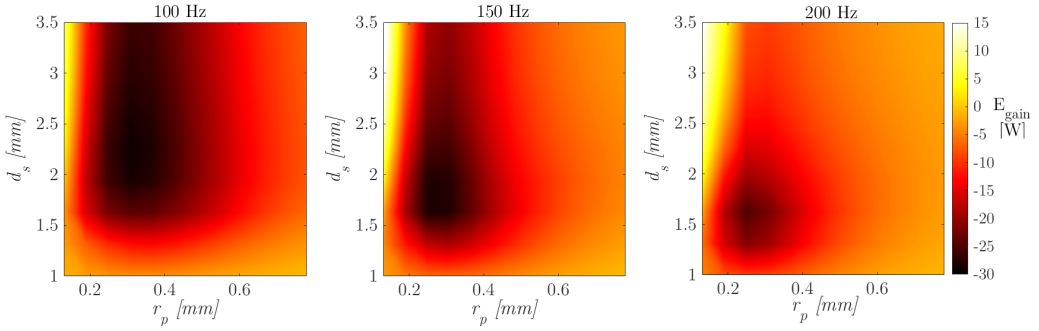

Figure 6.16: The performances, in terms of positive amount of energy per unit time $\dot{E}_{\text{gain}}$, of a thermoacoustic engines using a Wire Mesh stack. Two dimensional sweeps are provided for $0.13\ mm < r_p < 0.78\ mm$ and $1\ mm < d_s < 3.5\ mm$: left, $100\ Hz$, centered, $150\ Hz$,right, $200\ Hz$.

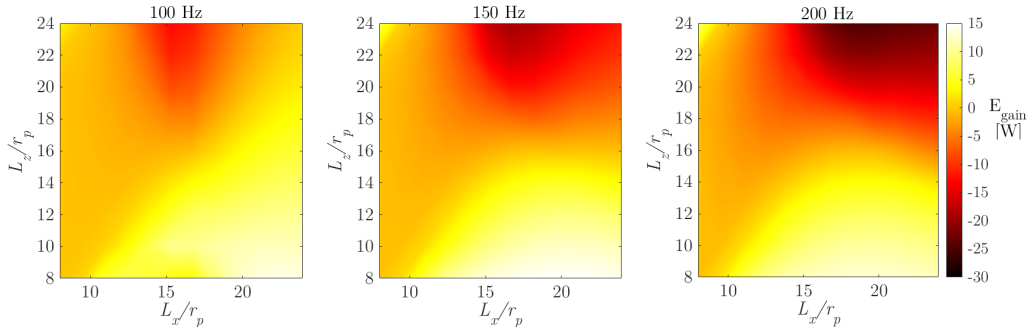

Figure 6.17: The performances, in terms of positive amount of energy per unit time $\dot{E}_{\text{gain}}$, of a thermoacoustic engines using a Tetragonal Pin Array stack. Two dimensional sweeps are provided for $r_p = 0.09\ mm$, $8 < \bar{L}_x < 24$ and $8 < \bar{L}_z < 24$: left, 100 Hz, centered, 150 Hz,right, 200 Hz.

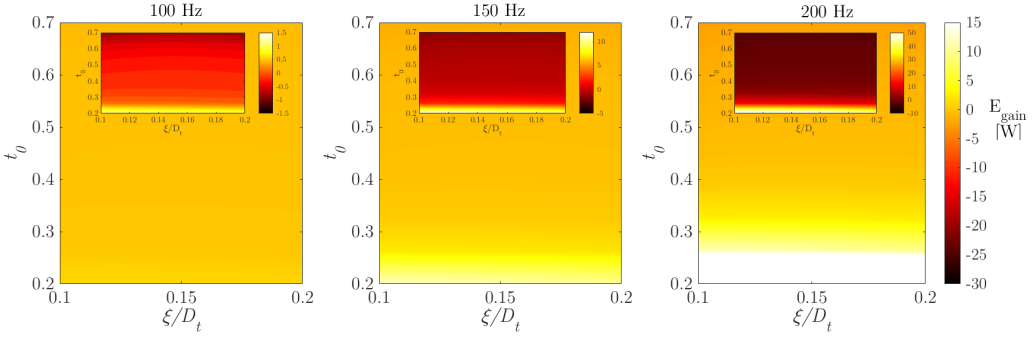

Figure 6.18: The performances, in terms of positive amount of energy per unit time $\dot{E}_{\text{gain}}$, of a thermoacoustic engines using a 3D-Membrane Foam stack. Two dimensional sweeps are provided for $D_t = 1\ mm$, $0.1 < \xi/D_t < 0.2$ and $0.2 < t_0 < 0.7$: left, 100 Hz, centered, 150 Hz,right, 200 Hz. For each surface plot, a subplot is reported with a zoomed scale.

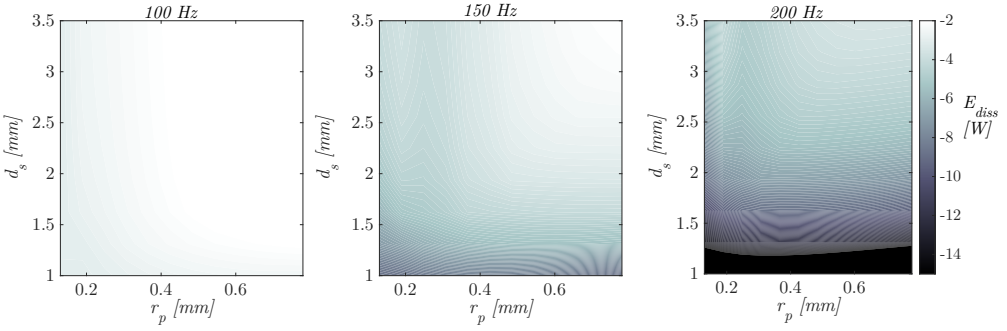

Figure 6.19: The dissipated energy per unit time $\dot{E}_{diss}$, of a thermoacoustic engines using a Wire Mesh stack. Two dimensional sweeps are provided for $0.13\ mm < r_p < 0.78\ mm$ and $1\ mm < d_s < 3.5\ mm$: left, 100 Hz, centered, 150 Hz,right, 200 Hz.

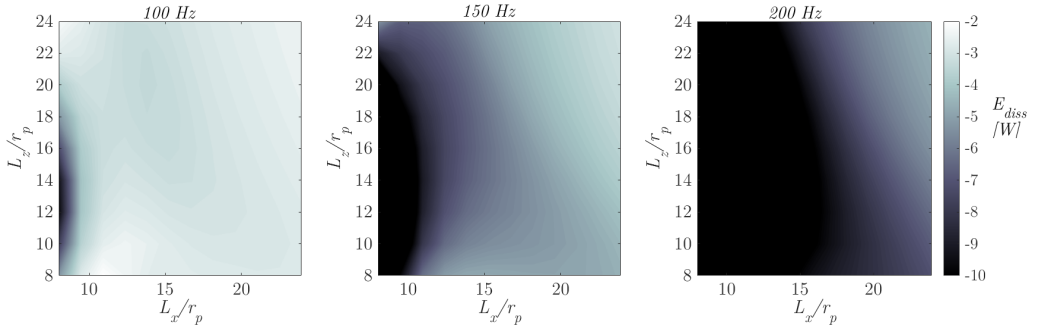

Figure 6.20: The dissipated energy per unit time $\dot{E}_{diss}$, of a thermoacoustic engines using a Tetragonal Pin Array stack stack. Two dimensional sweeps are provided for $r_p = 0.09\ mm$, $8 < \bar{L}_x < 24$ and $8 < \bar{L}_z < 24$: left, 100 Hz, centered, 150 Hz,right, 200 Hz.

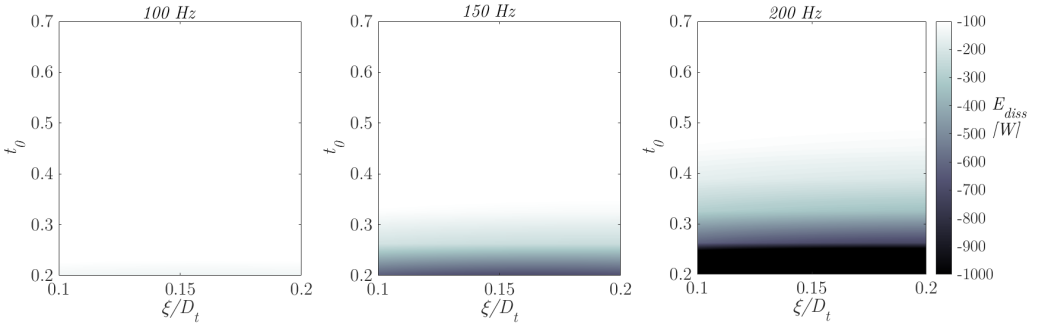

Figure 6.21: The dissipated energy per unit time $\dot{E}_{diss}$, of a thermoacoustic engines using a 3D-Membrane Foam stack. Two dimensional sweeps are provided for $D_t = 1\ mm$, $0.1 < \xi/D_t < 0.2$ and $0.2 < t_0 < 0.7$: left, 100 Hz, centered, 150 Hz,right, 200 Hz.

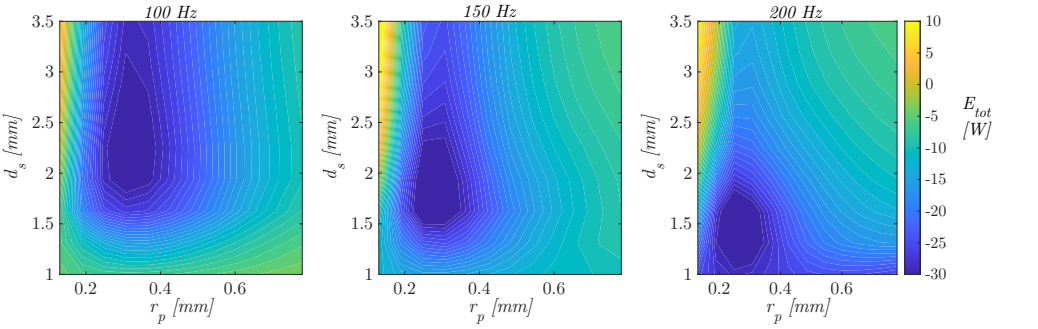

Figure 6.22: The total amount of energy per unit time $\dot{E}_{tot}$, of a thermoacoustic engines using a Wire Mesh stack. Two dimensional sweeps are provided for $0.13\ mm < r_p < 0.78\ mm$ and $1\ mm < d_s < 3.5\ mm$: left, 100 Hz, centered, 150 Hz,right, 200 Hz.

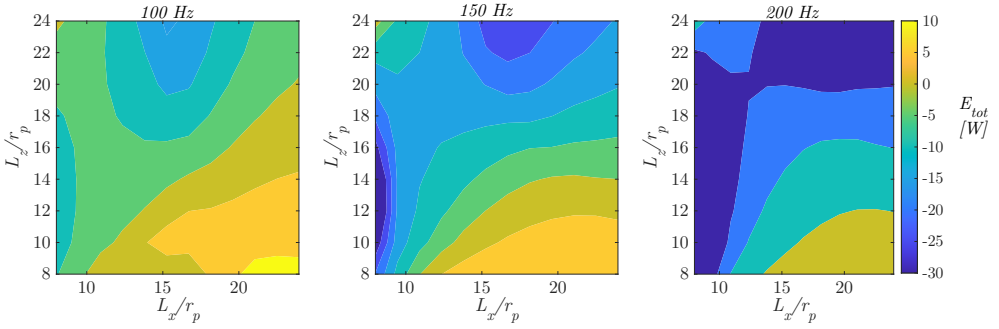

Figure 6.23: The total amount of energy per unit time $\dot{E}_{tot}$, of a thermoacoustic engines using a Tetragonal Pin Array stack stack. Two dimensional sweeps are provided for $r_p = 0.09\ mm$, $8 < \bar{L}_x < 24$ and $8 < \bar{L}_z < 24$: left, 100 Hz, centered, 150 Hz,right, 200 Hz.

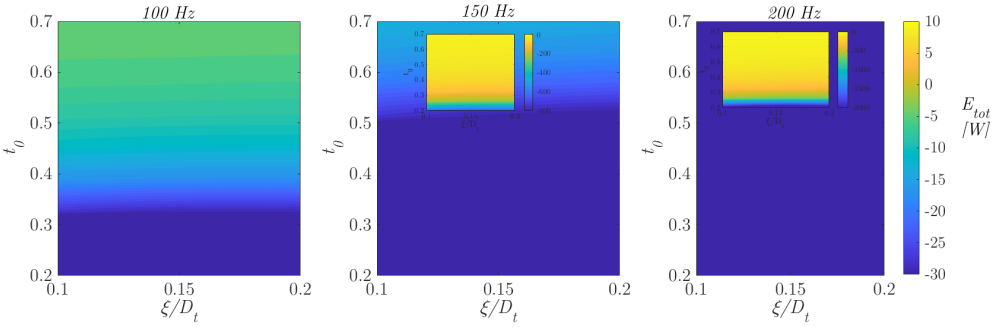

Figure 6.24: The total amount of energy per unit time $\dot{E}_{diss}$, of a thermoacoustic engines using a 3D-Membrane Foam stack. Two dimensional sweeps are provided for $D_t = 1\ mm$, $0.1 < \xi/D_t < 0.2$ and $0.2 < t_0 < 0.7$: left, 100 Hz, centered, 150 Hz,right, 200 Hz. For central and right surface plot, a subplot is reported with an extended scale.

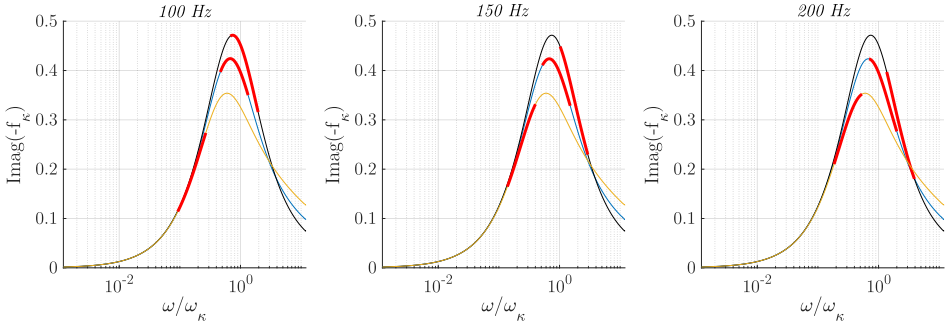

Figure 6.25: Comparison between the quantity $\Im\left[-f_\kappa\right]$ of the three different materials (black line for the Wire Mesh, blue line for the TBC and orange line for Membrane Foams): left, 100 Hz, centered, 150 Hz,right, 200 Hz. In bold red line the working region in terms of dimensionless thermal frequency taking into account the temperature variation along the stack.

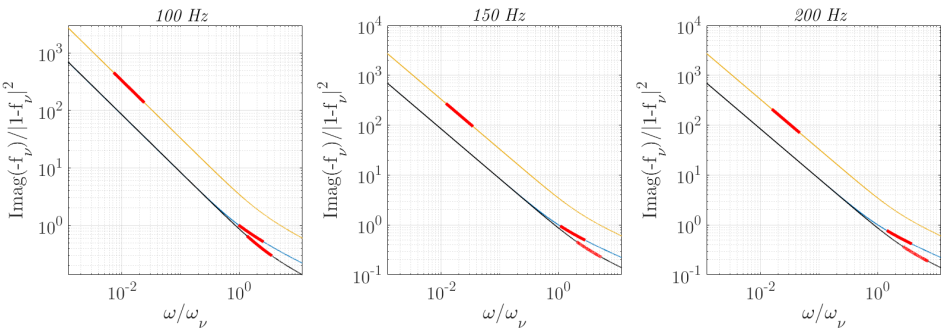

Figure 6.26: Comparison between the quantity $\Im\left[-f_\nu\right]/|1-f_\nu|^2$ of the three different materials (black line for the Wire Mesh, blue line for the TBC and orange line for Membrane Foams): left, 100 Hz, centered, 150 Hz,right, 200 Hz. In bold red line the working region in terms of dimensionless viscous frequency taking into account the temperature variation along the stack.

Chapter 7

Conclusions

Contents

7.1 General conclusions

Porous materials represent the core of thermoacoustic devices. In this work the relations between the microgeometrical features (*transport parameters*) and the dynamic viscous and thermal behaviors of the porous materials have been investigated. In particular, predictive models have been developed to correlate the *transport parameters* with the geometrical dimensions, for three different typologies of materials: Tetragonal Pin Array, Wire Mesh and 3D-Membrane Foams. *Finite Element* based simulations allowed to numerically estimate the transport parameters from the resolution of the Stokes, Laplace and Poisson's problems inside the Representative Elementary Volume of the material. In fact, thanks to the diffusion of the additive manufacturing technology precise-controlled geometry porous materials can be realized. Therefore, a predictive model is a powerful tool in the design phase of both sound absorption applications and thermoacoustic applications. In the first case, the aim is to maximize the energy dissipation due to the viscous and thermal losses when the sound propagate in the solid skeleton. While in the second case, the goal is to find the optimal balance between viscous resistance and thermal relaxation effects in order to trigger the thermoacoustic phenomenon, i.e. the heat to mechanical energy conversion (and *vice versa*). Furthermore, two new experimental apparatuses and techniques have been developed to accurately characterize porous media in low frequency range. These techniques are lumped element based and the analysis for the frequency validity ranges has been synthesized in $|\tilde{k}d| < 0.5$. Subsequently, an energetic criterion has been developed to qualitatively predict the performance of a porous material used as *stack*. In particular, $\Im\left[-f_\kappa\right]$ and $\Im\left[-f_\nu\right]/|1-f_\nu|^2$ functions are studied as functions of the transport parameters of a generic porous material modelled with Johnson-Champoux-Allard-Lafarge semi phenomenological model. Finally, a comparison between the performances of a thermoacoustic engine using the three different *stack* (Tetragonal Pin Array, Wire Mesh and 3D-Membrane Foams) and the same operating conditions has been reported in terms of amount of energy gained and dissipated energy per unit time.

7.2 Future remarks

The experimental activities have been carried out entirely at the Acoustic Laboratory of the Industrial Engineering Department (LAD), University of Naples *Federico II*. Numerical elaborations have been partially conducted in Naples and partially at *Laboratorie Modélisation and simulation multi échelle* of University *Gustave Eiffel* in Paris. The predictive models of the viscous and thermal behaviour of the presented *stacks* have been tested with a total acoustic setup (only the microphones and the loudspeaker). As future remarks, in the LAD of University *Federico II* a first prototype of a thermoacoustic engine, shown in Fig. 7.1, has been realized in order to thermoacoustically test the predictive models also of the performances of the thermoacoustic devices using unconventional porous *stacks*. Internal heat exchangers are replaced with external heat sources to keep as many parameters under control as possible. To supply the high temperature heat power, a heating tape in particular is adopted. When the operating temperature is achieved, the thermoregulator that controls its power supply can turn off the heating tape. A Variac is used to regulate the electrical voltage, current, and then the power. The ambient heat exchanger is performed by an external cooling serpentine. A serpentine surrounds the device and receives water at ambient temperature from a resevoir through a pump. A *stack* holder composed of insulating ceramic material is used to thermally separate the device's hot and cold parts in order to prevent thermal bridges. Thermocouples and microphones conclude the probes. Different thermoacoustic measurements will be made using such a system by changing the controlled process parameters, including the input heat power, the hot temperature, the employed *stack*, and its location. Verifying the accuracy of the models presented in predicting thermoacoustic performance will be a future goal.

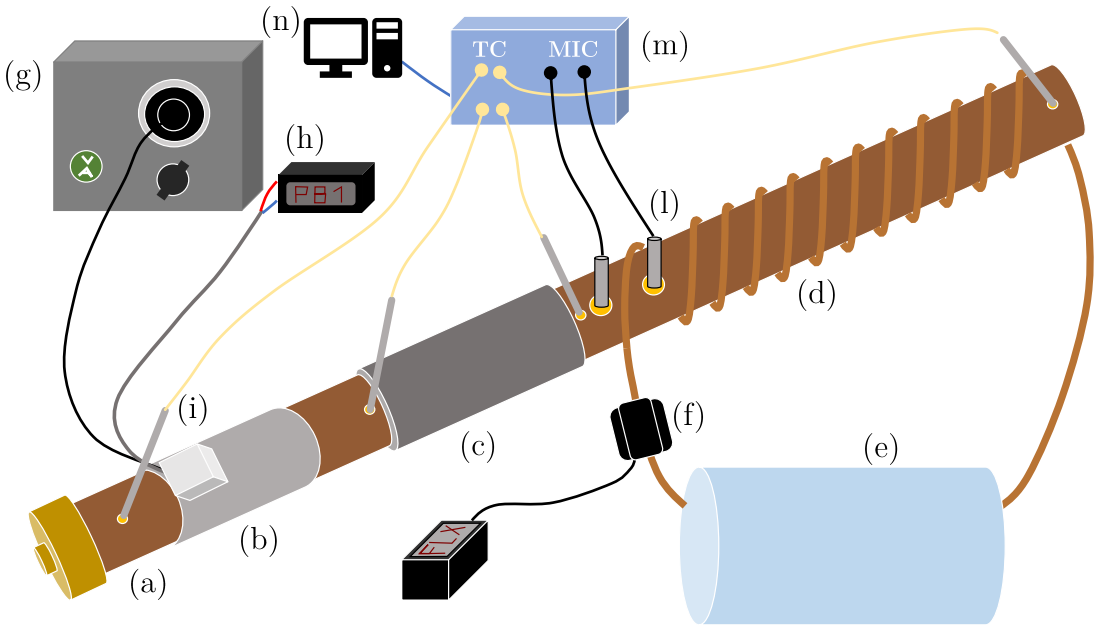

Figure 7.1: Thermoacoustic engine prototype realized in Acoustic Lab of University of Naples *Federico II*. The components: (a) copper tube, (b) heating tape, (c), *stack* holder made by insulating ceramic material, (d) cooling serpetine, (e) ambient temperature resevoir, (f) flowmeter, (g) Voltage Variac, (h) heating tape thermal controller, (i) thermocouple type K, (l) microphone, (m) data acquisition system, (n) post-processing computer.

Appendix A

Definition of the unit cell for Wire Mesh

Wire meshes are realized by intertwined metal filaments (Figs. A.1.a and A.1.b). The geometry of the RVE was simplified by considering intersecting filaments at the junctions (Figs. A.1.c and A.1.d). The effects of this simplification on the transport parameter values were assessed by means of numerical simulations on a single layer. The relative differences Δ between transport parameters of intertwined and intersecting filaments was much lower than 5%, with a small exception for the characteristic length (attributed to the lower wetted surface area ratio of the straight pattern); Tab. A.1. Following this analysis, the simplified geometry was chosen to realize the RVE, mainly for two reasons: (i) the greater simplicity to build the geometry; (ii) this approach allowed us to avoid uncertainties usually associated with the analysis of singular geometrical problems (due to the mesh in the vicinity of critical points, such as the contact of two filaments in the intertwined case).The representative volume element (RVE) on which the numerical simulations are carried out is based on six superimposed layers, randomly oriented (Fig. 4.3.b). The convergence of the transport parameters was assessed by adding progressively supplementary layers of wire-mesh. For a given number of layers, the simulations were repeated four times with the relative orientation of each horizontal layer being chosen randomly. Results are presented as mean $\pm$ standard deviation (Fig. A.2). The relative difference Δ between the mean value corresponding to a transport parameter with n layers and the mean value corresponding to the same transport parameter with $n-1$ layers was found to be less than 1% for the porosity (Fig. A.2.a) and for the tortuosity (Fig. A.2.b), and less that 5% for the characteristic lengths (Figs. A.2.c and A.2.d); with $n = 6$. Considering the viscous k_0 and thermal k_0' permeabilities, the relative difference declines appreciably with the number of layers, with a relatively stable level for $n \geq 4$ (Figs. A.2.e and A.2.f). A value of $n = 6$ represents a good tradeoff between accuracy and computational time.

Geometry	φ	α_∞	Λ	Λ'	k_0	k_0'
Intertwined	0.9536	1.0385	0.7936	2.6254	0.2981	0.5115
Intersecting	0.9533	1.0456	0.7596	2.7806	0.2930	0.5199
$\Delta\%$	0.04	0.68	4.49	5.58	1.73	1.60

Table A.1: Transport parameter values of an intertwined and intersecting wire mesh geometry $\left(r_p = 0.15\ mm, d_s = 3.3\ mm\right)$.

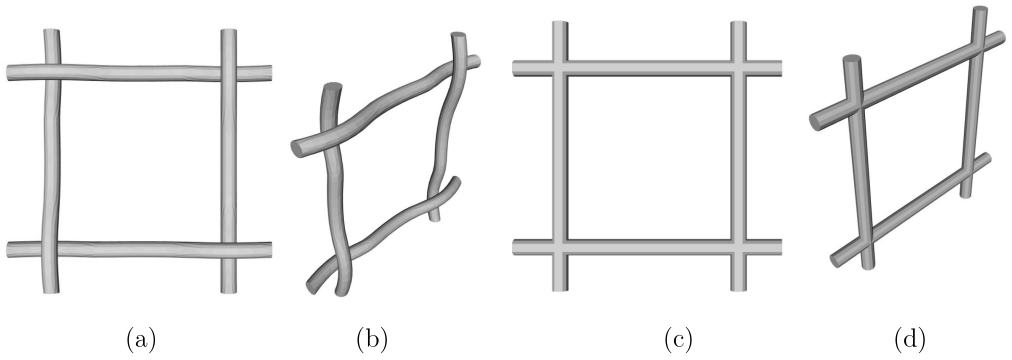

Figure A.1: Intertwined metal filaments. (front (a) and perspective (b) views) compared to the simplified model with intersecting filaments (front (c) and perspective (d) views).

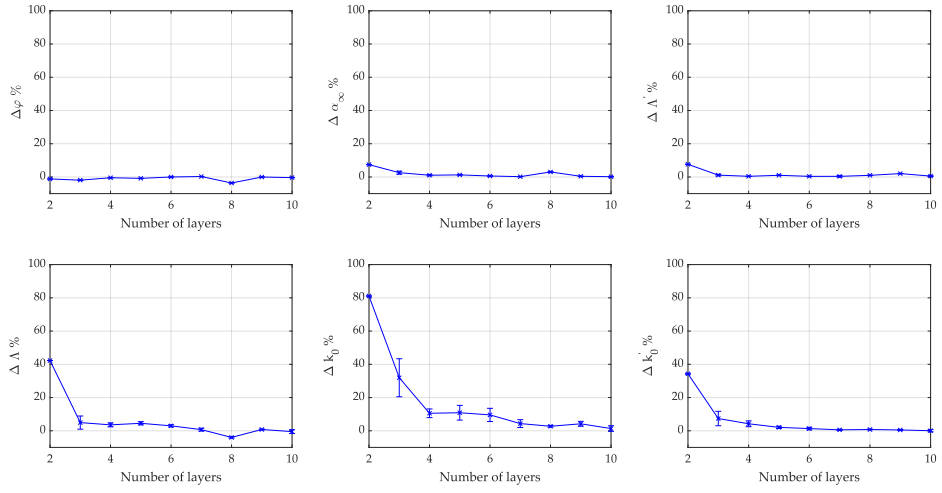

Figure A.2: The relative variation between a calculation with n layers and the previous one with $n-1$ layers for: (a) the porosity φ, (b), the high frequency limit of tortuosity α_∞, (c) the thermal characteristic length Λ', (d) the viscous characteristic length Λ, (e) the static viscous permeability k_0, (f) the static thermal permeability k_0'.

Appendix B

Convergence analysis for Membrane Foams

Langlois, Trinh and Perrot [94] highlighted how the electrical resistivity and the high-frequency tortuosity of solid foam are modified by the presence of membranes that partially or totally close the cell windows connecting neighbor pores. Laplace problem could present singulary points in the fluid domain where discontinuities of the solid boundary are heightened, such as presence of holes, thin membranes, cusps or any angular points. Therefore, to avoid numerical convergence problems in the resolution of electrical fields, the edges of the 3D-Membrane Foams have been rounded in order to allow a convergence trend as the mesh size is reduced (Fig. B.1). In Fig. B.2 the comparison between the no-rounded edges and the rounded edges for three different values of the radius $R = 0.02, 0.005, 0.001\ mm$ is reported for both the tortuosity and the thermal characteristic length. It can be seen how the no-rounded edges geometry does not show a convergent trend with the reducing of the mesh size, while in the case of rounded edges it can be recognized a convergent trend to different values, but very close one to each other. In particular, the smaller the radius, the closer the curves. For the presented study the chosen radius is $0.001\ mm$.

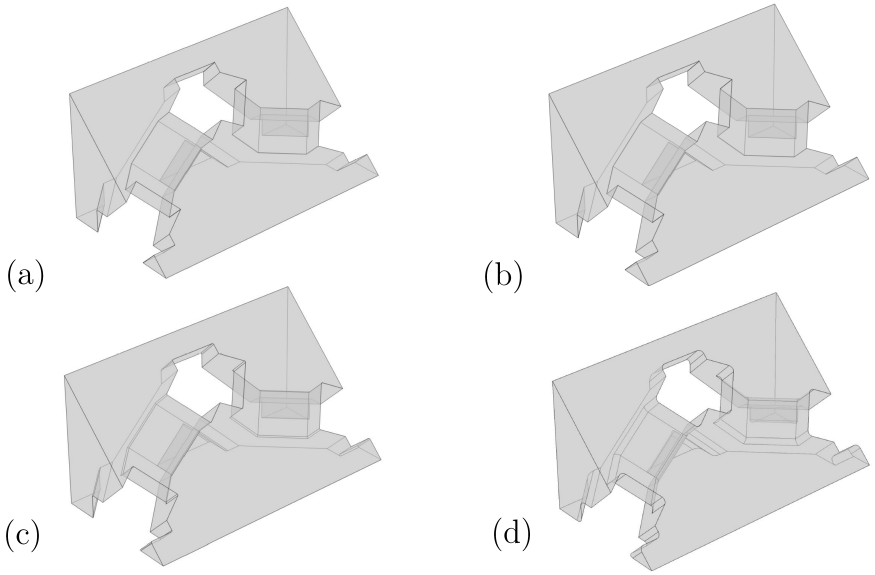

Figure B.1: One eighth part of the Representative Elementary Volume of 3D-Membrane Foams with: (a) no-rounded edges, (b) rounded edge with radius $0.001\ mm$,(c) rounded edge with radius $0.005\ mm$,(b) rounded edge with radius $0.02\ mm$.

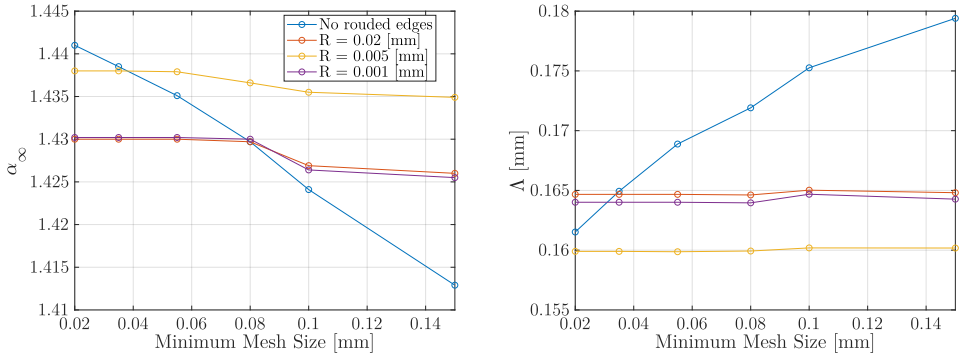

Figure B.2: Comparison between the no-rounded edges and the rounded edges for three different values of the radius $R = 0.02, 0.005, 0.001\ mm$ reported for: on the left, the tortuosity; on the right, the thermal characteristic length.

Bibliography

[1] S. Backhaus, E. Tward, and M. Petach. "Traveling-wave thermoacoustic electric generator". In: *Applied Physics Letters* 85.6 (2004), pp. 1085–1087. ISSN: 00036951. DOI: 10.1063/1.1781739.

[2] Ercang Luo, Wei Dai, Yong Zhang, and Hong Ling. "Thermoacoustically driven refrigerator with double thermoacoustic-Stirling cycles". In: *Applied Physics Letters* 88.7 (2006). ISSN: 00036951. DOI: 10.1063/1.2176855.

[3] Islam Ramadan, Helene Bailliet, Gaelle Poignand, and David Gardner. "Design, manufacturing and testing of a compact thermoacoustic refrigerator". In: *Elsevier* 189 (2021), p. 116705.

[4] Wei Dai, Ercang Luo, Jianying Hu, and Hong Ling. "A Heat-driven thermoacoustic cooler capable of reaching liquid nitrogen temperature". In: *Applied Physics Letters* 86.22 (2005), pp. 1–3. ISSN: 00036951. DOI: 10.1063/1.1941472.

[5] O. G. Symko, E. Abdel-Rahman, Y. S. Kwon, M. Emmi, and R. Behunin. "Design and development of high-frequency thermoacoustic engines for thermal management in microelectronics". In: *Microelectronics Journal* 35.2 (2004), pp. 185–191. ISSN: 0026-2692. DOI: 10.1016/J.MEJO.2003.09.017.

[6] G. W. Swift. "Thermoacoustic engines". In: *The Journal of the Acoustical Society of America* 84.4 (1998), p. 1145. ISSN: 0001-4966. DOI: 10.1121/1.396617.

[7] Massoud Kaviany. *Principles of Heat Transfer in Porous Media*. Ed. by Springer. Springer, 1995, Chapt. I.

[8] L.D. Landau and E.M. Lifshitz. *Fluid Mechanics*. Ed. by Pergamon Press. Second. Pergamon Press, 1987, Chapt. I, II, V.

[9] Jean F. Allard and Noureddine Atalla. *Propagation of Sound in Porous Media: Modelling Sound Absorbing Materials*. John Wiley and Sons, 2009, pp. 1–358. DOI: 10.1002/9780470747339.

[10] Gregory W. Swift. *Thermoacoustics : a unifying perspective for some engines and refrigerators.* Springer, 2018. ISBN: 3319883488.

[11] Nikolaus Rott. "Damped and thermally driven acoustic oscillations in wide and narrow tubes". In: *Zeitschrift für angewandte Mathematik und Physik ZAMP 1969 20:2* 20.2 (1969), pp. 230–243. ISSN: 1420-9039. DOI: 10.1007/BF01595562.

[12] Jean Louis Auriault, Claude Boutin, and Christian Geindreau. *Homogenization of Coupled Phenomena in Heterogenous Media*. Wiley-ISTE, 2010. ISBN: 9781848211612. DOI: 10.1002/9780470612033.

[13] G. Kirchhoff. "Ueber den Einfluss der Wärmeleitung in einem Gase auf die Schallbewegung". In: *Annalen der Physik* 210.6 (1868), pp. 177–193. ISSN: 1521-3889. DOI: 10.1002/ANDP.18682100602.

[14] Michael R. Stinson. “The propagation of plane sound waves in narrow and wide circular tubes, and generalization to uniform tubes of arbitrary cross-sectional shape”. In: *The Journal of the Acoustical Society of America* 89.2 (1998), p. 550. ISSN: 0001-4966. DOI: 10.1121/1.400379.

[15] C. Zwikker and C.W. Kosten. *Sound Absorbing Materials*. Ed. by Elsevier. 1949.

[16] Guoqiang Lu and Ping Cheng. “Friction Factor and Nusselt Number for Thermoacoustic Transport Phenomena in a Tube”. In: *Journal of Thermophysics and Heat Transfer* 14.4 (2000), pp. 566–573. ISSN: 08878722. DOI: 10.2514/2.6558.

[17] Jin Liu and Steven L. Garrett. “Relationship between Nusselt number and the thermoviscous (Rott) functions”. In: *The Journal of the Acoustical Society of America* 119.3 (2006), p. 1457. ISSN: 0001-4966. DOI: 10.1121/1.2165000.

[18] Raffaele Dragonetti, Marialuisa Napolitano, Sabato Di Filippo, and Rosario Romano. “Modeling energy conversion in a tortuous stack for thermoacostic applications”. In: *Applied Thermal Engineering* 103 (2016), pp. 233–242. ISSN: 1359-4311. DOI: 10.1016/J.APPLTHERMALENG.2016.04.076.

[19] G. A. Russell and E. D. Hjerpe. “On the analogy between the one-dimensional acoustic waveguide and the electrical transmission line”. In: *Journal of the Acoustical Society of America* 94.1 (1993), pp. 583–584. ISSN: NA. DOI: 10.1121/1.407073.

[20] M. L. Munjal. *Acoustics of Ducts and Mufflers*. Ed. by Wiley. 2014, Chapt. I, II. ISBN: 978-1-118-44312-5.

[21] John William Rayleigh. “The theory of sound”. In: *The Theory of Sound* 9781108032 (1877), pp. 1–326. DOI: 10.1017/CBO9781139058087.

[22] Armando Di Meglio, Elio Di Giulio, Raffaele Dragonetti, and Nicola Massarotti. “Analysis of heat capacity ratio on porous media in oscillating flow”. In: *International Journal of Heat and Mass Transfer* 179 (2021), p. 121724. ISSN: 0017-9310. DOI: 10.1016/J.IJHEATMASSTRANSFER.2021.121724.

[23] M. E. Delany and E. N. Bazley. “Acoustical properties of fibrous absorbent materials”. In: *Applied Acoustics* 3.2 (1970), pp. 105–116. ISSN: 0003-682X. DOI: 10.1016/0003-682X(70)90031-9.

[24] Yasushi Miki. “Acoustical properties of porous materials-Modifications of Delany-Bazley models-”. In: *Journal of the Acoustical Society of Japan (E)* 11.1 (1990), pp. 19–24. ISSN: 0388-2861. DOI: 10.1250/AST.11.19.

[25] D. Keith Wilson. “Relaxation-matched modeling of propagation through porous media, including fractal pore structure”. In: *The Journal of the Acoustical Society of America* 94.2 (1998), p. 1136. ISSN: 0001-4966. DOI: 10.1121/1.406961.

[26] David Linton Johnson, Joel Koplik, and Roger Dashen. “Theory of dynamic permeability and tortuosity in fluid-saturated porous media”. In: *Journal of Fluid Mechanics* 176 (1987), pp. 379–402. ISSN: 1469-7645. DOI: 10.1017/S0022112087000727.

[27] Yvan Champoux and Jean-F. Allard. “Dynamic tortuosity and bulk modulus in air-saturated porous media”. In: *Journal of Applied Physics* 70.4 (1998), p. 1975. ISSN: 0021-8979. DOI: 10.1063/1.349482.

[28] Denis Lafarge, Pavel Lemarinier, Jean F. Allard, and Viggo Tarnow. “Dynamic compressibility of air in porous structures at audible frequencies”. In: *The Journal of the Acoustical Society of America* 102.4 (1998), p. 1995. ISSN: 0001-4966. DOI: 10.1121/1.419690.

[29] Steven R. Pride, Frank Dale Morgan, and Anthony F. Gangi. “Drag forces of porous-medium acoustics”. In: *Physical Review B* 47.9 (1993), p. 4964. ISSN: 01631829. DOI: 10.1103/PhysRevB.47.4964.

[30] D. A. Bies and C. H. Hansen. “Flow resistance information for acoustical design”. In: *Applied Acoustics* 13.5 (1980), pp. 357–391. ISSN: 0003-682X. DOI: 10.1016/0003-682X(80)90002-X.

[31] M. Garai and Francesco. Pompoli. “A simple empirical model of polyester fibre materials for acoustical applications”. In: *Applied Acoustics* 66 (2005), pp. 1383–1398.

[32] I.P. Dunn and W.A. Davern. “Calculation of acoustic impedance of multi-layer absorbers”. In: *Applied Acoustics,* 19 (1986), pp. 321–34.

[33] M. Avellaneda and S. Torquato. “Rigorous link between fluid permeability, electrical conductivity, and relaxation times for transport in porous media”. In: *Physics of Fluids A: Fluid Dynamics* 3.11 (1998), p. 2529. ISSN: 0899-8213. DOI: 10.1063/1.858194.

[34] Raymond Panneton and Xavier Olny. “Acoustical determination of the parameters governing viscous dissipation in porous media”. In: *The Journal of the Acoustical Society of America* 119.4 (2006), p. 2027. ISSN: 0001-4966. DOI: 10.1121/1.2169923.

[35] Xavier Olny and Raymond Panneton. “Acoustical determination of the parameters governing thermal dissipation in porous media”. In: *The Journal of the Acoustical Society of America* 123.2 (2008), p. 814. ISSN: 0001-4966. DOI: 10.1121/1.2828066.

[36] Leo L. Beranek. “Acoustic Impedance of Porous Materials”. In: *The Journal of the Acoustical Society of America* 13.3 (2005), p. 248. ISSN: 0001-4966. DOI: 10.1121/1.1916172.

[37] Y. Salissou and R. Panneton. “Pressure/mass method to measure open porosity of porous solids”. In: *Journal of Applied Physics* 101.12 (2007), p. 124913. ISSN: 0021-8979. DOI: 10.1063/1.2749486.

[38] Olga Umnova, Keith Attenborough, Ho Chul Shin, and Alan Cummings. “Deduction of tortuosity and porosity from acoustic reflection and transmission measurements on thick samples of rigid-porous materials”. In: *Applied Acoustics* 66.6 (2005), pp. 607–624. ISSN: 0003-682X. DOI: 10.1016/J.APACOUST.2004.02.005.

[39] Z. E. A. Fellah, S. Berger, W. Lauriks, C. Depollier, C. Aristégui, and J.-Y. Chapelon. “Measuring the porosity and the tortuosity of porous materials via reflected waves at oblique incidence”. In: *The Journal of the Acoustical Society of America* 113.5 (2003), p. 2424. ISSN: 0001-4966. DOI: 10.1121/1.1567275.

[40] American Society for Testing and Materials. *C522-03 - Standard Test Method for Airflow Resistance of Acoustical Materials*. 2016. DOI: 10.1520/C0522-03R16.

[41] International Organization for Standardization Occupational Safety and Health Administration. *ISO 9053-1:2018 - Acoustics - Determination of airflow resistance — Part 1: Static airflow method*. 2018.

[42] International Organization for Standardization Occupational Safety and Health Administration. *ISO 9053-2:2020 - Acoustics — Determination of airflow resistance — Part 2: Alternating airflow method*.

[43] Raffaele Dragonetti, Carmine Ianniello, and Rosario A. Romano. “Measurement of the resistivity of porous materials with an alternating air-flow method”. In: *The Journal of the Acoustical Society of America* 129.2 (2011), p. 753. ISSN: 0001-4966. DOI: 10.1121/1.3523433.

[44] P. Leclaire, L. Kelders, W. Lauriks, C. Glorieux, and J. Thoen. “Determination of the viscous characteristic length in air-filled porous materials by ultrasonic attenuation measurements”. In: *The Journal of the Acoustical Society of America* 99.4 (1998), p. 1944. ISSN: 0001-4966. DOI: 10.1121/1.415378.

[45] F Fohr, D Parmentier, B R J Castagnede, and M Henry. “An alternative and industrial method using low frequency ultrasound enabling to measure quickly tortuosity and viscous characteristic length”. In: *Proceedings - European Conference on Noise Control*. Acoustical Society of America (ASA), 2008, pp. 955–959.

[46] Michel Henry and Jean F. Allard. “Acoustical measurement of the trapping constant of foams with open cells”. In: *Comptes Rendus de l’Académie des Sciences - Series IIB - Mechanics-Physics-Chemistry-Astronomy* 325.6 (1997), pp. 331–338. ISSN: 1251-8069. DOI: 10.1016/S1251-8069(97)81151-7.

[47] Alexis Debray, Jean F. Allard, Walter Lauriks, and Luc Kelders. “Acoustical measurement of the trapping constant of porous materials”. In: *Review of Scientific Instruments* 68.12 (1998), p. 4462. ISSN: 0034-6748. DOI: 10.1063/1.1148414.

[48] Viggo Tarnow. “Measurement of sound propagation in glass wool”. In: *The Journal of the Acoustical Society of America* 97.4 (1998), p. 2272. ISSN: 0001-4966. DOI: 10.1121/1.411952.

[49] Yacoubou Salissou, Raymond Panneton, and Olivier Doutres. “Complement to standard method for measuring normal incidence sound transmission loss with three microphones”. In: *The Journal of the Acoustical Society of America* 131.3 (2012), EL216. ISSN: 0001-4966. DOI: 10.1121/1.3681016.

[50] American Society for Testing and Materials. *E2611 - 09 - Standard Test Method for Measurement of Normal Incidence Sound Transmission of Acoustical Materials Based on the Transfer Matrix Method*. 2017. DOI: 10.1520/E2611-09.

[51] Hideo Utsuno, Toshimitsu Tanaka, Takeshi Fujikawa, and A. F. Seybert. “Transfer function method for measuring characteristic impedance and propagation constant of porous materials”. In: *The Journal of the Acoustical Society of America* 86.2 (1998), p. 637. ISSN: 0001-4966. DOI: 10.1121/1.398241.

[52] Elio Di Giulio, Marialuisa Napolitano, Armando Di Meglio, Rosario Aniello Romano, and Raffaele Dragonetti. “Low frequency acoustic method to measure the complex density of porous materials”. In: *The Journal of the Acoustical Society of America* 152.4 (2022), p. 2220. ISSN: 0001-4966. DOI: 10.1121/10.0014762.

[53] Marialuisa Napolitano, Elio Di Giulio, Fabio Auriemma, Rosario Aniello Romano, and Raffaele Dragonetti. “Low frequency acoustic method to measure the complex bulk modulus of porous materials”. In: *The Journal of the Acoustical Society of America* 151.3 (2022), pp. 1545–1556. ISSN: 0001-4966. DOI: 10.1121/10.0009767.

[54] Luc Jaouen, Emmanuel Gourdon, Philippe Glé, and Philippe Gl. “Estimation of all six parameters of Johnson-Champoux-Allard-Lafarge model for acoustical porous materials from impedance tube measurements”. In: *The Journal of the Acoustical Society of America* 148.4 (2020), p. 1998. ISSN: 0001-4966. DOI: 10.1121/10.0002162.

[55] Olivier Doutres, Yacoubou Salissou, Noureddine Atalla, and Raymond Panneton. “Evaluation of the acoustic and non-acoustic properties of sound absorbing materials using a three-microphone impedance tube”. In: *Applied Acoustics* 71.6 (2010), pp. 506–509. ISSN: 0003-682X. DOI: 10.1016/J.APACOUST.2010.01.007.

[56] Kirill V. Horoshenkov, Amir Khan, François-Xavier Bécot, Luc Jaouen, Franck Sgard, Amélie Renault, Nesrine Amirouche, Francesco Pompoli, Nicola Prodi, Paolo Bonfiglio, Giulio Pispola, Francesco Asdrubali, Jörn Hübelt, Noureddine Atalla, Celse K. Amédin, Walter Lauriks, and Laurens Boeckx. "Reproducibility experiments on measuring acoustical properties of rigid-frame porous media (round-robin tests)". In: *The Journal of the Acoustical Society of America* 122.1 (2007), p. 345. ISSN: 0001-4966. DOI: 10.1121/1.2739806.

[57] Francesco Pompoli, Paolo Bonfiglio, Kirill V. Horoshenkov, Amir Khan, Luc Jaouen, François-Xavier Bécot, Franck Sgard, Francesco Asdrubali, Francesco D'Alessandro, Jörn Hübelt, Noureddine Atalla, Celse K. Amédin, Walter Lauriks, and Laurens Boeckx. "How reproducible is the acoustical characterization of porous media?" In: *The Journal of the Acoustical Society of America* 141.2 (2017), p. 945. ISSN: 0001-4966. DOI: 10.1121/1.4976087.

[58] Youssef Atalla and Raymond Panneton. "Inverse acoustical characterization of open cell porous media using impedance tube measurements". In: *Canadian Acoustics* 33 (2005).

[59] Raffaele Dragonetti, Carmine Ianniello, and Rosario Aniello Romano. "The evaluation of intrinsic non-acoustic parameters of polyester fibrous materials by an optimization procedure". In: *Euronoise* (2006).

[60] Tomasz G. Zieliński, Rodolfo Venegas, Camille Perrot, Milan Červenka, Fabien Chevillotte, and Keith Attenborough. "Benchmarks for microstructure-based modelling of sound absorbing rigid-frame porous media". In: *Journal of Sound and Vibration* 483 (2020), p. 115441. ISSN: 0022-460X. DOI: 10.1016/J.JSV.2020.115441.

[61] R. J.S. Brown. "Connection between formation factor for electrical resistivity and fluid-solid coupling factor in Biot's equations for acoustic waves in fluid-filled porous media". In: *Geophysics* 45.8 (1980), pp. 1269–1275. ISSN: 00168033. DOI: 10.1190/1.1441123.

[62] G. E. Archie. "The Electrical Resistivity Log as an Aid in Determining Some Reservoir Characteristics". In: *Transactions of the AIME* 146.01 (1942), pp. 54–62. ISSN: 0081-1696. DOI: 10.2118/942054-G.

[63] Tomasz G. Zieliński, Nicolas Dauchez, Thomas Boutin, Mikel Leturia, Alexandre Wilkinson, Fabien Chevillotte, François Xavier Bécot, and Rodolfo Venegas. "Taking advantage of a 3D printing imperfection in the development of sound-absorbing materials". In: *Applied Acoustics* 197 (2022), p. 108941. ISSN: 0003-682X. DOI: 10.1016/J.APACOUST.2022.108941.

[64] Sagar Deshmukh, Harshavardhan Ronge, and Sripriya Ramamoorthy. "Design of periodic foam structures for acoustic applications: Concept, parametric study and experimental validation". In: *Materials & Design* 175 (2019), p. 107830. ISSN: 0264-1275. DOI: 10.1016/J.MATDES.2019.107830.

[65] William Johnston and Bhisham Sharma. "Additive manufacturing of fibrous sound absorbers". In: *Additive Manufacturing* 41 (2021), p. 101984. ISSN: 2214-8604. DOI: 10.1016/J.ADDMA.2021.101984. arXiv: 2101.05114.

[66] Jean Boulvert, Josué Costa-Baptista, Théo Cavalieri, Maxime Perna, Edith Roland Fotsing, Vicente Romero-García, Gwénaël Gabard, Annie Ross, Jacky Mardjono, and Jean Philippe Groby. "Acoustic modeling of micro-lattices obtained by additive manufacturing". In: *Applied Acoustics* 164 (2020), p. 107244. ISSN: 0003-682X. DOI: 10.1016/J.APACOUST.2020.107244.

[67] Elio Di Giulio, Fabio Auriemma, Marialuisa Napolitano, and Raffaele Dragonetti. "Acoustic and thermoacoustic properties of an additive manufactured lattice structure". In: *The Journal of the Acoustical Society of America* 149.6 (2021), pp. 3878–3888. ISSN: 0001-4966. DOI: 10.1121/10.0005085.

[68] Elio Di Giulio, Cong Truc Nguyen, Camille Perrot, and Raffaele Dragonetti. "Wire mesh stack and regenerator model for thermoacoustic devices". In: *Applied Thermal Engineering* 221 (2023), p. 119816. ISSN: 1359-4311. DOI: 10.1016/J.APPLTHERMALENG.2022.119816.

[69] M. E. Hayden and G. W. Swift. "Thermoacoustic relaxation in a pin-array stack". In: *The Journal of the Acoustical Society of America* 102.5 (1998), p. 2714. ISSN: 0001-4966. DOI: 10.1121/1.420325.

[70] G. W. Swift and R. M. Kenlian. "Thermoacoustics in pin-array stacks". In: *Journal of the Acoustical Society of America* 94.2 (1993), pp. 941–943. DOI: 10.1121/1.408196.

[71] Fabio Auriemma, Elio Di Giulio, Marialuisa Napolitano, and Raffaele Dragonetti. "Porous Cores in Small Thermoacoustic Devices for Building Applications". In: *Energies 2020, Vol. 13, Page 2941* 13.11 (2020), p. 2941. ISSN: 19961073. DOI: 10.3390/EN13112941.

[72] Konstantin I. Matveev. "Thermoacoustic energy analysis of transverse-pin and tortuous stacks at large acoustic displacements". In: *International Journal of Thermal Sciences* 49.6 (2010), pp. 1019–1025. ISSN: 1290-0729. DOI: 10.1016/J.IJTHERMALSCI.2009.12.007.

[73] Armando Di Meglio, Elio Di Giulio, Raffaele Dragonetti, and Nicola Massarotti. "A novel model for macroscopic simulation of oscillating heat and fluid flow in porous media". In: *International Journal of Thermal Sciences* 181 (2022), p. 107758. ISSN: 1290-0729. DOI: 10.1016/J.IJTHERMALSCI.2022.107758.

[74] Liu Liu, Yingwen Liu, and Fei Duan. "Effect of the characteristic time on the system performance of a three-stage looped traveling-wave thermoacoustic engine". In: *Energy Conversion and Management* 224 (2020), p. 113367. ISSN: 0196-8904. DOI: 10.1016/J.ENCONMAN.2020.113367.

[75] Esmatullah Maiwand Sharify and Shinya Hasegawa. "Traveling-wave thermoacoustic refrigerator driven by a multistage traveling-wave thermoacoustic engine". In: *Applied Thermal Engineering* 113 (2017), pp. 791–795. ISSN: 1359-4311. DOI: 10.1016/J.APPLTHERMALENG.2016.11.021.

[76] G. W. Swift and W. C. Ward. "Simple harmonic analysis of regenerators". In: *Journal of Thermophysics and Heat Transfer* 10.4 (1996), pp. 652–662. ISSN: 15336808. DOI: 10.2514/3.842.

[77] W.M. Kays and A.L. London. *Compact Heat Exchangers*. New York: McGraw-Hill, 1964.

[78] Bill Ward, John Clark, and Gregory. W. Swift. *Design environment for low-amplitude thermoacoustic energy conversion, DELTAEC version 6.2: Users guide*. Los Alamos National Laboratory, 2008.

[79] Kenichiro Tsuda and Yuki Ueda. "Critical temperature of traveling- and standing-wave thermoacoustic engines using a wet regenerator". In: *Applied Energy* 196 (2017), pp. 62–67. ISSN: 0306-2619. DOI: 10.1016/J.APENERGY.2017.04.004.

[80] Hoang Tuan Luu, Camille Perrot, and Raymond Panneton. "Influence of Porosity, Fiber Radius and Fiber Orientation on the Transport and Acoustic Properties of Random Fiber Structures". In: *Acta Acustica united with Acustica* 103.6 (2017), pp. 1050–1063. ISSN: 18619959. DOI: 10.3813/AAA.919134.

[81] Camille Perrot, Guy Bonnet, M T Hoang, F Chevillotte, F.-X Bécot, Laurent Gautron, A Duval, Minh Tan Hoang, Fabien Chevillotte, François-Xavier Bécot, and Arnaud Duval. "Microstructure, transport, and acoustic properties of open-cell foam samples". In: (2011), Paper 2019 –R36 (Physical Acoustics).

[82] Minh Tan Hoang and Camille Perrot. "Solid films and transports in cellular foams". In: *Journal of Applied Physics* 112.5 (2012), p. 054911. ISSN: 0021-8979. DOI: 10.1063/1.4751345.

[83] Van Hai Trinh, Vincent Langlois, Johann Guilleminot, Camille Perrot, Yacine Khidas, and Olivier Pitois. "Tuning membrane content of sound absorbing cellular foams: Fabrication, experimental evidence and multiscale numerical simulations". In: *Materials & Design* 162 (2019), pp. 345–361. ISSN: 0264-1275. DOI: 10.1016/J.MATDES.2018.11.023.

[84] Olivier Doutres, Noureddine Atalla, and Kevin Dong. "A semi-phenomenological model to predict the acoustic behavior of fully and partially reticulated polyurethane foams". In: *Journal of Applied Physics* 113.5 (2013), p. 054901. ISSN: 0021-8979. DOI: 10.1063/1.4789595.

[85] V. Langlois, A. Kaddami, O. Pitois, and C. Perrot. "Acoustics of monodisperse open-cell foam: An experimental and numerical parametric study". In: *The Journal of the Acoustical Society of America* 148.3 (2020), p. 1767. ISSN: 0001-4966. DOI: 10.1121/10.0001995.

[86] Bryan H. Song and J. Stuart Bolton. "A transfer-matrix approach for estimating the characteristic impedance and wave numbers of limp and rigid porous materials". In: *The Journal of the Acoustical Society of America* 107.3 (2000), p. 1131. ISSN: 0001-4966. DOI: 10.1121/1.428404.

[87] Hans Bodén and Mats Åbom. "Influence of errors on the two-microphone method for measuring acoustic properties in ducts". In: *The Journal of the Acoustical Society of America* 79.2 (1998), p. 541. ISSN: 0001-4966. DOI: 10.1121/1.393542.

[88] L. A. Wilen. "Measurements of thermoacoustic functions for single pores". In: *The Journal of the Acoustical Society of America* 103.3 (1998), p. 1406. ISSN: 0001-4966. DOI: 10.1121/1.421299.

[89] L. A. Wilen. "Dynamic measurements of the thermal dissipation function of reticulated vitreous carbon". In: *The Journal of the Acoustical Society of America* 109.1 (2001), p. 179. ISSN: 0001-4966. DOI: 10.1121/1.1333422.

[90] A. Petculescu and L. A. Wilen. "Lumped-element technique for the measurement of complex density". In: *The Journal of the Acoustical Society of America* 110.4 (2001), p. 1950. ISSN: 0001-4966. DOI: 10.1121/1.1401743.

[91] Chen Li and G. P. Peterson. "The effective thermal conductivity of wire screen". In: *International Journal of Heat and Mass Transfer* 49.21-22 (2006), pp. 4095–4105. ISSN: 0017-9310. DOI: 10.1016/J.IJHEATMASSTRANSFER.2006.03.031.

[92] Elio Di Giulio, Armando Di Meglio, Nicola Massarotti, and Raffaele Dragonetti. "Effective Thermal Conductivity Model for Tetragonal Pin Array Stack". In: *Journal of Fluid Flow, Heat and Mass Transfer* (2022). DOI: 10.11159/JFFHMT.2022.005.

[93] E.G. Jr. Alexander. "Structure-property relationships in heat pipe wicking materials". PhD thesis. North Carolina State University, Raleigh (USA), 1972.

[94] V. Langlois, V. H. Trinh, and C. Perrot. "Electrical conductivity and tortuosity of solid foam: Effect of pore connections". In: *Physical Review E* 100.1 (2019), p. 013115. ISSN: 24700053. DOI: 10.1103/PHYSREVE.100.013115/FIGURES/15/MEDIUM.